Detection of Dry Snow using Spaceborne Microwave Radiometer Data

Lina Zschenderlein

Master's Thesis
Espoo, 10.01.2022

Supervisor

Prof. Jaan Praks

Advisors

Dr. Louise Sandberg Sørensen
Dr. Kari Luojus

DTU

Aalto University

FMI

Cold Climate Engineering

Copyright © 2022 Lina Zschenderlein

Author Lina Zschenderlein

Title Detection of Dry Snow using Spaceborne Microwave Radiometer Data

Degree Programme Cold Climate Engineering - Space Track,
Earth Observation Techniques

Supervisor Prof. Jaan Praks

Advisors Dr. Louise Sandberg Sørensen
Dr. Kari Luojus

Date 10.01.2022 **Number of Pages** 56+20 **Language** English

Abstract

Snow monitoring on global scale is an important task considering the essential role of snow cover in the Earth's climate and the scarcity of ground-based snow observations. Snow has distinctive, frequency-dependent characteristics in terms of microwave emission. This enables the use of brightness temperatures, as measured by spaceborne passive microwave sensors, not only for the estimation of snow cover extent (SCE) through (dry) snow detection, but also for the retrieval of snow depth and snow water equivalent (SWE). Approaches for SWE retrieval, such as the methodology of the GlobSnow v3.0 SWE product, frequently implement dry snow detection as one of the main processing steps. Reliable dry snow detection is thus crucial, however, common algorithms are known to generally underestimate the presence of snow due to their sensitivity to vegetation and liquid water content of the snowpack, amongst other. Although several suggestions for improvement have been proposed, an extensive, long-term comparison has not been conducted. This thesis hence investigates six current dry snow detection algorithms and their intraseasonal performance in order to identify the most appropriate one for implementation in the GlobSnow SWE product. The aim is to improve the product which is primarily affected by underestimation during the snow accumulation period from September to February. The investigated algorithms are based on the brightness temperature difference involving primarily, but not exclusively, the 18/19-GHz and 37-GHz channels which are available for the SMMR, SSM/I and SSMIS instruments covering more than 40 years of observations. In addition to conventional daily snow masks, cumulative snow masks are investigated as a means to counteract underestimation. The assessment focuses on seasonal snow above 40° North, and is conducted for the snow seasons from 1979/1980 to 2017/2018 with reference to exhaustive, in situ snow depth data from multiple sources. In addition, spatially-complete SCE maps by the Interactive Multisensor Snow and Ice Mapping System serve as reference from 2007/2008 to 2016/2017, in order to evaluate the detected snow cover extent as a whole. The results emphasise the potential of cumulative masks to counteract underestimation and increase detection accuracy, and highlight the benefit of discriminating between different scattering sources, that could otherwise be mistaken for snow. Two methods are found to be overall best-performing: the empirically-derived algorithm of the EUMETSAT H SAF H11 product (applicable to SMMR, SSM/I and SSMIS), and the decision tree published by Grody and Basist in 1996 (applicable to SSM/I and SSMIS). Promising accuracies with respect to in situ data are achieved using cumulative masks, reaching approximately 0.83 and 0.80 for the approaches of Grody and Basist and of the H SAF product, respectively. Implementing the H SAF algorithm into the GlobSnow SWE product is expected to lead to immediate improvements of the latter and is thus planned, though falls outside the scope of this thesis. Further investigation is required to adapt the approach of Grody and Basist to the whole long-term passive microwave data record including SMMR data.

Keywords Dry Snow Detection, Passive Microwave Remote Sensing, Northern Hemisphere, Snow Cover Extent, GlobSnow SWE, SMMR, SSM/I, SSMIS

Contents

List of Figures

List of Tables

List of Algorithms

Nomenclature

Abbreviations

AFWA	Air Force Weather Agency
AMSR-E	Advanced Microwave Scanning Radiometer - Earth Observing System
AMSR2	Advanced Microwave Scanning Radiometer 2
ANSA	AFWA/NASA Snow Algorithm
ASCII	American Standard Code for Information Interchange
AVHRR	Advanced Very-High-Resolution Radiometer
CCI	ESA Climate Change Initiative
DMSP	Defense Meteorological Satellite Program
DTU	Technical University of Denmark
DW	Downward radiation
EASE-Grid	Equal-Area Scalable Earth-Grid
ECMWF	European Centre for Medium-Range Weather Forecasts
ECV	Essential Climate Variable
ESA	European Space Agency
EUMETSAT	European Organisation for the Exploitation of Meteorological Satellites
FMI	Finnish Meteorological Institute
FN	False negative
FOV	Field of view
FP	False positive
GCOM-W	JAXA Global Change Observation Mission – Water
GCOS	Global Climate Observing System
GHCN	Global Historical Climatology Network
GSFC	NASA Goddard Space Flight Center
H SAF	EUMETSAT Satellite Application Facility on Support to Operational Hydrology and Water Management
HUT	Helsinki University of Technology
IMS	Interactive Multisensor Snow and Ice Mapping System
JASMES	JAXA Satellite Monitoring for Environmental Studies
JAXA	Japan Aerospace Exploration Agency

MAE	Mean absolute error
MODIS	Moderate Resolution Imaging Spectroradiometer
NaN	Not a Number
NASA	National Aeronautics and Space Administration
NOAA	National Oceanic and Atmospheric Administration
NSIDC	National Snow and Ice Data Center
PM	Passive microwave
RIHMI-WDC	All-Russia Research Institute of Hydrometeorological Information - World Data Center
RMSE	Root-mean-square error
SCAT	Scattering signature relationships
SCE	Snow cover extent
SD	Snow depth
SE	Surface emission
SMMR	Scanning Multichannel Microwave Radiometer
SS	Surface-scattered part of downward radiation
SSM/I	Special Sensor Microwave Imager
SSMIS	Special Sensor Microwave Imager Sounder
SWE	Snow water equivalent
TN	True negative
TP	True positive
UP	Upward radiation
USNIC	United States National Ice Center
WMO	World Meteorological Organisation

Greek

ϵ	Emissivity
ε	Permittivity
ε_0	Permittivity of free space
ε_r	Relative permittivity
ε_r'	Dielectric constant (real part of complex relative permittivity)
ε_r''	Dielectric loss factor (imaginary part of complex relative permittivity)
κ_e	Extinction coefficient
λ	Wavelength

Ω	Solid angle
Ω_p	Pattern solid angle
Ω_s	Source solid angle
ϕ	Angle of directionality
τ	Optical depth
θ	Angle of directionality
Υ_a	Atmospheric transmissivity

Latin

A_r	Receiving effective aperture
B	Bandwidth
b	Wien's displacement constant
c	Speed of light in vacuum
D	Antenna width (or diameter)
d_0	Effective snow grain size
e	Euler's number
F	Antenna pattern
f	Frequency
H	Horizontal polarisation
h	Planck's constant
I	Brightness intensity
i	Imaginary unit
I_λ	Spectral brightness intensity (wavelength-dependent)
I_bb	Brightness intensity of a blackbody
I_f	Spectral brightness intensity (frequency-dependent)
J	Source function
j	Sample
k	Boltzmann's constant
n	Maximum number of samples or predictions
P	Power
p	Forest cover fraction
R	Thickness
R_c	Regression coefficient
$\mathbf{R}$	Location of observation of electromagnetic radiation

$\widehat{\mathbf{R}}$	Direction of the propagation of electromagnetic radiation
T	(Kinetic) Temperature
T'_A	Lossless antenna temperature
T_A	Antenna temperature
T_B	Brightness temperature
T_{DN}	Brightness temperature component of downward radiation
T_{SE}	Brightness temperature component of surface emission
T_{SS}	Brightness temperature component of the surface-scattered part of downward radiation
T_{UP}	Brightness temperature component of upward radiation
V	Vertical polarisation
x	Satellite flight path
y	Reference value
$\hat{y}$	Predicted value

1 Introduction

The cryosphere—derived from the Greek 'krios' for cold, icy and 'sphaira' for ball, globe—describes the part of the Earth where water is in its solid state [1], [2]. This includes snow cover, permafrost, sea ice, freshwater ice like frozen lakes and rivers, and large terrestrial ice masses such as ice sheets and glaciers, and related phenomena including ice shelves and icebergs [1]. The cryosphere covers different parts of the globe, as shown in Fig. 1.1, and is both a seasonal or permanent phenomenon that is mostly present at high latitudes centered around the poles due to generally lower temperatures [1]. It has a central role in the global climate with close links to the atmosphere and hydrosphere, affecting surface energy fluxes and freshwater storage, amongst others [2]. In the context of climate change, models predict the largest changes to occur in the polar regions: the so-called polar amplification [1]. Monitoring of the cryosphere and its elements is important, though the hostile environment and geographical remoteness of most of the cryosphere impede ground-based observations. Remote sensing methods and particularly the use of satellite data are therefore favourable [1].

Snow cover, the second-largest component of the cryosphere, is a crucial factor in the Earth's energy balance owing to its high albedo [2], i.e. its ability to reflect a large fraction of the incoming solar radiation. Even though the largest variations in surface albedo are due to seasonal changes in snow cover, seasonal snow predominantly occurs in the Northern Hemisphere only [1], as shown in Fig. 1.1. The maximum extent covers about 50% of the hemispheric land area [3], making meltwater from seasonal snow essential for freshwater resources, soil moisture and groundwater [1], [4]. Hence, it is important to estimate both the snow cover extent (SCE) and the snow mass, measured by means of snow water equivalent (SWE), on global scale.

Snow is defined as an Essential Climate Variable (ECV) by the Global Climate Observing System (GCOS), with the main snow parameters being SCE, SWE and snow depth (SD) [5]. The Climate Change Initiative (CCI) programme of the European Space Agency (ESA) encompasses 26 ECV projects, including the ESA CCI Snow project whose objective is to generate consistent long-time series of daily global snow products from archived and current Earth observation data [6]. This includes SCE maps from optical satellite data and SWE products from passive microwave (PM) satellite data, addressing the snow parameters SCE and SWE, and indirectly SD which can be derived from SWE for known or estimated snow density [6]. Within ESA CCI Snow, the retrieval of SWE from PM data is investigated by the Finnish Meteorological Institute (FMI), and this activity succeeds the ESA GlobSnow project. Recently, the GlobSnow v3.0 Northern Hemisphere SWE dataset [7] has been used to assess the annual hemispheric maximum snow mass for 1980–2018 [4]. The quantification of snow mass is achieved on hemispheric, continental and regional scale, and the trend analysis provides critical information for the evaluation of impacts and feedbacks due to snow mass changes and trends [4].

In contrast to visible and infrared bands, the microwave energy that is emitted from a snowpack originates not only from its surface, but also from deeper snow layers and from the ground beneath [8]. The emission in the microwave region is thus sensitive to a variety of snow properties, namely SD, SWE, temperature, and state (wet or dry), and additionally to the soil conditions below the snow [8], [9]. Microwave emission characteristics are estimated by means of brightness temperatures observed by PM sensors or radiometers [10], and spaceborne PM data is therefore commonly used for snow monitoring on

global scale. Due to significant differences in emission between wet and dry snow [1], [9], [11], the use of PM methods generally applies to dry snow with liquid water content equal to zero [12]. Because dry snow itself presents distinctive, frequency-dependent features in the microwave part of its electromagnetic spectrum, PM methods generally implement multifrequency data for SWE retrieval or snow detection in first instance [1], [12]. Algorithms for dry snow detection are mainly based on the brightness temperature difference between two channels, one of lower frequency that is less affected by snow cover, and one of higher frequency whose measured brightness temperature is noticeably affected by snow cover in form of attenuation [13]–[15].

Figure 1.1. Overview of the cryospheric components [16]. Snow cover extent for the Northern Hemisphere is represented by the 1966–2005 February average, for the Southern Hemisphere by the 1987–2003 August average.

Albeit dry snow detection is a typical preprocessing step for global SWE retrieval methods in order to minimise uncertainties in the latter [12], we lack an extensive, long-term comparison of PM dry snow detection approaches and their intraseasonal performance. This also affects the GlobSnow product, which implements PM dry snow detection prior to the actual SWE retrieval [7]. Products such as GlobSnow use primarily spaceborne radiometer data, because it allows for the discrimination between dry and wet snow on hemispheric scale. The presence of liquid water within the snowpack adds additional ambiguity to SWE retrievals [12]. Moreover, auxiliary data sources are kept to a minimum with the purpose to limit error propagation [12], and under the consideration that global ground-truth measurements are very sparse for SD and SWE, or not even available for snow wetness. The integration of PM dry snow detection is thus crucial as is the knowledge on the spatial and temporal behaviour of different approaches, which generally tend to underestimate snow cover [1].

The aim of this thesis is to investigate and evaluate the performance of existing algorithms for the global detection of dry snow by means of satellite-based radiometer data. The com-

parison of PM dry snow detection algorithms is carried out with the ultimate objective to select the most suitable one for implementation in the follow-up datasets of the GlobSnow v3.0 and ESA CCI Snow v2.0 products. By improving dry snow detection, it is expected to further enhance the SWE retrieval itself, though the actual implementation and testing with GlobSnow is outside the scope of this project. In accordance with the long-time series approach of CCI Snow [6], GlobSnow uses data from the Scanning Multichannel Microwave Radiometer (SMMR), Special Sensor Microwave Imager (SSM/I) and the Special Sensor Microwave Imager/Sounder (SSMIS) spanning the years from 1979 onwards [7]. In this context, the identification, selection and implementation of relevant algorithms is restricted by the available channels of those radiometers, with an emphasis on brightness temperature differences between 18/19 GHz (K-band) and 37 GHz (Ka-band) since those are most frequently used in literature, see e.g. [13]–[15], and are available for the whole time series. Algorithms that are applicable only to SSM/I and SSMIS data may be considered given the relatively long time span (1987 onwards), whereby algorithms that are applicable to all radiometers are preferred. It is known that the GlobSnow SWE product presents higher relative errors in the beginning of the snow season between October and December in comparison to mid-winter from January to March [7]. The comparison of PM dry snow detection approaches is thus tailored around the months of snow accumulation, i.e. the months with an increase in snow cover extent, covering the very beginning of the snow season in September up to its approximate peak in snow cover extent in February. Furthermore, the ability of cumulative snow masks to tackle underestimation in SCE is investigated besides common daily snow masks derived from daily brightness temperature data. Those cumulative snow masks follow the example of [7] and, as the name suggest, consider snow to be cumulative and retain detected snow pixels for the whole season. Considering the focus on terrestrial seasonal snow cover in the Northern Hemisphere, brightness temperature data above 40° North are applied, similar to [4]. The performance of the algorithms is evaluated for 40 years, from 1979 to 2018, against extensive synoptic SD measurements from weather stations across the whole Northern Hemisphere. In addition to the pointwise in situ observations, SCE maps of the Interactive Multisensor Snow and Ice Mapping System [17] are used as spatially complete reference, which is a blended product derived from multiple data sources including but not limited to ground measurements, PM data and optical imagery.

This document gives some background on microwave remote sensing, and in particular on passive microwave remote sensing, also called microwave radiometry. An overview of the characteristics of snow is given, and the physical properties of snow are subsequently put into context with passive microwave remote sensing. Common dry snow detection algorithms using radiometer data are then outlined, followed by an extract of global snow products using also other types of spaceborne data. The next chapters list the datasets used in this thesis and explain their implementation, including the computation of snow masks, together with the evaluation of the applied dry snow detection algorithms. The actual analysis of dry snow detection approaches follows, where the different approaches are compared to each other, and the findings are presented and discussed. The last chapter gives a closing summary of the work.

2 Remote Sensing of Snow

Snow is considered an Essential Climate Variable by the GCOS of the World Meteorological Organisation (WMO), indicating that snow plays a critical role in the characterization of the Earth's climate [5]. The limited spatial density of in situ snow measurements on global scale highlights the importance of spaceborne remote sensing for snow monitoring. Important monitored snow attributes are snow cover extent, snow depth and snow water equivalent.

This chapter introduces microwave remote sensing as a whole in Section 2.1 and discusses then passive remote sensing in the microwave region in more detail in Section 2.1.1. The underlying concepts of thermal emission and radiative transfer are presented briefly in Sections 2.1.2 and 2.1.3, following primarily [10]. Section 2.2 then outlines the properties of snow, also in context of the Northern Hemisphere as region of interest in Section 2.2.1. Section 2.2.2 links the physical properties of snow with the theory in Sections 2.1.2 and 2.1.3, and Section 2.3 shows how snow properties can be derived from radiometry [1], [10].

2.1 Microwave Remote Sensing

Remote sensing in general describes the process of collecting information about an object or a material without physical contact, and refers in more specific terms to airborne or spaceborne observations using electromagnetic radiation. Terrestrial remote sensing most often makes use of the 'windows' with (nearly) no atmospheric attenuation in the visible and microwave regions of the electromagnetic spectrum [11]. The visible region includes wavelengths between about 0.4 to 0.7 µm [10], whereas the microwave region covers wavelengths between roughly 1 mm to 1 m which is equivalent to frequencies between 300 and 0.3 GHz. Those useful wavelength/frequency regions as well as the influence of different atmospheric components and precipitation on attenuation are shown in Fig. 2.1.

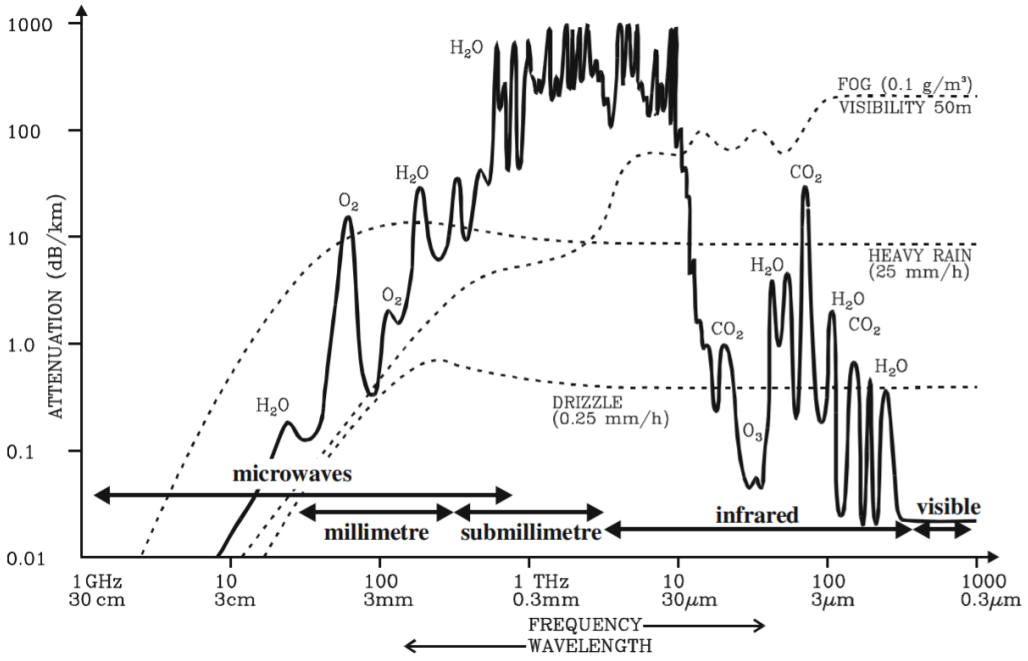

Figure 2.1. Attenuation of a clear atmosphere [11]. The dashed curves show additional attenuation from fog, heavy rain and drizzle.

There are two types of instruments used for microwave remote sensing, referred to as active and passive systems. As the name suggests, active ones such as radar systems actively emit electromagnetic radiation [10]. The transmitted radiation pulses are reflected upon illuminating a ground area, and the scattered signal is then received and measured by the sensor. Passive ones on the other hand simply measure radiation incident on the sensor. This includes the energy radiated and reflected by the Earth's surface and atmosphere, i.e. direct thermal emission as well as reflected thermal emissions from other objects like the sun. The concept of passive microwave remote sensing or radiometry is described in more detail in the following.

2.1.1 Microwave Radiometry

The concept of radiometry describes the measurement of incoherent radiant electromagnetic energy [10]. In the case of PM imaging, the measured radiation typically has wavelengths of 3 mm up to 6 cm with equivalent frequencies between 5 and 100 GHz [1]. Radiation in this region is transmitted through the atmosphere and most clouds [1], [2]. Snow mapping is thus possible in all weather conditions and without solar illumination which allows for a high temporal resolution including during polar nights, a clear benefit in comparison to optical imagery. Another advantage over optical methods is the ability to not only identify the presence of snow cover but to also estimate SD and SWE on global scale thanks to characteristic properties of snow regarding microwave emission [2], as described in Sections 2.2 and 2.3.

Due to comparatively long wavelengths, photons are much less energetic in the microwave region when compared to visible light. Electro-optical systems as used for the visible range are not applicable as such for PM remote sensing [1]. PM sensors or so-called radiometers follow a different detection technique, where the radiation is collected by an antenna. The antenna converts the received power into a fluctuating voltage difference which is then amplified and detected [1]. The size of the antenna directly influences the spatial resolution since the beamwidth is approximately λ/D, for wavelength λ and antenna width (often diameter) D [1]. Beamwidth, usually defined as half-power (3-dB) beamwidth, describes the angular width of the main beam where the normalized radiation intensity is half of its maximum value [10]. The spatial resolution is generally expressed in terms of the (instantaneous) field of view (FOV) which is the area on ground that is observed by the antenna. The effective FOV, on the other hand, takes the relative motion into account and is hence slightly larger.

The long wavelengths together with practical limits of antenna sizes result in relatively coarse spatial resolutions of typically several tens of kilometres. Large antennas also restrict the feasibility of constructing antenna arrays. In order to still ensure sufficient spatial coverage, beam scanning methods can be applied. A common form of mechanical scanning is the conical scan, as illustrated in Fig. 2.2. Here, the antenna beam i.e. direction of maximum sensitivity is rotated in a wide cone around nadir, typically with an incidence angle of around 50° measured between the vertical and the antenna beam [10]. This causes a circular arc footprint pattern in front of the satellite, centered around nadir and along the satellite flight path (noted by x in Fig. 2.2). Due to mechanical constraints, amongst other, the swath width of conical-scanning systems is limited to approximately 1 700 km [10], though still allows for large spatial coverage [2], [3].

The sensitivity of a radiometer, or radiometric resolution, depends on factors such as the physical temperature of the instrument, integration time and bandwidth, amongst other. It is defined by the smallest detectable change in brightness temperature, with typical values between a few tenths to one Kelvin [1]. Radiometers thus measure the

electromagnetic energy in the microwave region, as a whole or along a single polarisation direction, by means of brightness temperature. The radiometers of interest in this project are SMMR, SSM/I and SSMIS.

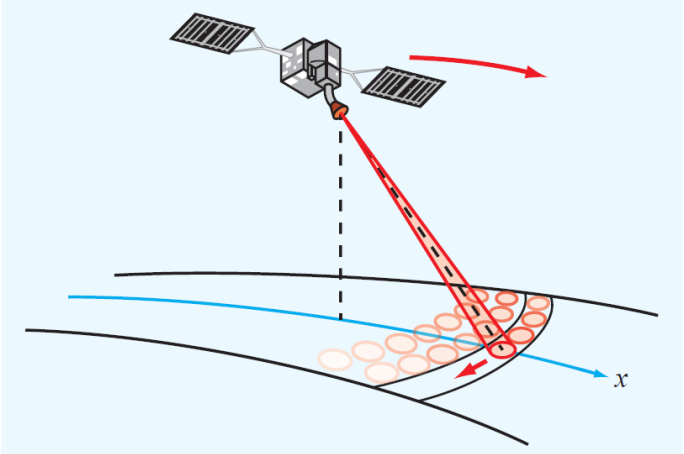

Figure 2.2. Radiometric imaging by conical scanning [10]. Dashed black lines mark the vertical (azimuth) and the beam direction; Red arrows indicate the rotation (conical scan) of the antenna beam and the flight direction of the satellite, along the flight path x.

2.1.2 Characterisation of Thermal Emission

A blackbody is an idealised material that absorbs all incident radiation without reflecting any and is thus a perfect absorber. Due to thermodynamic equilibrium, where the amount of absorbed energy equals the amount of emitted energy, a blackbody is also a perfect emitter. The radiation of a blackbody with spectral radiance or spectral brightness (intensity) I_f[1] is given by Planck's radiation law as

$$I_f = \frac{2hf^3}{c^2}\left(\frac{1}{e^{hf/kT}-1}\right) \tag{2.1}$$

for frequency f and the blackbody's kinetic temperature T, and with Planck's constant h, Boltzmann's constant k and light speed c in vacuum [10]. I_f as a function of frequency describes the amplitude of the emitted radiation over the entire spectrum of a blackbody of given T. An example for $T = 300\,\mathrm{K}$ is shown in Fig. 2.3, with a peak in radiation for $f_{\max}$. The corresponding dominant wavelength is found using Wien's displacement law $\lambda_{\max} = b/T$, with b as Wien's displacement constant. The total brightness intensity I results from the integration of I_f over the entire spectrum, since $dI = I_f\, df$. Increasing the temperature leads to an overall raise of the curve and thus of I, together with an increase in $f_{\max}$.

For lower frequencies with $hf/kT \ll 1$, a linear approximation of (2.1) can be used, namely Rayleigh-Jeans law [10]

$$I_f \approx \frac{2kTf^2}{c^2}. \tag{2.2}$$

This expression also applies to the microwave region with frequencies in the range of 10^9 Hz (GHz), where its deviation from Planck's law is less than 1% [10]. The fit between Planck's law and Rayleigh-Jeans law is visualised in Fig. 2.3.

[1] Frequency- or wavelength-dependent formulations with subscripts f and λ, respectively, can of course be transformed to one or the other. Though $f = c/\lambda$ cannot simply be used for conversion since $I_f \neq I_\lambda$, and instead $I_f\, df = I_\lambda\, d\lambda$ applies with $df/d\lambda = -c/\lambda^2$.

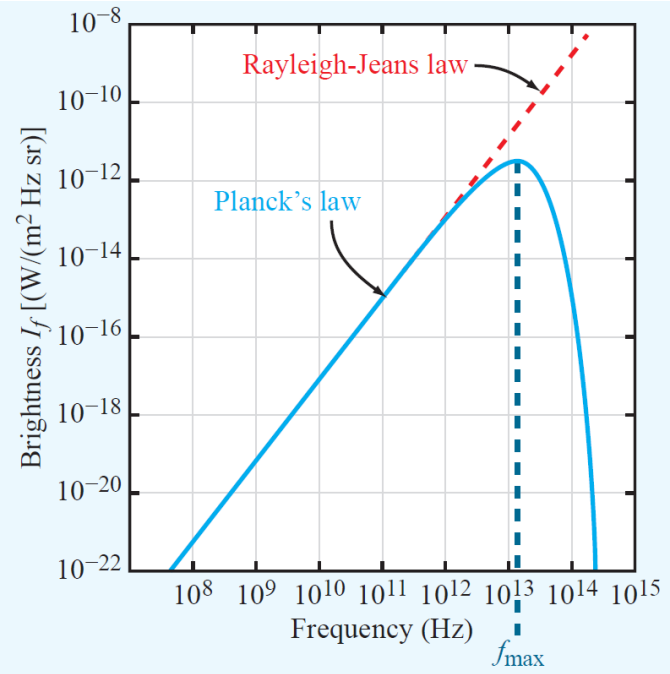

Figure 2.3. Comparison of Planck's law with the Rayleigh-Jeans law [10]. The radiation spectrum (blue) with peak for frequency f_{max} and its low-frequency approximation (red) are given for 300 K.

To summarise, I_f is the power which is emitted over a bandwidth of 1 Hz and through a solid angle of 1 sr by a blackbody with a surface area of 1 m^2. The total received power P by an antenna is hence

$$P = A_r \Omega_s \int_{f_1}^{f_2} I_f \, df \tag{2.3}$$

with receiving effective aperture A_r, source solid angle Ω_s and bandwidth $B = (f_2 - f_1)$. When accounting for the directionality of the antenna with radiation pattern $F(\theta, \phi)$ over the full solid angle $\Omega = 4\pi$, (2.3) becomes

$$P = A_r \int_{f_1}^{f_2} \iint_{4\pi} I_f \, F(\theta, \phi) \, d\Omega \, df. \tag{2.4}$$

An antenna pattern is illustrated in grey in Fig. 2.4, with a mainlobe, sidelobes and backlobes. Typically, (polarised) antennas measure a single polarisation, horizontal H or vertical V, and a factor of $1/2$ has to be introduced to (2.4). Together with (2.2) and the pattern solid angle $\Omega_p = \iint_{4\pi} F(\theta, \phi) \, d\Omega = \lambda^2 / A_r$, (2.3) simplifies to

$$P = kTB, \tag{2.5}$$

given a narrow bandwidth over which I_f remains approximately constant. In microwave remote sensing, this direct linear relationship (2.3) between 'power' and 'temperature' results in the interchangeable use of those two terms [10].

In reality, materials are neither perfect absorbers nor emitters, but rather reflect and absorb/emit fractions of the incoming radiation depending on their physical temperature and dielectric properties. Since the concept of a blackbody is an idealisation, it is used as reference to express the emittance of any other materials, so-called grey bodies, by

means of brightness temperature. Brightness temperature is defined as the blackbody equivalent radiometric temperature [10], in other words, the brightness temperature of a material equals the temperature of a blackbody that would radiate the same thermal energy. The ratio of the (non-uniform) brightness intensity $I(\theta, \phi)$ of a grey body to the (uniform) brightness intensity I_{bb} of a blackbody, or equivalently the ratio of the grey body's brightness temperature $T_B(\theta, \phi)$ and the blackbody's physical temperature T, is defined as the emissivity ϵ:

$$\epsilon(\theta, \phi) = \frac{I(\theta, \phi)}{I_{\mathrm{bb}}} = \frac{T_B(\theta, \phi)}{T}. \tag{2.6}$$

Depending on its viewing direction, the antenna observes a brightness temperature distribution $T_B(\theta, \phi)$ as illustrated in Fig. 2.4. Different components of the radiation within the mainlobe observation area are surface emission (SE), upward radiation (UP) emitted by the atmosphere, and the surface-scattered (SS) part of downward radiation (DN) emitted by the atmosphere. The observed brightness temperature T_B is formed of the corresponding brightness temperatures T_{SE}, T_{UP}, T_{SS} and T_{DN}, respectively. Taking into account the atmospheric transmissivity Υ_{a}, this results in:

$$T_B = T_{\mathrm{UP}} + \Upsilon_{\mathrm{a}} \left(T_{\mathrm{SE}} + T_{\mathrm{SS}} \right). \tag{2.7}$$

As mentioned earlier regarding (2.5), the power incident on the antenna is interchangeable with temperature and hence with brightness temperature T_B for grey bodies. For a lossless antenna, the antenna temperature T'_A would thus equal T_B. However, losses and other contributions to T'_A have to be considered with respect to the actual antenna temperature T_A. In addition to the mainlobe, contributions from the side and backlobes have to be considered as well as cosmic background radiation. The latter is corrected for by pointing the radiometer towards space. Note that in case of cold space correction in the microwave region, the Rayleigh-Jeans law actually does not apply for cold space with a temperature of only about 2.7 K [10].

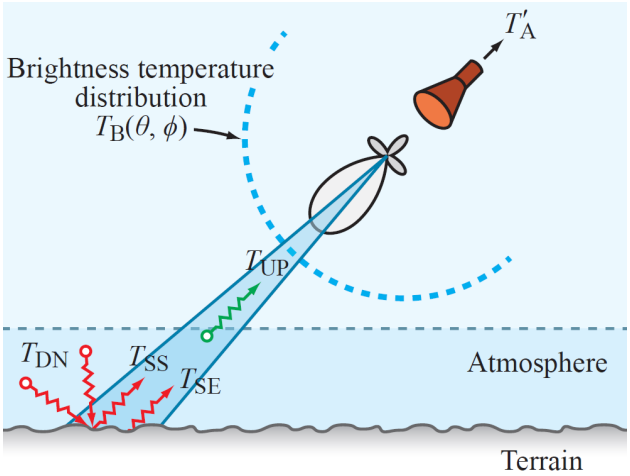

Figure 2.4. Surface and atmospheric emission, adapted from [10]. Subscripts label the contributions to the observed brightness temperature distribution $T_B(\theta, \phi)$: surface emission (SE), upward radiation (UP) emitted by the atmosphere, and the surface-scattered (SS) part of downward radiation (DN) emitted by the atmosphere.

2.1.3 Radiative Transfer

The propagation of electromagnetic radiation through a medium is affected by different processes, namely absorption, emission, and scattering. The resulting intensity of the radiation is described mathematically by the radiative transfer equation [11], which is given in a simple form as

$$\frac{dI}{d\tau} + I = J, \tag{2.8}$$

with intensity I and source function J accounting for thermal emission and scattering [10]. Both are defined at location $\mathbf{R}$ and for propagation in direction $\widehat{\mathbf{R}}$. Along $\widehat{\mathbf{R}}$, $d\tau$ is an increment of optical depth, or rather electromagnetic depth since not only optical wavelengths are addressed. For thickness dR of the medium, $d\tau = \kappa_\mathrm{e}\, dR$ which describes the observed absorption of dR by means of the extinction coefficient κ_e, or also called power attenuation coefficient. The extincted energy is due to either absorption by the material itself, or scattering by particles contained in the material, or due to both. Equation (2.8) can also be expressed in terms of T_B, and is usually solved numerically [2], [10]. The simplest model of radiative transfer considers a local thermodynamic equilibrium, a homogeneous medium and no scattering effects.

The energy loss caused by scattering refers to changes in direction of the energy incident on $\mathbf{R}$—in Fig. 2.5 equivalent to the position of the radiometer. For an inhomogeneous medium, scattering occurs because the dielectric properties of the particles are considerably different to the ones of air as background medium [18]. This causes the energy to get refracted away from the original direction $\widehat{\mathbf{R}}$, as illustrated in Fig. 2.5 for the emission of ground underneath a snow layer. The dielectric properties of snow and their meaning for the emission of snow are explained in more detain in Section 2.2.2, including permittivity ε and relative permittivity ε_r.

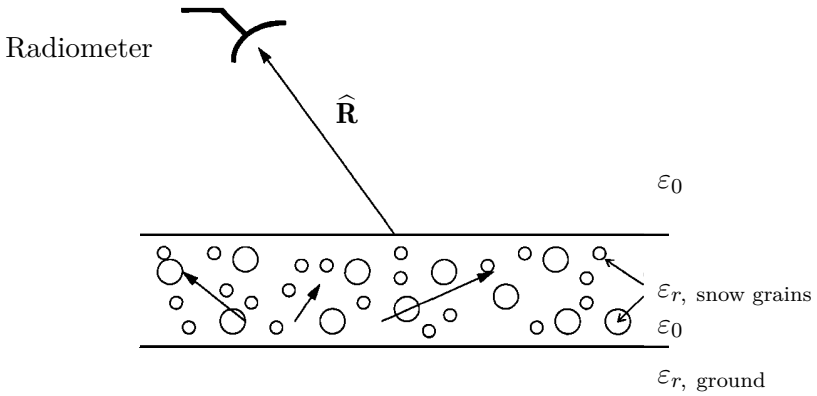

Figure 2.5. Geometrical configuration for thermal emission from ground underneath snow, adapted from [19]. Different media properties influence the thermal emission in direction $\widehat{\mathbf{R}}$ that is measured by the radiometer. This includes the permittivity of free space ε_0, for air as such and within the snow (a layer of particles enclosed in air), and the relative permittivity ε_r of ground and of snow grains, amongst other.

In conventional radiative transfer theory, particles are assumed to scatter independently from each other [18]. However, this assumption is not valid for snow because of the densely packed ice crystals which makes snow a so-called dense medium [2], [18]. The term 'dense' generally refers to a high refraction index; A material is considered more dense than an-

other if it has a larger refraction index [10]. In order to understand the interaction between snow grains and electromagnetic waves in the microwave region, the correlated scattering or volume scattering in dense media has to be understood [19]. Dense medium radiative transfer theory accounts for this correlation in scattering and for the deficiencies of conventional theory in this regard [18]. Variations of this model like [19] account for multiple volumetric scattering, i.e. volume scattering for multiple particles of different sizes. It considers a two-layer medium, such as snow on top of ground and as shown in Fig. 2.5, where the boundary conditions are set by the Fresnel equations to account for the transmission and reflection of electromagnetic waves at dielectric boundaries. Dense medium radiative transfer is commonly used in the context of (passive) microwave remote sensing, e.g. to model brightness temperatures [18]–[20]. A further example besides dense medium radiative transfer models is the Helsinki University of Technology (HUT) snow microwave emission model [21], a semi-emipirical model based on radiative transfer. SWE retrieval through the inversion of such models is an alternative to PM-based SWE retrieval [2].

2.2 Characteristics of Snow

Snow is a mixture of ice crystals, liquid water and air, with densities ranging between 0.2 and 0.6 $\mathrm{Mg\,m^{-3}}$ [1]. Over time, the density of a snow pack increases due to compaction by wind and gravity, and due to thermal metamorphism [1]. Its internal structure is characterised primarily through the grain or crystal size, commonly defined as the crystal radius with values typically between 0.1 and 3.0 mm, and by the form and orientation of the crystals [1]. A further property is snow wetness i.e. liquid water content. For temperatures below the freezing point, a snow pack is unlikely to contain any liquid water and is thus referred to as 'dry snow'. Though for temperatures at or above the freezing point, a considerable amount of liquid water might be present within the snow, which is then 'wet snow'. The total amount of water that is hold by a unit area of the snow pack is the so-called snow water equivalent. It is defined as the depth of liquid water that would result if the snowpack was melted instantaneously.

2.2.1 Seasonal Snow in the Northern Hemisphere

Commonly, it is distinguished between temporary, seasonal and permanent snow cover [1]. Temporary and seasonal snow cover last on the scale of days and months, respectively, and typically melt during summer. Permanent snow cover on the other hand is preserved over several years and mainly occurs in Antarctica and Greenland, resulting in snow accumulation over the ice sheets. In the Southern Hemisphere, permanent snow cover hence predominates whereas in the Northern Hemisphere, temporary and seasonal snow are primarily observed. This project investigates terrestrial seasonal snow cover and therefore the Northern Hemisphere, disregarding accumulation over Greenland. Average seasonal changes in snow cover extent for this area of interest are given in Fig. 2.6. The spatial extent presents a minimum of about 4 million square kilometers in August, and reaches a maximum of around 46 million square kilometers approximately in January [1].

The maximum snow cover extent equals approximately $40 - 50\%$ of the land area which makes snow cover the dominant land-cover type during snow season [1], [3]. Seasonal snow cover plays a significant role in the global climate as it causes the largest annual and interannual variations in land surface albedo [22]. Albedo is a measure of how much incident solar radiation is reflected or scattered upwards by a surface, generally given for shortwave radiation between 0.3 and 3.0 µm, and is a critical parameter to specify the surface energy balance [23]. The high albedo of snow is a key regulator of the absorption of solar energy for snow-covered areas [2], though earlier melting and less area coverage have been observed due to climate change which in turn decreases the albedo

and further accelerates melting and decreases snow cover extent [3], [23]. This effect is the so-called snow-albedo feedback [23]. Aside from its climatological impact, snow is a main contributor to hydrology and influences local groundwater recharge, (snowmelt) river run-off, flooding or energy supply through hydropower, amongst other [1], [3]. Both the variability and extent of seasonal snow cover are hence important factors in climate and hydrologic systems, highlighting the importance of spatial and temporal mapping of snow-cover conditions—on global as well as on regional scale.

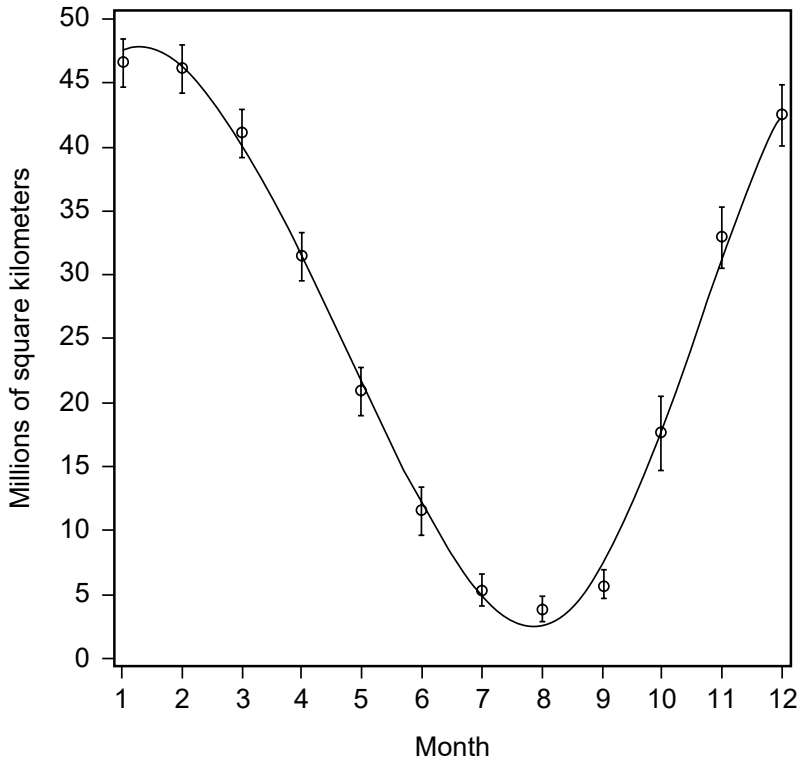

Figure 2.6. Average snow cover in the Northern Hemisphere excluding Greenland during 1972–1991 [1]. Circles show mean values with error bars of ±1 standard deviation in interannual variation. The curve is the best-fitting harmonic with terms at one and two cycles per year.

The latitudinal occurrence of seasonal snow varies throughout the Northern Hemisphere. In North America, seasonal snow occurs for latitudes generally north of 40°, whereas in Western Europe, it is north of 60° and in mountainous areas. In Eastern Europe, seasonal snow is found northward from about 50° and extends in Asia as far south as 30° latitude [1]. The latitudinal range may differ for temporary snow cover. Since the vast majority of seasonal snow in the Northern Hemisphere is found north of 40° North, this is set as study area following the example of Pulliainen et al. [4] whereby the authors exclude alpine areas with high topographic variability within the satellite data footprint. The average snow distribution for this area without mountainous regions is shown in Fig. 2.7. The amount of snow mass generally increases for regions further north, with the largest average SWE ocurring in Siberia, the north of Scandinavia and around the Canadian province Quebec. Figure 2.7 considers essentially the time period of interest of this thesis: the winters from 1979/1980 until 2017/2018.

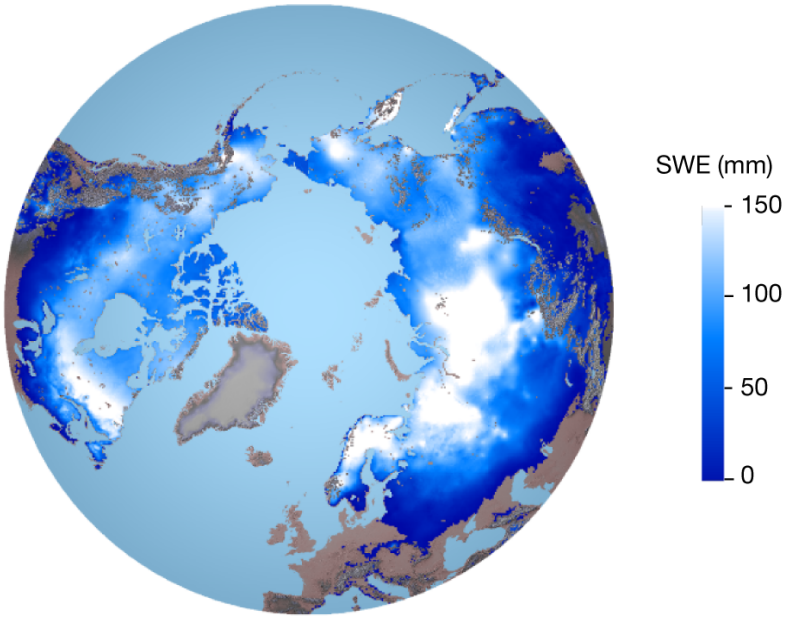

Figure 2.7. Average snow distribution in the Northern Hemisphere during 1980–2018 [4]. The snow distribution is given in terms of SWE for non-alpine regions above 40° North.

2.2.2 Dielectric Properties

The electromagnetic properties of a material or object define its effects on electromagnetic radiation. For microwave remote sensing, the most important characteristic is the complex electric permittivity ε, which is expressed by means of the permittivity of free space ε_0 and the dimensionless, material-specific relative permittivity ε_r as $\varepsilon = \varepsilon_r \varepsilon_0$. Since ε_r is also complex, it can be denoted as:

$$\varepsilon_r = \varepsilon_r' - i\varepsilon_r''. \tag{2.9}$$

Its real part ε_r', also called dielectric constant, represents the energy scattered and reflected by the material, whereas its imaginary part, the dielectric loss factor, describes the energy losses due to absorption [10], [11]. Both are dependent on the frequency and on the temperature of the material.

Most encountered solid materials in remote sensing are non-conducting, so-called dielectrics [11]—for perfect dielectrics with zero conductivity the imaginary part of (2.9) equals zero. Since ε_r'' of the observed dielectric materials is most often insignificantly small, the dielectric constant becomes the dominant property. The majority of the Earth's dry land-based materials, such as soil, vegetation, ice and snow, have a comparatively low ε_r' between about 1 and 8 [24], making them to some degree transparent to microwaves [11]. The dielectric constant of dry snow depends directly on the dielectric constant of air, of ice, and on the ratio of snow to ice density, whilst being essentially independent of frequency and temperature in the microwave region [10]. For a typical density of $0.3\,\mathrm{Mg\,m^{-3}}$, it is approximately 1.57 [1]. Liquid water on the other hand has a very high dielectric constant of around 80 [24], practically blocking the penetration of microwaves, which leads to fundamental differences between dry and wet snow [11].

The dielectric constant moreover influences the emissivity ϵ, as defined in (2.6), which describes how efficiently a material radiates energy in comparison to a blackbody. When an electromagnetic wave propagates through a dielectric material, it inevitably undergoes

an energy loss that is also referred to as attenuation [11]. The lower ε_r' and the more transparent the medium, the smaller the loss. A low dielectric constant therefore roughly translates into high emissivity, and vice versa [24]. Because dry snow is comparatively transparent to microwave radiation having a very small loss factor i.e. very little absorption, the observed attenuation is dominated by scattering [1].

The scattering effect observed for dry snow, volume scattering, is highly dependent on frequency. Air acts as a surrounding medium for the ice particles which are on the order of millimetres, as stated earlier. For propagating waves with wavelengths much larger than the ice particle diameter, snow appears as a homogeneous medium without scattering but only absorptive effects [10]. For wavelengths of similar magnitude, the ice particles act as scatterers due to the inhomogeneity of dielectric properties of the ice itself and the air background [10]. Volume scattering leads to an attenuation in emissivity as well as in brightness temperature, see (2.6). The characteristic of dry snow that its emissivity decreases with increasing frequency is unique among land cover types [9]. It furthermore becomes evident that the emission from dry snow stems from different depths and thus is not simply described by a single emissivity [1].

Different aspects on the microwave emission of snow including environmental effects are visualised in Fig. 2.8. The emission is illustrated as vertical arrows of different thickness for different intensities. Volume scattering is represented as horizontal dashed arrows and the more arrows, the more scattering is present. Figure 2.8a illustrates how shallow snow depths not only cause an increase in emission due to less volume scattering, but also due to possible effects from the ground underneath as snow has only little absorption due to small ε_r''. Depending on the soil's properties, such as comparatively high temperature and wetness, the observed emission and hence the measured brightness temperature may be increased significantly. In addition, though independent on snow depth, overlying vegetation and trees reflect and emit upwelling microwave radiation [25], causing snow cover in forested areas to present higher emissivities and brightness temperatures than in unforested regions [8].

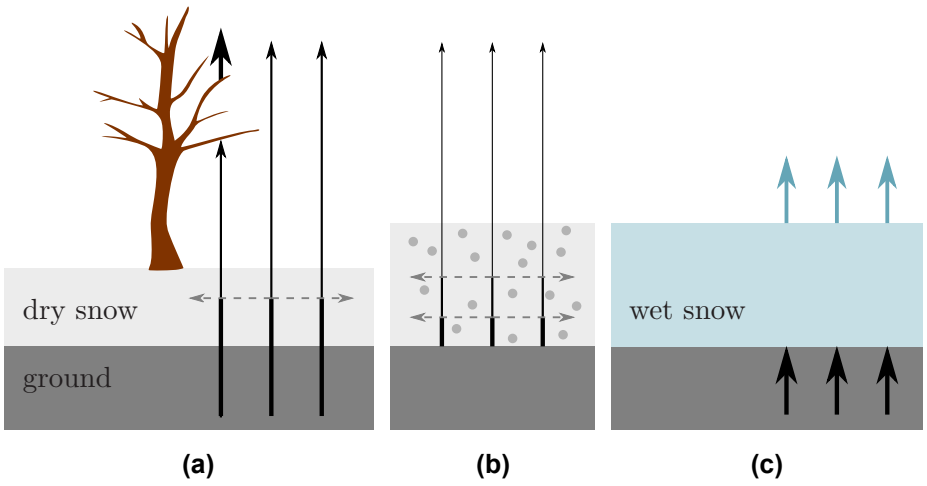

Figure 2.8. Schematic of the microwave emission from snow. The influence of different environmental conditions includes **(a)** soil under a thin snow layer and vegetation, **(b)** internal snow properties such as grain size and density, and **(c)** liquid water content of snow. Microwave emission is represented by vertical arrows of varying thickness according to its intensity; Volume scattering is represented as horizontal dashed arrows with more arrows indicating more scattering.

Further internal snow properties affect the emission, as shown in Fig. 2.8b for a deeper snow layer and without ground effects. The above mentioned effects of varying wavelength on scattering behaviour can be directly translated to snow grain size. The higher the frequency and/or the larger the grain size, the more scattering is observed as the particle size approaches the wavelength [2], [14]. The shape of the snow crystals on the other hand has nearly no impact [26]. Besides the grain size, snow density has a similar effect, and since both generally increase for aging snow, the emission is more attenuated for older snowpacks [8].

In contrast to dry snow, wet snow has a high dielectric constant i.e. it is less transparent to microwave radiation causing much less effects from the underlying soil on the emission, see Fig. 2.8c. Despite its large dielectric constant, melting or wet snow has a much larger emissivity than dry snow. There is essentially no attenuation through volume scattering due to the much smaller size of liquid water droplets in comparison to ice particles [11]. Instead of volume emission, the absorption and emission effects on the surface dominate [1], and the emissivity spectra of wet snow are therefore significantly different from the ones of dry snow [9]. The arising challenges for snow PM remote sensing are discussed in the following section.

2.3 Global-Scale Snow Cover Mapping

In this section, approaches and limitations for passive microwave remote sensing of snow are discussed in more detail, followed by dry snow detection algorithms using exclusively PM data. Finally, common global and hemispheric snow products using various data types are introduced.

2.3.1 Passive Microwave Remote Sensing of Snow

Dry snow is often detected by the use of multi-spectral and/or multi-polarization methods. The use of two or more PM bands enables the detection of attenuation effects as found for snow-covered surfaces [2]. Essentially, the contribution in emissivity from the dry snow layer itself is most of the times negligible, because of its low emissivity in comparison to the soil underneath [2] (compare to Fig. 2.5). The emission of the soil, in turn, is attenuated by the snow cover due to volume scattering. The magnitude of the attenuation is dependent on microwave wavelengths, and lower brightness temperatures are measured for higher frequencies in the presence of snow. This brightness temperature difference between different frequency bands can be related not only to snow presence but also to snow depth and SWE. A further benefit in using multiple bands over a single frequency is that unwanted effects are reduced or possibly eliminated [7]. Those include, for instance, variations in physical temperature of the instrument that affect the measured signal or systematic errors, if a common calibration target is chosen for all channels [7].

The difference in brightness temperature, and equally in emissivity ϵ, between two different frequencies is shown in Fig. 2.9. Modelled emissivities for snow depths of 0.1, 0.5 and 1.5 m are given for 10 and 37 GHz, and the overall drop in emissivity from Fig. 2.9a to Fig. 2.9b is apparent for both polarisations. The emissivity curves corresponding to 10 GHz barely differ from each other. For 37 GHz, emissivities are overall lower and are clearly sensitive to snow depth: the deeper the snow, the lower the emissivity due to increased volume scattering. However, snow depths of more than about 1.25 m become problematic as the maximum observable scattering is reached which results in signal saturation [14]. Since no variations in scattering are present anymore for deep snow, snow depths cannot be estimated correctly using the brightness temperature difference. Snow is now the primary emitter [14], and its emissivity starts to increase for increasing snow depth [9].

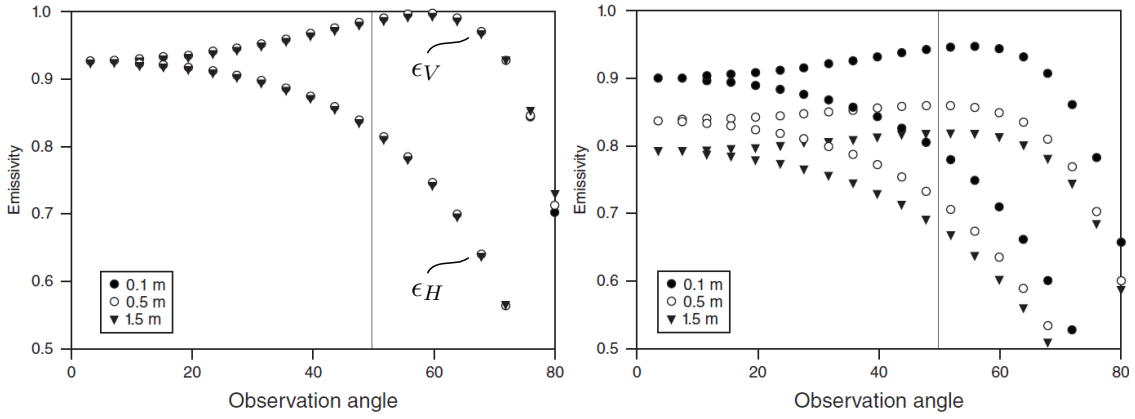

(a) 10 GHz **(b)** 37 GHz

Figure 2.9. Modelled snowpack emissivity at 10 and 37 GHz versus observation angle, adapted from [2]. Emissivities are given for different snow depths of 0.1, 0.5 and 1.5 m, for vertical and horizontal polarisation. The emissivity ϵ_V of vertical polarisation is generally larger than ϵ_H of horizontal polarisation, as indicated for exemplary ϵ_V and ϵ_H of the same observation angle in **(a)**; the same behaviour is transferable to the emissivity curves shown in **(b)**. The used model is based on the dense medium radiative transfer theory and accounts for multiple volumetric scattering, with snow and ground temperatures of 271 K, snow particle radius of 0.5 mm, snow density of 0.3 Mg m^{-3} and relative permittivity of frozen soil of $4 + 0.1i$. The 50° observation angles are marked by a vertical line.

Figure 2.9 also highlights the view dependency of the emissivity $\epsilon(\theta, \phi)$, see (2.6). For an observation angle of 50° which is about the incidence angle of SMMR, SSM/I and SSMIS and of the radiometer measurements by Mätzler [9], the emissivities of different polarisations can be clearly distinguished. The emissivity is generally higher for vertical than for horizontal polarisation, though this difference gets smaller and essentially vanishes for small angles i.e. for a viewing direction approaching nadir. An increase in observation angle above around 60° on the other hand leads to a rapid decrease in emissivity, less ability to discriminate between snow depths and as a result to a loss in information.

For a fixed observation angle of 50°, Mätzler measured the emissivities of different media as shown in Fig. 2.10. A significant reduction in emissivity is observed for dry snow with frequencies above 10 GHz due to volume scattering, often referred to as scattering signature. The scattering signature is more prevalent for medium than for shallow snow, indicating its sensitivity to snow depth. Even though not all object classes of [9] are given, this negative spectral gradient is present for all snow types with a dry surface. Nevertheless, for fresh powder snow with a depth of 37 cm and SWE of approximately 4 cm, the scattering effect appears only at higher frequencies above 35 GHz because of generally very small grain sizes. Consistently wet or melting snow, in contrast, has a high emissivity and can thus be hardly discriminated from bare (wet) or frozen soil, regardless of polarisation.

The polarization difference at and below 10 GHz shows a (small) monotonous increase with increasing SWE [9]. This can be seen in Fig. 2.10 for 5 and 10 GHz, since ϵ_V is roughly the same for medium and shallow snow, whereas ϵ_H is clearly lower for medium than for shallow snow. Though in comparison to higher frequencies, emissivities and equivalently brightness temperatures measured at or below 10 GHz are barely responsive to snow depth.

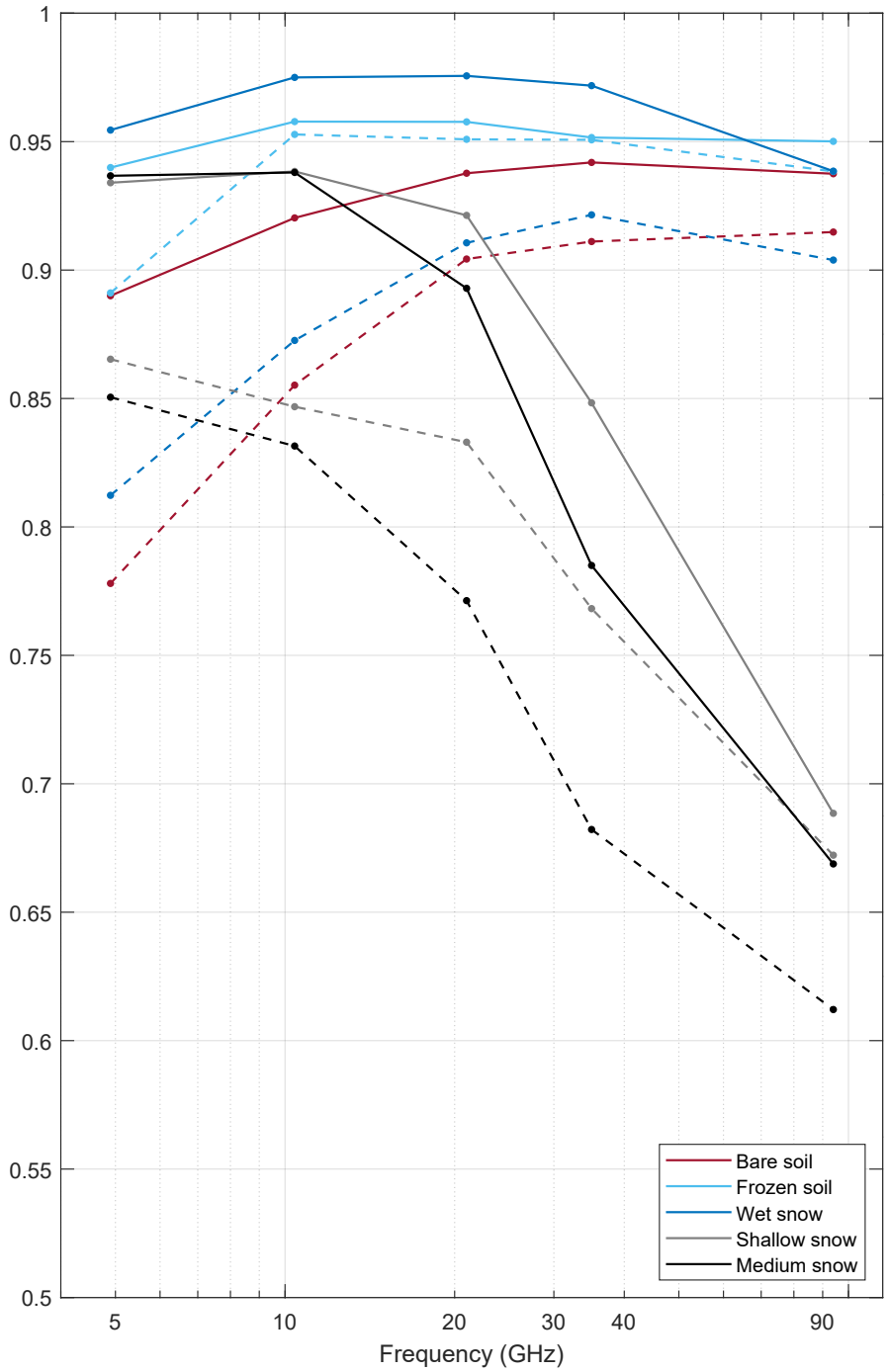

Figure 2.10. Measured emissivity spectra of snow and other object classes at 50° off nadir, after [9]. Mean emissivity values of vertical and horizontal polarisation, ϵ_V and ϵ_H, are plotted for 4.9, 10.4, 21.0, 35.0 and 94.0 GHz as solid and dashed lines, respectively. The object classes include different types of soil and snow: 'Bare soil' represents nine snow-free observations in wet and dry, warm and cold conditions (unfrozen only); 'Frozen soil' represents two situations of frozen bare soil of mostly frozen soil moisture of about 40% by volume and with surface temperatures of −6 °C and −1 °C, respectively; 'Wet snow' represents 53 situations of wet snow having at least a wet surface layer; 'Shallow snow' represents 11 situations of dry snow with SWE between 4 and 10 cm; 'Medium snow' represents 12 situations of dry snow with SWE between 10 and 25 cm.

Those lower frequencies serve as 'scatter-free' references to reduce the effects of ground temperature and atmospheric quantities on changes in brightness temperature [13], [27]. In order to detect the scattering signature of snow, T_B differences of different channels can be applied, using a channel that is not sensitive to scattering and a channel that is sensitive to scattering. Available bands of SMMR, SSM/I and SSMIS may differ from the exact frequencies shown in Fig. 2.10, nonetheless, the overall scattering behaviour remains. A 10-GHz channel as scatter-free reference is only available for SMMR and therefore 18/19 GHz are used instead. Using 19 GHz (SSM/I and SSMIS) over 18 GHz (SMMR) has only a very small effect on T_B-difference algorithms because the penetration characteristics are nearly identical for both frequencies at an incidence angle of 50° [28].

In addition to the scatter-free reference, 37-GHz data is generally best suited for snowpack studies [13], [27]. Between 18/19 and 37 GHz, the emissivity of frozen soil is estimated to stay on similar levels [7]; Fig. 2.10 confirms this when comparing 20 and 35 GHz not only for frozen soil but also bare soil and wet snow. For dry snow on the other hand, volume scattering leads to the already mentioned drop in emissivity. By subtracting T_B^{37} measured at 37 GHz from $T_B^{18/19}$ measured at 18/19 GHz, the attenuation in T_B caused by snow cover can be identified. This applies to both polarisations and either can be chosen for dry snow detection.

Limitations of this approach arise due other anomalous scattering signals, caused for instance by precipitation or cold deserts (e.g. Central Iran, the Gobi Desert or the Tibetan Plateau) [1], [25], or due to internal variations in snow properties, amongst other [2]. This includes for instance variations in grain size such as those resulting from depth hoar, large-grained crystals of up to 10 mm in diameter [29]. Within the snowpack, distinctive layers of snow are encountered which differ from each other in terms of e.g. density and grain size, and which as a whole are described as the so-called snowpack stratigraphy [30]. The horizontal polarisation of the 18/19 and 37-GHz channels is slightly more sensitive to the vertical variations caused by the snow's stratigraphy than the vertical polarisation [31]. Based on this, it could be derived that the vertical polarisation channels are more appropriate for snow depth estimations since they are less affected by the internal properties, whereas the horizontal polarisation channels are more responsive to those same properties and therefore more suitable for dry snow detection in first place [31].

Because the scattering effect is only marginal for thin snow packs, snow depths of less than about 3 cm are seldom detected [1], [13], [15]. To improve the sensitivity to thin snowpacks, brightness temperatures from high frequencies of 85 GHz and above can be included as those are subject to increased volume scattering [1]. According to Mätzler [9], those brightness temperatures should only be complementary due to the following: First, only a thin surface layer of the snow cover determines the actual emissivity given the small wavelength which complicates the detection of fresh powder snow due to higher emissivities than other dry snow types, as mentioned above; Second, the atmospheric transparency is variable and precipitating clouds can additionally show low emissivities that comparable to dry snow. The latter argument similarly speaks against the use of 21/22 GHz, which also suffers from effects of atmospheric water vapour and precipitation [8], [27]. Nevertheless, those channels may as well be used for complementary information [25].

A more general problem of snow remote sensing is that most of the Earth's seasonal snow cover occurs in complex landscapes which hinders the identification of snow cover using PM observations [1]. Mountainous terrain is challenging for several reasons. Generally, large spatial differences in snow depth are expected and whilst deep snow eventually reaches the saturation depth, the signal of shallow snow prevails due to higher emissivity. Moreover,

complex topography with significant changes in slope gradient causes variations in (local) observation angle within the sensor footprint and thus variations in emissivity [2], since the latter is view-dependent as seen in Fig. 2.9. Apart from mountains, liquid water poses a key challenge both within the snow itself and in form of water bodies. Large waters such as oceans and large lakes are therefore commonly masked out, as well as pixels that cover a large percentage of water e.g. in coastal areas or lakeland. The internal wetness of snow on the other hand not only affects PM seasonal snow detection, but also the capability for PM snow accumulation monitoring. Even though PM remote sensing can be used to retrieve accumulation rates in the dry-snow zone of ice sheets, it is greatly limited by spatial and temporal variability in liquid water and refrozen subsurface ice structures [2], and relies highly on in situ measurements [1]. An additional classification for glacial ice might need to be introduced since common scattering signatures for snow detection can result in a lack of scattering for large regions of Greenland and Antarctica [25].

Major discrepancies also arise for the presence of vegetation and especially of forest cover [12], as described in Section 2.2.2. Typically, horizontal polarisation channels are more sensitive to vegetation [14], however, the underestimation of snow due to forests masking out snow cover affects both polarisations [3]. The interpretation of PM signals for snow mapping on hemispheric or global scale is hence hindered by significant regional variations, for instance in terrain elevation and land cover. Overall, PM approaches tend to underestimate snow extent [1], [32].

In order to achieve consistent accuracy in SCE and SWE estimates across all of the Northern Hemisphere, either physical approaches, including robust snow pack parameterisation, or regional approaches are required [2]. The latter may involve algorithms for particular regions, e.g. for the Himalayas [33] or Western Canada [34], or hemispheric but regionally-tuned algorithms, e.g. by Foster et al. [14]. Armstrong and Brodzik [35] state that, in general, horizontal polarization-based algorithms achieve the best SCE estimates on hemispheric to global-scale throughout the snow season. Algorithms of vertical polarization obtain similar results but have the tendency to overestimate snow cover particularly if desert soils and/or frozen ground are present.

2.3.2 Dry Snow Detection Algorithms using Passive Microwave Data

The algorithms applied in this thesis are presented according to the year of their publication, and are referred to by their first authors' name(s) since they have usually no specific names given. All methods apply to dry snow conditions only and are static, disregarding temporal variations for instance in snow grain size or snow density. PM algorithms for dry snow detection are generally based on the spectral gradient between a 'non-scattering' and a 'scattering' channel, typically 18/19 GHz and 37 GHz respectively, so that a positive difference in brightness temperature indicates the presence of a scattering medium like snow [13], [36].

Chang et al. (1987)

Based on SMMR data, Chang et al. [13] first introduced the relationship between snow depth and brightness temperature for a uniform snow field as:

$$\mathrm{SD} = R_c \cdot \left(T_B^{18H} - T_B^{37H}\right) \tag{2.10}$$

with constant (linear) regression coefficient $R_c = 15.9\,\mathrm{mm\,K^{-1}}$ and brightness temperatures at 18 and 37 GHz for horizontal polarisation H, as indicated by the corresponding superscripts. A snow density of $0.3\,\mathrm{Mg\,m^{-3}}$ is assumed, and the authors furthermore note that the application of (2.10) should be limited to snow depths of less than 1 m. If $\mathrm{SD} \geq 25\,\mathrm{mm}$, the observation is marked as snow.

Grody and Basist (1996)

Grody and Basist [25] introduce additional frequencies for snow detection, namely the 22 and 85-GHz channels of SSM/I. The presence of scattering is determined based on the scattering signature relationships:

$$T_A^{22V} - T_A^{85V} > T \tag{2.11a}$$

OR

$$T_A^{19V} - T_A^{37V} > T \tag{2.11b}$$

which may also be referred to as SCAT for the varying temperature threshold T. In contrast to (2.10), (2.11b) utilizes the vertical polarisation V.

Equation (2.11a) is generally sufficient to detect snow, though the additional test in (2.11b) is beneficial in case of significant cloud liquid water. The decision tree as shown in Fig. 2.11 is developed to identify and discriminate between further scattering materials. Once a scattering medium is detected in (2.12a), precipitation, cold deserts and frozen ground are filtered out by the conditions given in (2.12b) to (2.12d).

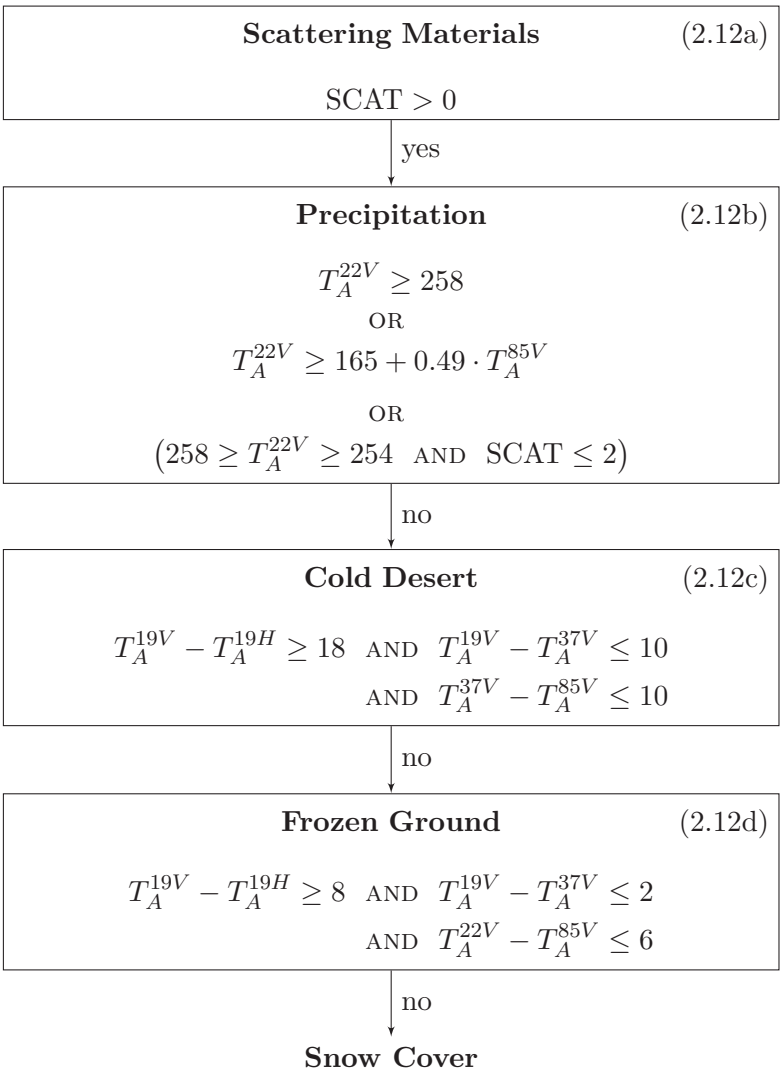

Figure 2.11. Decision tree used to differentiate between scattering sources, based on [25].

Note that the authors use antenna temperatures T_A instead of T_B [25]. To account for this, corrections have to be applied to brightness temperature data for the 19, 22, 37, and 85-GHz channels by subtracting 7, 6, 4, and 3 K, respectively.

Foster et al. (1997)

Foster et al. [14] propose for SMMR data the GSFC 1996 algorithm, named after the Goddard Space Flight Center of the National Aeronautics and Space Administration (NASA). Here, the effects due to vegetation cover are accounted for by including a forest cover parameter:

$$\mathrm{SD} = \frac{R_c}{1-p}\left(T_B^{18H} - T_B^{37H}\right), \tag{2.13}$$

with forest cover fraction p. The authors expect grain sizes to be slightly larger on average for interior areas of Eurasia in comparison to interior areas of North America. Therefore, R_c is set as $7.8\,\mathrm{mm\,K^{-1}}$ for interior areas of Eurasia and remains $15.9\,\mathrm{mm\,K^{-1}}$ elsewhere, assuming grain sizes of 0.4 mm and 0.3 mm, respectively. The interior regions of Europe are defined as boreal and transitional forest. The latter is understood to be forest as transition between boreal and deciduous forest.

Armstrong and Brodzik (2001)

Armstrong and Brodzik [37] introduced an adjustment of −5 K to (2.10) in order to compensate for the central frequency difference between the channels of SMMR and SSM/I. For SSM/I data, snow is now detected if:

$$\mathrm{SD} = R_c \cdot \left(\left(T_B^{19H} - 6\right) - \left(T_B^{37H} - 1\right)\right) \geq 25\,\mathrm{mm}^2. \tag{2.14}$$

Hall et al. (2002)

A further modified version of (2.10) for SSM/I data was suggested by Hall et al. [15], with the purpose of creating a snow-mapping instead of a snow-depth algorithm:

$$\begin{aligned} \mathrm{SD} = R_c \cdot \left(T_B^{19H} - T_B^{37H}\right) &> 80\,\mathrm{mm} \\ T_B^{37V} &< 250\,\mathrm{K} \\ T_B^{37H} &< 240\,\mathrm{K}. \end{aligned} \tag{2.15}$$

Hall et al. found to this approach to be more reliable than (2.14) [15].

Modifications and Other Approaches

The GlobSnow SWE product (see Section 3.6) incorporates dry snow detection where the approach of Hall et al. [15] as given in (2.15) is applied to SMMR in addition to SSM/I and SSMIS data. The H11 product (see Section 2.3.3) of the Satellite Application Facility on Support to Operational Hydrology and Water Management (H SAF), as part of the European Organisation for the Exploitation of Meteorological Satellites (EUMETSAT), provides snow status information (dry or wet) and also uses the relation in (2.15) for dry snow detection, but with the following empirically-derived criteria:

$$\begin{aligned} \mathrm{SD} &> 30\,\mathrm{mm} \\ T_B^{37V} &< 255\,\mathrm{K} \\ T_B^{37H} &< 250\,\mathrm{K}. \end{aligned} \tag{2.16}$$

[2] The threshold of 25 mm is not specifically stated in [37]. Since the authors modified the approach of Chang et al. [13], it is assumed that the original SD threshold is kept.

Exemplary regional approaches, based on PM data, are developed for the Himalayas by Saraf [33], or for Western Canada by Derksen et al. [34] and (for airborne data) by Goodison [38]. A comparison of the approaches of Goodison [38], Chang et al. [13] and Grody and Basist [25] for the Northern Hemisphere is conducted by Armstrong and Brodzik [32] for the years from 1978 to 1999 for SMMR and SSM/I data. Che et al. [39] use the approach of Grody and Basist [25], amongst other, for regional dry snow detection in China[3]. Tait [40], on the other hand, derives a global approach for SWE estimation that is based on individual relationships between SWE and observed brightness temperatures for 16 different land-cover categories. Moreover, neural networks have been applied for snow cover mapping. Tedesco and Jeyaratnam [41], for instance, utilise climatological data, electromagnetic modelling together with artificial neural networks in order to estimate SD and a dynamic snow density scheme to convert SD to SWE. Tedesco et al. [42] use a technique based on artificial neural networks for the inversion of SSM/I brightness temperatures.

Note that not all existing dry snow detection methods based on passive microwave data are mentioned. The presented selection is considered to represent the most influential approaches, which may be developed for dry snow detection itself or as part of estimations in SD and/or SWE.

2.3.3 Global Snow Products

Besides the GlobSnow SWE product [7] (described in more detail in Section 3.6) which is based on SMMR, SSM/I and SSMIS data, other global SD/SWE products are the Global SWE product [36] using Advanced Microwave Scanning Radiometer - Earth Observing System (AMSR-E) data, or the Standard SD and SWE product [43] using AMSR-E and Advanced Microwave Scanning Radiometer 2 (AMSR2) data. However, the temporal coverage of the latter two is limited to the period from 2002 to 2011 [12]. AMSR-E has channels of horizontal and vertical polarisation at 6.9, 10.7, 18.7, 23.8, 36.5 and 89.0 GHz. The instrument, onboard NASA's Aqua satellite, was developed by the Japan Aerospace Exploration Agency (JAXA), as was its successor AMSR2 which is carried by JAXA's Global Change Observation Mission – Water (GCOM-W) satellite. Those three products keep auxiliary data sources to a minimum in order to limit error propagation [12]. In general, global SD and SWE estimates have snow detection and SD/SWE retrieval in common as one of the main processing steps [12].

In addition to PM data, optical data has been successfully used for snow mapping, for instance from the Moderate Resolution Imaging Spectroradiometer (MODIS) on Terra and (a nearly identical version of MODIS) on Aqua, both satellites of NASA. Since early 2000, snow cover has been estimated daily using MODIS with automated algorithms developed and updated at GSFC [44]. A further example for the use of optical data is JAXA's Northern Hemisphere daily SCE product [45] (described in more detail in Section 3.3).

The synergistic use of data or snow products, offers the benefit of incorporating the most reliable aspects of each [46]. Blended products may involve PM data together with visible, near-infrared data and/or active remote sensing methods [2], [12]. The Air Force Weather Agency (AFWA)/NASA Snow Algorithm (ANSA) [47], for example, is a blended global snow product derived from visible, passive microwave and active scatterometer satellite data. ANSA blends existing snow products derived from MODIS, AMSR-E and NASA's Quick Scatterometer into a single, daily product that provides SCE, fractional snow cover, SWE, the onset of snowmelt and the identification of actively melting snow cover. As the confidence for mapping SCE is greater for the MODIS product, it is used as default for

[3] It was noticed that the authors apparently apply the original T_A decision tree directly to T_B data without temperature corrections to account for the conversion between T_A and T_B.

snow detection. The PM product is used if MODIS data are affected by the presence of clouds or darkness. Fig. 2.12 gives an example of the ANSA product and highlights the susceptibility of optical data to environmental factors, given the large amount of bright-blue, dark-grey and green pixels.

A further blended approach, this time to map the snow state (wet or dry), is implemented by the EUMETSAT H SAF H11 product [48]. Binary snow maps of the EUMETSAT H SAF H10 product [49], derived from visible and infrared radiometry, are set to show wet snow. Dry snow is then detected as part of H11 by means of PM radiometry, using primarily data of AMSR-E onboard NASA's Aqua satellite or, if missing, of SSM/I and SSMIS.

A comprehensible review of global satellite-derived snow products is conducted by Frei et al. [46].

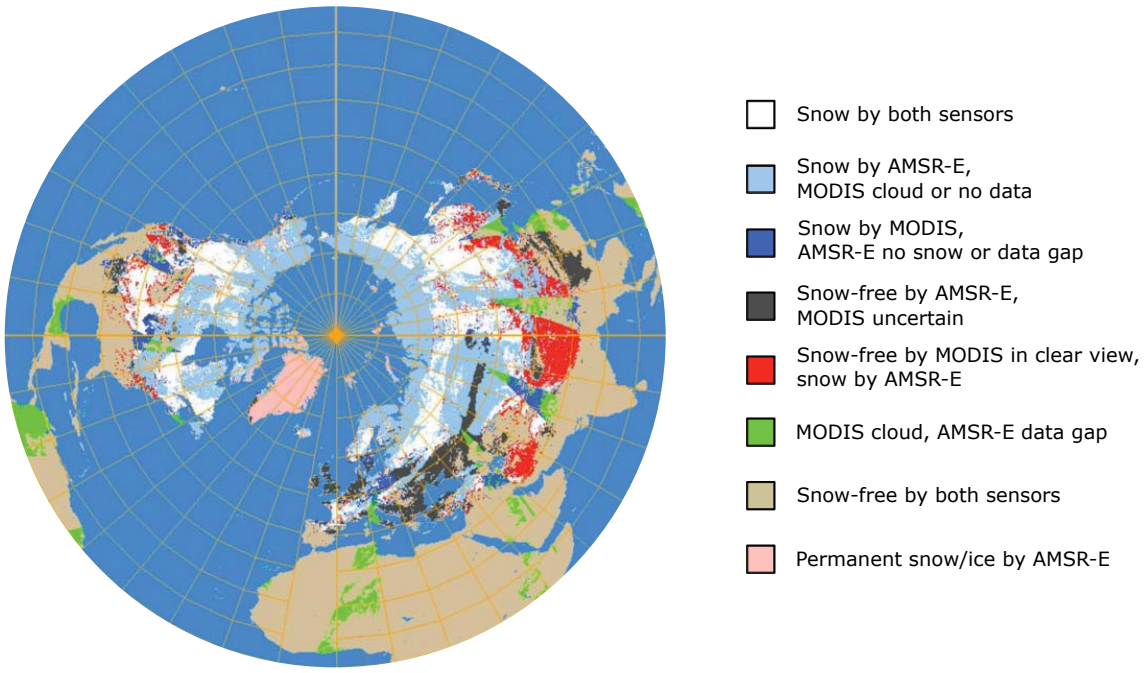

Figure 2.12. ANSA blended-snow product for 26 January 2007 in the Lambert Azimuthal polar projection [47], adapted from [2].

3 Data Records

This chapter lists the used data and introduces the applied data format. PM satellite data is described in Section 3.2 as well as reference data in form of optical satellite data in Section 3.3, a blended snow product in Section 3.4, and in situ SD measurements from weather stations in Section 3.5. Even though the GlobSnow SWE dataset as such is not used, it is described in Section 3.6 to provide context regarding its implementation of PM dry snow detection which is of interest for this project.

3.1 Data Format

All data are processed in the form of North azimuthal maps of the Equal-Area Scalable Earth-Grid (EASE-Grid) [50]. The format is adopted from the GlobSnow SWE product which uses the 25-km resolution of Northern Hemisphere EASE-Grid maps of (721×721) pixels, with the North Pole in the centre (the corners of the map fall outside of the Earth's projection). EASE-Grid is a versatile format for global-scale gridded data such as remote sensing data and as the name suggests, it provides equal-area maps without areal distortion. This means that by placing a small circle anywhere on the map, the same area on the globe is covered. Shape distortion may still be present, though the used equal-area projection minimizes it over the poles. A newer version of EASE-Grid is available but not used in this project, namely EASE-Grid 2.0 [51]. In the following, the 25-km Northern Hemisphere EASE-Grid map format may simply be referred to as 'EASE-Grid'.

3.2 Passive Microwave Satellite Data

The used PM satellite data are from the SMMR, SSM/I and SSMIS instruments, all conical scanners in near-polar orbits with incidence angles of approximately 50°. An overview of the PM sensors' relevant bands for dry snow detection is given in Table 3.1. The SMMR sensor was on board NIMBUS-7 satellite operated by NASA, with data available every other day from 1978 to 1987. It was succeeded by the SSM/I and later the SSMIS instruments with daily acquisitions as part of the Defense Meteorological Satellite Program (DMSP) aboard F-series satellites. SSM/I data applied in this thesis are from the spacecrafts F8 $(1987 - 1991)$, F11 $(1992 - 1995)$ and F13 $(1996 - 2008)$, whilst SSMIS data from F17 has been in use since 2009.

The radiometer observations, resampled to the Northern Hemisphere EASE-Grid projection, are acquired from the National Snow and Ice Data Center (NSIDC) [52], [53]. Both spatial and temporal data gaps may occur throughout the time series, though the coverage becomes generally more consistent for SSM/I and SSMIS data records and is usually on the scale of a few days only[1]. In addition, differences in local acquisition times between the different radiometers have to be considered. For SMMR, the equatorial crossing times are at midnight for descending, and at noon for ascending passes. For SSM/I and SSMIS on the other hand, the crossing times are approximately at 6:00 for descending and at around 18:00 for ascending passes. Since the focus is on dry snow detection, night-time and early-morning data from descending passes are prioritised if available, in order to keep the effect of liquid water in the snowpack on the brightness temperature to a minimum.

[1] The approach of Grody and Basist is the only algorithm that is affected by major data constraints. Due to compromised data integrity of the vertical 37-GHz channel, it is recommended to use data from the F18 instead of F17 satellite starting from 1 April 2016. However, F18 T_B data are not provided on the NSIDC portal and thus F17 data are used. Note that furthermore 85/91-GHz data are not available from 1 February 1989 to 31 December 1991 due to degradation of this channel.

Table 3.1. Sensor characteristics of SMMR [54], SSM/I [55] and SSMIS [56] channels relevant for dry snow detection.

SMMR	Centre Frequency (GHz)	**10.7**	**18.0**	**21.0**	**37.0**	
	Polarisation	V, H	V, H	V, H	V, H	
	Bandwidth (MHz)	250	250	250	250	
	FOV (km × km)	97 × 98	60 × 60	60 × 60	30 × 30	
SSM/I	Centre Frequency (GHz)		**19.35**	**22.235**	**37.0**	**85.5**
	Polarisation		V, H	V	V, H	V, H
	Bandwidth (MHz)		400	400	1 500	3 000
	FOV (km × km)		69 × 43	60 × 40	37 × 29	15 × 13
SSMIS	Centre Frequency (GHz)		**19.35**	**22.235**	**37.0**	**91.655**
	Polarisation		V, H	V	V, H	V, H
	Bandwidth (MHz)		350	400	1 500	1 400
	FOV (km × km)		72 × 44	72 × 44	44 × 26	15 × 9

Examples of brightness temperature data are given in Fig. 3.1 for 19 and 37-GHz channels of horizontal polarisation of SSMIS. Note the overall lower brightness temperature for 37 GHz, especially over the north of Siberia and Canada, due to snow cover. Note that the spatial integrity may vary between different days, channels and instruments. Besides SMMR data being generally available only every other day, as mentioned earlier, the swath width of SMMR is with 780 km [54] considerably lower than SSM/I with 1 400 km [55] and SSMIS with 1 700 km [56], and results in less spatial coverage.

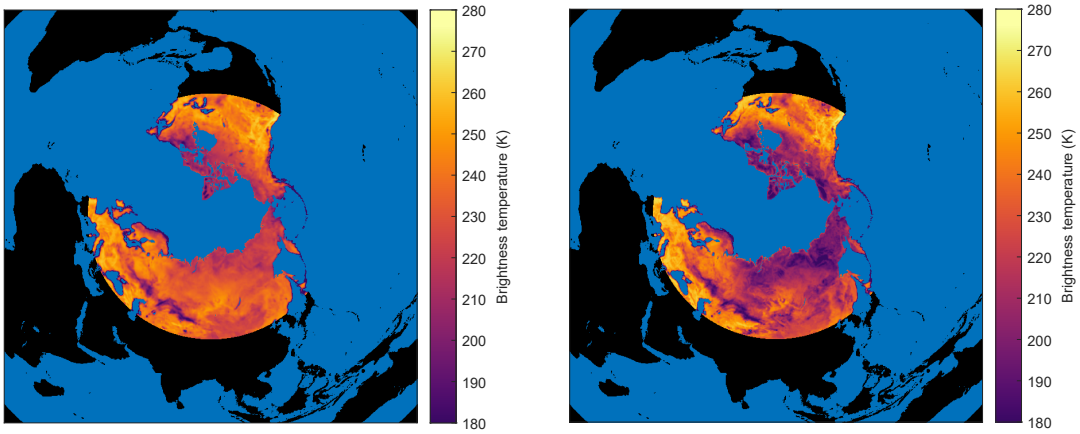

(a) T_B^{19H} **(b)** T_B^{37H}

Figure 3.1. Exemplary brightness temperature data of horizontal polarisation over land above 40° North on 15 January 2010.

3.3 Optical Satellite Data

For additional reference, the Northern Hemisphere daily snow cover extent product [45] is used, as provided by Satellite Monitoring for Environmental Studies (JASMES) of JAXA. The snow extent maps are derived from optical data by the Advanced Very-High-Resolution Radiometer (AVHRR) of the National Oceanic and Atmospheric Administra-

tion (NOAA) for the years from 1978 to 2005, and by MODIS onboard NASA's Terra and Aqua satellites for the years from 2000 onwards. The JASMES snow extent product with 5-km resolution is converted to daily snow masks with Northern Hemisphere 25 km EASE-Grid projection. For this, a 25% snow cover fraction threshold is used and the latest cloud-free observation per cell is retained in a cumulative manner.

3.4 Interactive Multisensor Snow and Ice Mapping System

The Interactive Multisensor Snow and Ice Mapping System (IMS) [17] of the United States National Ice Center (USNIC) provides a daily, analysis of snow and ice for the Northern Hemisphere and is one of the most widely used products for large-scale climate research [46]. The generation of IMS maps through the snow/ice cover algorithm involves preprocessing where all products and imagery in their original formats are collected. This includes AVHRR and MODIS Aqua/Terra imagery, SSM/I products, statistically modelled snow depth and global daily surface data readings, amongst other. Processed data are then displayed on IMS projection to analysts to tag snow and ice-covered locations to define the final snow line delineation. The human involvement is a key feature that distinguishes IMS from the other algorithm-based products [46]. The 24-km resolution IMS product for the Northern Hemisphere in American Standard Code for Information Interchange (ASCII) is chosen as reference, using data from 2007 until 2017 converted to EASE-Grid.

3.5 Synoptic Weather Station Observations

The same weather station data from various sources are used as for the GlobSnow product (see Section 3.6). Those are generally available for the years from 1979 to 2018, unless stated otherwise. Data of the European Centre for Medium-Range Weather Forecasts (ECMWF) are separated into Eurasia and North America components, and the former is complemented by data of the World Data Center of the All-Russia Research Institute of Hydrometeorological Information (RIHMI-WDC) covering the region of the former Soviet Union [57]. Daily Global Historical Climatology Network (GHCN) SD data [58] is the main dataset for North America in addition to ECMWF data. Further observations from the Meteorological Service of Canada ($1979-2018$) and from across the continental United States ($1979-2009$) [59] are applied.

Preprocessing involves filtering the individual datasets for duplicate observations. If the difference between latitude and longitude of the stations is less than 0.001°, the mean/median of two/multiple observations is used. Data are then combined into the synoptic Eurasia and North America datasets and again mean/median filtered. Duplicate observations are now detected if they fall within the same (25 km × 25 km) EASE-Grid pixel. In addition, negative as well as extremely high (> 500 cm) individual SD values are removed. Only SD values from long-term stations are kept that present at least 20 measurements for at least 5 separate years. Further median filtering is then once more applied to replace values that differ more than 20 cm from the median value over a 9-day window. For GlobSnow, stations where the measured SD is zero for more than 95% of the measurements are also filtered out. However, this step is not applied here in order to keep a reasonable amount of bare-ground, snow-free observations for reference. Neither are stations with unusually deep snow conditions typically in mountainous regions filtered out, nor for extreme slope conditions (mountain masking).

Due to the large number of observations of the North American dataset, further filtering is applied to only this dataset to allow more feasible computations. This data reduction step particularly addresses stations at lower latitudes. For latitudes between 30° and 45°, a 2° by 2° grid is created and the mean of all (filtered) SD observations for an individual

cell is used. Analogously, the mean is computed for latitudes from 45° to 50°, though here using a 1° by 1° grid. Data above 50° latitude are not reduced since observations are already sparse. After the filtering process, remaining weather station information is converted to EASE-Grid maps with available SD information in the corresponding pixels. To binarise SD information, pixels with SD = 0 cm are set to 0 (= snow-free) and with SD > 0 cm are set to 1 (= snow).

An example of the spatial distribution of weather stations across both North America and Eurasia is shown in Fig. 3.2, with a total of 2520 stations available on 15 January 2010. Note that the availability of weather station data varies on a daily basis, especially for Western Europe, and can be significantly less than in Fig. 3.2.

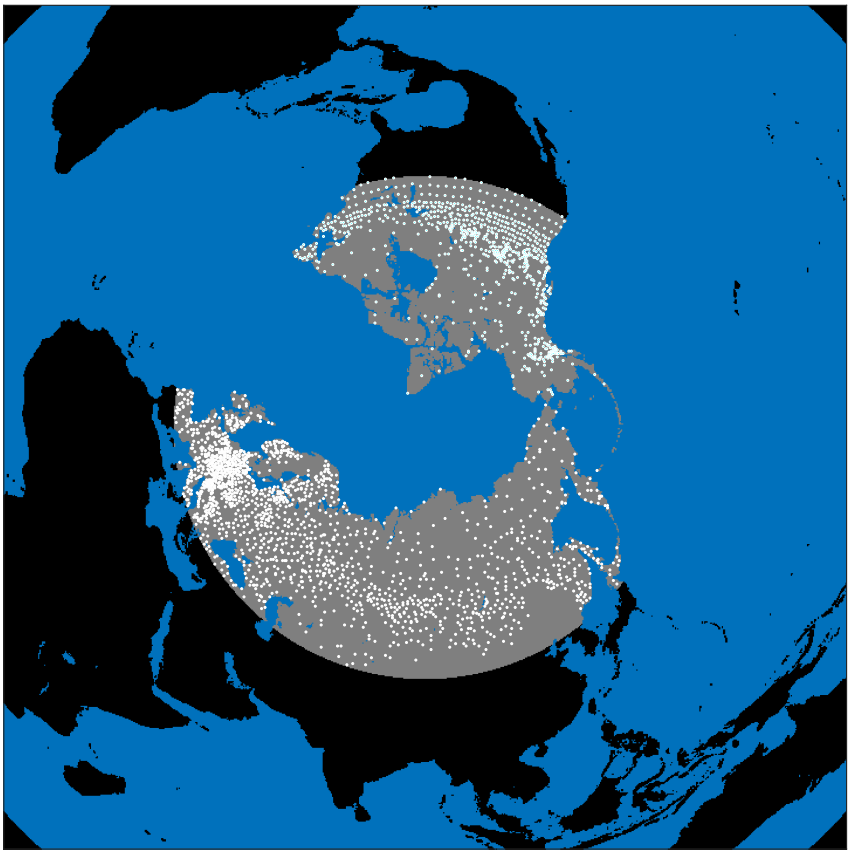

Figure 3.2. Exemplary weather station distribution in EASE-Grid. Stations are shown in white above 40° North (highlighted in grey) on 15 January 2010.

3.6 GlobSnow v3.0 Northern Hemisphere Snow Water Equivalent Dataset

The GlobSnow retrieval methodology combines spaceborne PM data with ground-based synoptic weather station observations through Bayesian non-linear iterative assimilation, and is primarily based on Pulliainen et al. [60] and Takala et al. [61]. The GlobSnow v3.0 SWE dataset and its methods are described in detail by Luojus et al. [7]. Using hemispheric snow course in situ reference data, the dataset is bias-corrected and used for the long-time analysis of patterns and trends of Northern Hemisphere snow mass by

Pulliainen et al. [4]. The trend determination is possible because GlobSnow v3.0 does not show a significant trend in systematic error, i.e. mean differences between SWE estimates and snow course measurements are statistically consistent over the full time series.

SWE is estimated on a daily basis, where SWE retrieval from satellite PM data is performed only for dry snow pixels. Vertical polarisations at 19 and 37 GHz are used over horizontal ones, due to better correlation with observed SWE in the boreal forest zone and due to decreased sensitivity to snow layering [7]. For wet snow pixels, SWE is estimated using the SD field derived from weather station observations. Prior to the SWE retrieval, PM dry snow detection determines snow pixels. During snow accumulation season in autumn (until December), a cumulative snow mask is computed (see Section 4.2). This allows for better tracking of the advancing snow cover extent. During snow melt season in spring, the cumulative snow mask is still used though the extent is reduced according to estimates for the end of snow melt season which are derived from PM data for each grid cell according to a time-series based snowmelt detection algorithm [62].

The simplified processing chain of GlobSnow v3.0 in Fig. 3.3 includes the following steps:

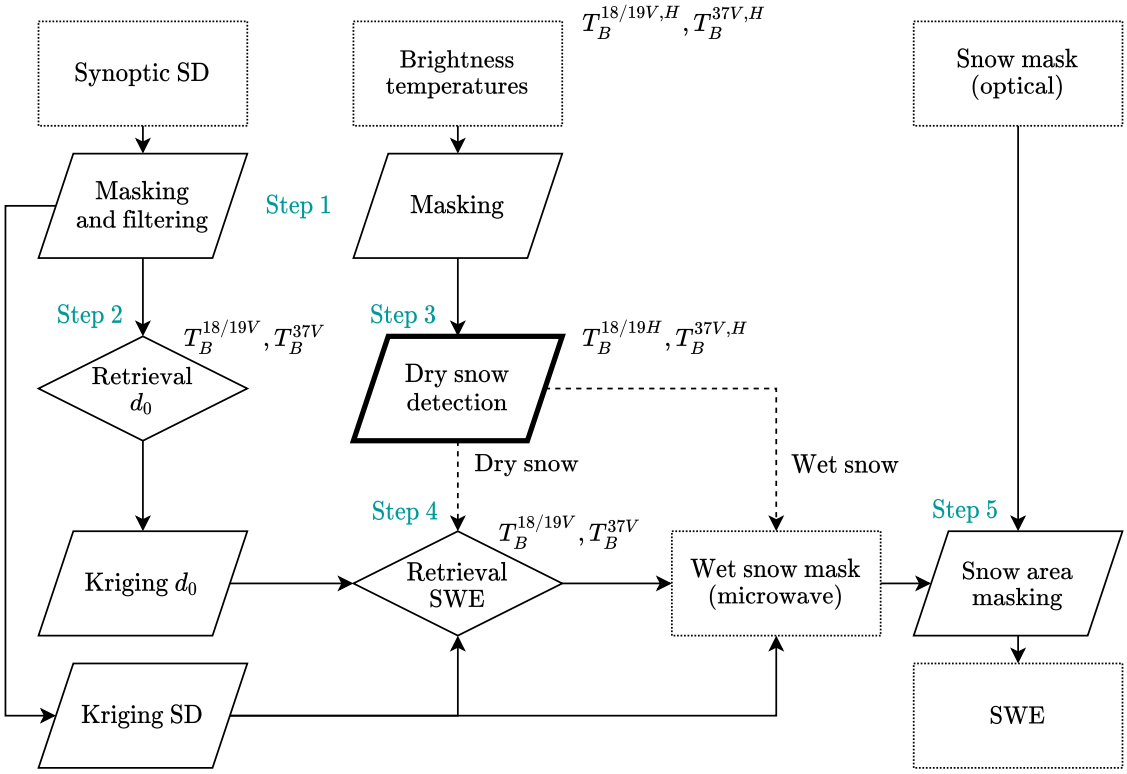

Figure 3.3. Processing chain for the GlobSnow v3.0 SWE product, simplified from [7].

Step 1: Both synoptic SD observations and satellite brightness temperature data are preprocessed. Synoptic SD observations are filtered and masked as described in Section 3.5, and mountain and water masking is applied to satellite data.

Step 2: The effective snow grain size d_0 is retrieved for grid cells with known synoptic SD through the numerical inversion of the multi-layer HUT snow emission model [60]. At the locations of weather stations, the HUT model is fitted to spaceborne T_B values, more precisely to $T_B^{18/19V} - T_B^{37V}$, by optimising d_0. After the retrieval, a spatially continuous field of d_0 is computed through kriging interpolation.

Step 3: Dry snow detection is performed according to Hall et al. using $T_B^{18/19H}$ and $T_B^{37V,H}$, see (2.15). If no dry snow is detected, wet snow (or bare ground) is present. The computed dry snow mask is applied to SWE retrieval (**Step 4**), and wet snow pixels get assigned a SWE value based on the spatially continuous SD field derived through kriging interpolation in order to create a wet snow mask.

Step 4: The retrieval of bulk SWE follows an assimilation approach similar to the d_0 retrieval (**Step 2**), again using numerical inversion of the HUT model. SWE are computed daily for dry snow pixels only, and fields of d_0 and SD (and their respective variance) serve as constraints. In addition, the weights of T_B data and of the SD field on the final SWE are adjusted (temporally and spatially) in order to obtain a maximum likelihood estimate of SWE.

Step 5: Ultimately, snow-free areas are detected and SWE values of affected (dry and wet) snow pixels are set to zero. The end of the snow-melt season is estimated through a time-series detection approach [62]. Moreover, snow masks from optical satellite data, namely JASMES [45] as described in Section 3.3, are used to detect snow-free conditions. Any affected grid cells are cleared.

3.7 Test Site and Auxiliary Datasets

The test site is equivalent to the Northern Hemisphere above 40° North, similar to [4]. Mountainous regions are included, but large water bodies are masked out. The focus is on the accumulation of snow as GlobSnow accounts for snow melt by detecting snow-free areas separately (see Step 5 in Section 3.6). Since an overall increase in SCE is observed for the months from September to about February inclusive, compare to Fig. 2.6, those six months are investigated and referred to hereinafter as 'snow accumulation season' or simply 'snow season'.

To ensure consistency within the different datasets, a mask is used to define land and water pixels. For this, the water fraction given by the ESA CCI Land Cover from 2000 [63] is aggregated from 300-m spatial resolution to 25-km EASE-Grid cells. Pixels with a water fraction $> 50\%$ are masked as water, since the proximity to water can lead to unreliable snow detection within heterogeneous cells covering both land and significant amounts of water. Using the water mask weather stations are filtered out that are on small islands or too close to water bodies. In addition, Greenland and Iceland are disregarded since the focus is on terrestrial seasonal snow and not on snow accumulation and glaciers as is mainly the case for Greenland and Iceland.

Additional forest cover information is required for the snow detection approach by Foster et al. given in (2.13). Both forest cover fractions and forest type classifications are derived from ESA GlobCover 2009 300 m data [64] and converted to EASE-Grid. The former was derived as part of the GlobSnow project and is shown in Fig. 3.4a. For the latter, boreal forest is defined if the fraction per pixel of Value $90 > 0.2$, where Value 90 describes open $(15 - 40\%)$ needleleaved deciduous or evergreen forest $(> 5\,\mathrm{m})$. Transitional forest is present if Value $90 > 0.15$ in addition to Value $50 > 0.1$, where Value 50 describes closed $(> 40\%)$ broadleaved deciduous forest $(> 5\,\mathrm{m})$. For both forest types, water (Value 210) has to be below a threshold of 0.25. Boreal forest is shown for both North America and Eurasia whereas transitional forest is derived for interior regions of Eurasia only, falling within longitudes between 5° East and 170° West. The resulting forest type map is shown in Fig. 3.4b.

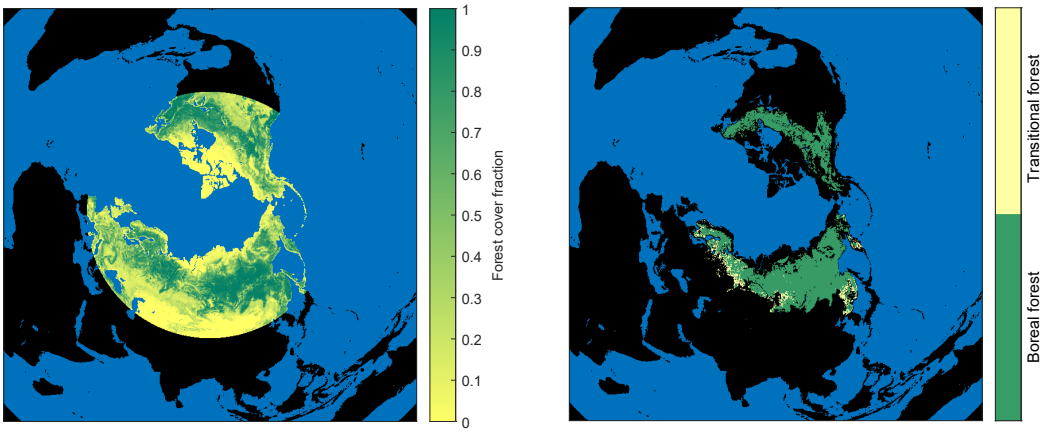

(a) Forest cover fraction map

(b) Forest type classification map

Figure 3.4. Forest maps in EASE-Grid. Maps above 40° North are derived from ESA GlobCover 2009 data [64].

4 Implementation and Evaluation

This chapter first introduces some general considerations and assumptions, and then elaborates on the computation of daily and cumulative snow masks, the evaluation of either with respect to reference data, and the meaning and computation of difference maps.

4.1 Considerations

In this project, a snow season covers the months September until February. For the analysis of the different PM methods, snow seasons will be split into the two time spans of SMMR, and of both SSM/I and SSMIS. This division is applied to avoid error propagation since methods usually perform worse for SMMR data, and to account for the different instrument properties causing not all approaches to be applicable to SMMR data. Grody and Basist [25] require channels only available for SSM/I and SSMIS, and Armstrong and Brodzik [37] specifically account for the difference in channel central frequency between SMMR and SSM/I (or SSMIS) to make use of data of the latter. Neither of the two approaches is thus evaluated for the SMMR period.

Even though PM methods are generally not accurate for extreme terrain and urban areas [12], both regions are kept. To ensure conformity of snow masks derived from different datasets, masks are applied to define the same land and water pixels for all. In addition, only latitudes including and above 40° North are considered analogous to [4]. Pixels are masked out if the geographical location of their centre falls below this latitude threshold. The resulting region of interest is highlighted in grey in Fig. 3.2.

The detected dry snow is validated against the weather station observations on a pixelwise basis. It is assumed that each PM estimate per grid cell was equivalent in scale to the point SD measurement on ground, i.e. the point measurement is compared against the whole cell. Although EASE-Grid has a nominal cell size of 25 km × 25 km, the actual cell size is slightly larger with 25.067 525 km × 25.067 525 km (corrected for in EASE-Grid 2.0) [50], [51]. When computing the daily snow extent, the nominal size of 25 km × 25 km is used for simplicity. The absolute SCE is not directly of interest here, but rather the relative SCE when compared to reference data.

4.2 Snow Masks

All snow masks are computed as binary EASE-Grid matrices of (721 × 721) pixels with 0 as snow-free ground (or for pixels with missing data) and 1 as snow. For each PM method, the masks are computed for every day that radiometer data are available. Daily snow masks are computed by following Algorithm 1. In the 'compute' step the selected specific PM dry snow detection approach is implemented as described in Section 2.3.2, see equations (2.10) to (2.16).

Even though the performances of the algorithms presented in Section 2.3.2 have been compared against each other to some extent, see for instance [32], this typically involves daily snow masks. In the case of GlobSnow, however, cumulative snow masks are used to track the advance of snow extent [7]. This follows the assumption that no snow melt occurs during snow accumulation season and is additionally more robust to missing data, e.g. due to incomplete coverage of the Northern Hemisphere. Therefore, cumulative snow masks are computed for all PM dry snow detection approaches selected in this project according to Algorithm 2.

Algorithm 1. Computation of daily snow masks.

```
Require: radiometer data
  select dry snow detection algorithm
  for year = 1979 : 2017                          ▷ year at beginning of winter season
    find serial date numbers:
      start date = 1 September of year
      end date = 28/29 February of (year + 1)

    for day = start date : end date                          ▷ days of winter season
      if year < 1987
        SMMR
      else if year == 1987
        if Julian date of day < 190: SMMR else SSM/I end
      else (year > 1987)
        SSM/I or SSMIS                  ▷ SSM/I and SSMIS are stored together
      end

      load required channel and polarisation data of respective instrument
      compute daily snow mask by applying specific method (0: snow-free, 1: snow)
      save daily snow mask
    end
  end
```

Algorithm 2. Computation of cumulative snow masks.

```
Require: daily snow masks of selected dry snow detection algorithm
  cumulative snow mask = [ ]
  for year = 1979 : 2017                          ▷ year at beginning of winter season
    find serial date numbers:
      start date = 1 September of year
      end date = 28/29 February of (year + 1)

    for day = start date : end date                          ▷ days of winter season
      load daily snow mask
      cumulative snow mask = (daily snow mask) OR (cumulative snow mask)
      save cumulative snow mask
    end
  end
```

4.3 Evaluation Measures

PM snow masks are compared to reference data, including weather station, JASMES and IMS data. Anything outside of the area of interest is masked out for this. For pointwise SD measurements, this means in addition that only pixels are considered that correspond to the weather stations.

The pixelwise comparison of two binary SCE masks, where 0 equals snow-free and 1 equals snow, follows the confusion matrix given in Fig. 4.1. Pixels are divided into true positive (TP), false positive (FP), true negative (TN) and false negative (FN) observations.

		Reference Data	
		Snow	**Snow-Free**
Evaluated Method	**Snow**	True Positive (TP)	False Positive (FP)
	Snow-Free	False Negative (FN)	True Negative (TN)

Figure 4.1. Confusion matrix for the comparison of binary SCE information.

The observation classes are used to calculate the classification accuracy, sensitivity or TP rate, and specificity or TN rate of the evaluated method as

$$\text{accuracy} = \frac{\text{TP} + \text{TN}}{\text{TP} + \text{FP} + \text{TN} + \text{FN}} \tag{4.1}$$

$$\text{TP rate} = \frac{\text{TP}}{\text{TP} + \text{FN}} \tag{4.2}$$

$$\text{TN rate} = \frac{\text{TN}}{\text{TN} + \text{FP}} \ . \tag{4.3}$$

The three measures are computed on a daily basis, i.e. for each day of the investigated snow seasons. Those daily values in turn are used to derive daily means for each day, as well as additional monthly and total means of the accuracy.

TP and TN values are furthermore used to derive histograms showing the share of correctly identified pixels with respect to synoptic snow depth. The first and largest bin collects pixels that correspond to synoptic SD $= 0\,\text{cm}$, and its share of correct snow-free PM observations (TN). Other bins collect pixels with synoptic SD $> 0\,\text{cm}$, each with a width of 1 cm, and again the shares of correct snow PM observations (TP). Each snow bins covers its respective interval $(\text{SD}, \text{SD} + 1\,\text{cm}]$. Pixels of synoptic SD $> 50\,\text{cm}$ are set as $50\,\text{cm}$ since the affected observations are quite sparse. Binned pixels, both total number and correct share, are summed up for each day of the snow seasons of all investigated years.

To assess estimated SCE, the area of SCE is computed as the sum of all snow pixels per day times the area of a pixel as $(25 \times 25)\ \text{km}^2$. Afterwards, the daily mean SCE area is calculated for every day of the snow season for the winters from 2007/2008 until 2016/2017 and for all approaches. SCE estimations by the PM methods are then evaluated with respect to IMS data using mean absolute error (MAE) and root-mean-square error (RMSE):

$$\text{MAE} = \frac{\sum_{j=1}^{n} |\hat{y}_j - y_j|}{n} \tag{4.4}$$

$$\text{RMSE} = \sqrt{\frac{\sum_{j=1}^{n} (\hat{y}_j - y_j)^2}{n}} \tag{4.5}$$

for predicted value $\hat{y}$ (PM daily SCE mean) and reference value y (IMS daily SCE mean) of sample j (day of a snow season) with maximum number of predictions n (equal to the number of days j per snow season).

MAE characterises the average magnitude of errors between $\hat{y}$ and y, i.e. the accuracy of SCE estimated by the PM algorithms. It is a linear score where all individual differences are weighted equally. RMSE on the other hand is a quadratic score which gives more weight to large errors whilst also estimating the average magnitude of errors. For both measures it applies that the smaller its value the better. Since RMSE is always larger or equal to MAE, the greater the difference between them both, the greater the variance of the individual errors.

It has to be stressed that the evaluation using MAE and RMSE is not straightforward since the area is considered as a whole without discriminating between correctly and incorrectly detected snow pixels. This means that even a wrong SCE would lead to low values in MAE and RMSE. MAE and RMSE on their own thus not necessarily indicate how well the algorithm performs, though become meaningful together with the computed accuracy in (4.1) and difference maps (see Section 4.4). One could argue that comparing the area as a whole is misleading in this context; It is included in this comparison since MAE and RMSE are more intuitive and better known measures than absolute difference as discussed in Section 4.4. The latter directly indicates how well the PM algorithms resemble IMS data in terms of SCE.

4.4 Difference Maps

The purpose of difference maps is to highlight regional, pixelwise differences regarding the estimated SCE of the individual PM dry snow detection algorithms, since over- and underestimation may be characteristic for certain types of landscapes. IMS data of 10 snow seasons is chosen as reference because it is spatially complete i.e. snow presence is determined for every pixel on every day. It is thus considered to be more accurate than JASMES which in contrast suffers from missing data and has spatial data gaps filled with snow presence information from the previous day (or the last day when satellite data was available and snow presence was estimated).

The difference is expressed as the number of days per pixel where the algorithm deviates from the IMS estimate. This can be either in form of overestimating (positive value) or underestimating (negative value) snow presence with respect to IMS data. Difference maps for the whole snow season are computed according to Algorithm 3 through pixelwise subtraction of daily IMS maps from the algorithm's snow mask. The latter can be either daily or cumulative. To obtain monthly difference maps, the start and end dates as shown in Algorithm 3 are simply set as first and last day, respectively, of the month under consideration. When calculating the final difference of a pixel (at the end of a month or at the end of the snow season) which is then displayed in the difference map, both over- and underestimation are considered. This means that the same amount of overestimation cancels out underestimation, and difference maps hence present the overall tendency of a pixel per month or per snow season over 10 winters.

The total absolute difference, on the other hand, presents the actual difference (and not the tendency) by calculating how many pixels are different to the IMS map without differentiating between over- and underestimation. It is expressed in pixels, which are the ones that differ between the investigated PM algorithm and IMS data per month or per snow season over the course of 10 winters. For this, the absolute value of the daily difference is summed over all days and in the end over all pixels to get a single value. Naturally it is not discriminated between over- and underestimation. Note that pixel values that are 'Not a Number' (NaN) have to be omitted when computing the daily difference so that the total absolute difference of the whole time series equals the sum of the monthly absolute differences.

Algorithm 3. Computation of difference maps and total absolute difference.

Require: daily or cumulative snow masks of selected dry snow detection algorithm and IMS EASE-Grid maps
difference map = [ ]
absolute difference map = [ ]
for year = 2007 : 2016 ▷ year at beginning of winter season
  find serial date numbers:
    start date = 1 September of year
    end date = 28/29 February of (year + 1)

  for day = start date : end date ▷ days of winter season
    load daily or cumulative snow mask and IMS map
    daily difference = snow mask - IMS map
    ▷ omit NaNs when daily difference is used for calculating absolute difference

    difference map = difference map + daily difference
    absolute difference map = absolute difference map + |daily difference|
  end
end
save difference map
total absolute difference = $\sum$ absolute difference map

5 Analysis of Dry Snow Detection Methods

The following analysis is the first extensive assessment of dry snow detection approaches for the Northern Hemisphere using spaceborne passive microwave data. Exhaustive synoptic snow depth measurements across Eurasia and North America serve as reference, together with optical satellite data and detailed blended snow information. The time series of SD reference and satellite data span 40 years, from 1979 to 2018. The motivation is to enhance dry snow detection as part of the GlobSnow SWE retrieval methodology [7] by selecting the best-performing algorithm. Six PM algorithms for dry snow detection are investigated, namely the approaches of Chang et al. [13], Grody and Basist [25], Foster et al. [14], Armstrong and Brodzik [37], Hall et al. [15] which is referred to hereinafter as 'GlobSnow' since it is part of the current version [7], and of the H SAF (H11) product [48].

Algorithm performances are evaluated using the measures presented in Chapter 4, and the best results are highlighted in tables in bold. If applicable, analysis is split between the period of SMMR (winters from 1979/1980 until 1986/1987), and the period of SSM/I and SSMIS (winters 1987/1988 until 2017/2018). The emphasis is on the SSM/I and SSMIS instruments since channel data is still available to date and covers a longer time span overall. First, the algorithms' performances are evaluated with respect to synoptic weather station data, followed by a comparison of the resulting snow cover extent.

5.1 Accuracy of Algorithms using Synoptic Observations

Snow masks are first compared to pointwise synoptic snow depth measurements from weather stations. For SSM/I and SSMIS, Figs. 5.1 and 5.2 show the changes in mean daily accuracy over the course of a snow season for the individual algorithms using daily and cumulative snow masks, respectively. The equivalent figures for SMMR are given in Appendix A.1. Those figures present significant jumps in accuracy due to data availability every other day. This causes poor averaging especially since SMMR only covers eight winters and thus, for some days, data are available only for three or four years. Monthly and total means are presented for all instruments in Tables 5.1 and 5.2.

JASMES is chosen for additional reference and performs overall best with a total accuracy of 0.8289 for AVHRR and 0.8460 for MODIS data. MODIS outperforms AVHRR slightly which can be traced to radiometric and geometric correction issues of the latter as well as data gaps, amongst other [45]. Overall, JASMES daily means show the least fluctuation over the course of a snow season, as can be seen in Figs. 5.1 and 5.2. Of the PM algorithms, Grody and Basist comes closest to this with a total accuracy over 0.8 for both daily and cumulative masks for SSM/I and SSMIS. Of the algorithms that are applicable to all satellite data, H SAF performs best for both instruments when using cumulative snow masks, achieving an accuracy of around 0.8.

For the vast majority of algorithms, cumulative snow masks overall outperform daily ones with respect to total accuracy. On a monthly basis, higher accuracies are achieved for November to February. The only exceptions of these observations are Chang et al. and Foster et al. for SSM/I and SSMIS. At the beginning of the snow season during September and October, on the other hand, all algorithms perform better for daily masks. This supports the intention of using cumulative masks to track advancing snow extent

for a progressing snow season. The better handling of data gaps is also apparent from the smoother appearance of the curve of the daily mean accuracy. This indicates that cumulative masks are less influenced by daily data availability.

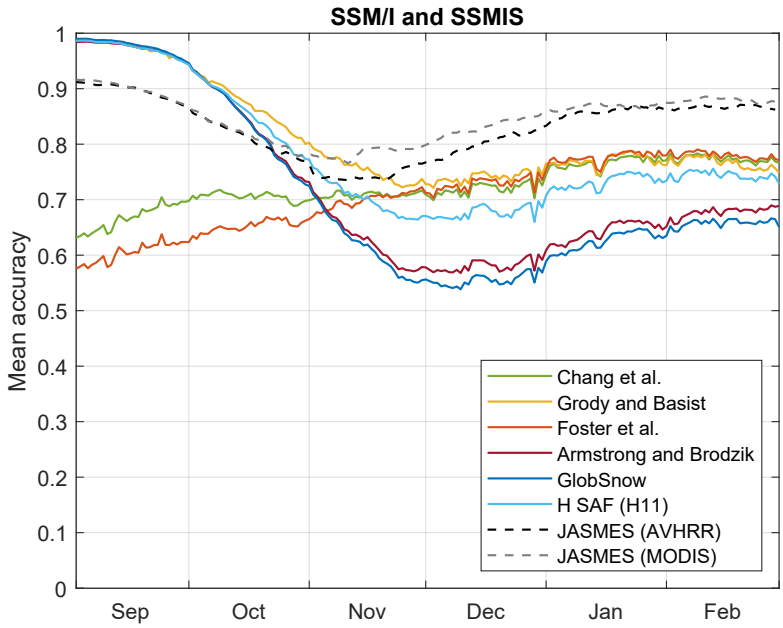

Figure 5.1. Daily mean accuracy over the course of a snow season for PM daily snow masks of SSM/I and SSMIS data and for optical JASMES masks of AVHRR and MODIS data with respect to synoptic weather station data.

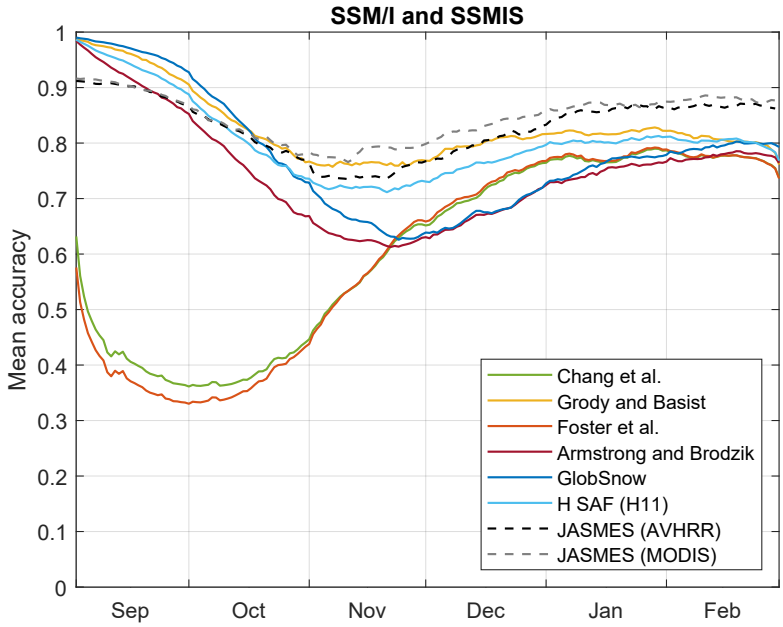

Figure 5.2. Daily mean accuracy over the course of a snow season for PM cumulative snow masks of SSM/I and SSMIS data and for optical JASMES masks of AVHRR and MODIS data with respect to synoptic weather station data.

Table 5.1. Mean accuracy of individual months and the complete snow season (total) derived from pixelwise comparison of PM daily snow masks with synoptic weather station data, and computed separately for the periods of SMMR and of SSM/I and SSMIS.

SMMR SSM/I, SSMIS	**Sep**	**Oct**	**Nov**	**Dec**	**Jan**	**Feb**	**Total**
Chang et al.	0.9524 0.6683	0.8358 0.7056	0.6269 0.7084	0.5749 0.7202	0.5536 0.7671	0.5925 0.7736	0.6948 0.7236
Grody and Basist	- 0.9742	- **0.8691**	- **0.7524**	- **0.7407**	- 0.7702	- 0.7667	- **0.8124**
Foster et al.	0.9372 0.6052	0.8339 0.6526	**0.6414** 0.6994	**0.5918** 0.7294	**0.5693** **0.7765**	**0.6035** **0.7799**	**0.7012** 0.7066
Armstrong and Brodzik	- 0.9727	- 0.8340	- 0.6253	- 0.5815	- 0.6434	- 0.6779	- 0.7228
GlobSnow	**0.9691** **0.9765**	0.8270 0.8321	0.5516 0.6135	0.4801 0.5561	0.4645 0.6257	0.5264 0.6582	0.6435 0.7107
H SAF (H11)	0.9653 0.9727	**0.8401** 0.8516	0.6164 0.7000	0.5623 0.6778	0.5425 0.7326	0.5846 0.7439	0.6910 0.7800

Table 5.2. Mean accuracy of individual months and the complete snow season (total) derived from pixelwise comparison of PM cumulative snow masks with synoptic weather station data, and computed separately for the periods of SMMR and of SSM/I and SSMIS.

SMMR SSM/I, SSMIS	**Sep**	**Oct**	**Nov**	**Dec**	**Jan**	**Feb**	**Total**
Chang et al.	0.8569 0.4212	0.7030 0.3894	0.6702 0.5699	0.7375 0.7163	0.8045 0.7751	0.8112 0.7739	0.7644 0.6058
Grody and Basist	- 0.9534	- **0.8241**	- **0.7631**	- **0.7998**	- **0.8200**	- **0.8056**	- **0.8275**
Foster et al.	0.7852 0.3853	0.6373 0.3701	0.6660 0.5711	**0.7474** 0.7221	**0.8162** 0.7780	**0.8143** 0.7744	0.7435 0.5983
Armstrong and Brodzik	- 0.9145	- 0.7477	- 0.6272	- 0.6734	- 0.7496	- 0.7766	- 0.7476
GlobSnow	**0.9527** **0.9660**	**0.8093** 0.8187	0.6140 0.6566	0.6400 0.6764	0.6993 0.7611	0.7717 0.7940	0.7519 0.7785
H SAF (H11)	0.9341 0.9384	0.8020 0.7982	**0.6971** 0.7214	0.7408 0.7654	0.7914 0.8044	0.8113 0.8019	**0.7983** 0.8047

For September, GlobSnow is the most accurate for both daily and cumulative masks. However the difference to Grody and Basist and H SAF, and for daily masks also Armstrong and Brodzik, is only minor. For October, Grody and Basist is found to perform best though the margin to H SAF for daily masks, and to GlobSnow for cumulative masks is again insignificant. A noticeable feature during September and October is the drop in accuracy for Chang et al. and Foster et al. when comparing daily and cumulative masks, each for SSM/I and SSMIS. This drop is not as significant for SMMR. Apart from those two, all algorithms have their maximum accuracy in September for both mask types.

With advancing snow season, the algorithms reach their minimum accuracy in November for cumulative masks. For daily masks, the minimum is shifted to December (SSM/I and SSMIS) or January (SMMR). Again, this is not necessarily true for Chang et al. and Foster et al. From November until February, Grody and Basist and Foster et al. are the overall best-performing algorithms, followed closely by H SAF using cumulative masks. As mentioned earlier, the time between October and November marks a changing point when the benefit of cumulative masks becomes evident. For increasing snow cover extent, cumulative masks counteract the general tendency of PM algorithms to underestimate snow presence.

5.1.1 Robustness of Snow and Snow-Free Classifications

Snow masks are again compared to pointwise synoptic snow depth measurements from weather stations. This time the algorithms' ability to depict snow and snow-free observations is assessed using TP and TN rate, respectively. The discrimination between snow and snow-free labels allows for the evaluation of their respective robustness and trends during a winter season, and highlights possibly biased sensitivities for an individual algorithm.

Figures 5.3 and 5.4 show the TP and TN rates over the course of a snow season for a selection of algorithms using daily or cumulative masks for SSM/I and SSMIS data. The behaviour of TP and TN rates for Chang et al. versus Foster et al., and for Armstrong and Brodzik versus Grody and Basist are very similar. Thus only the better-performing algorithm is given for each pair, namely Foster et al. and Grody and Basist. Complementary figures are given in Appendix A.2, including equivalent figures for SMMR data. For SMMR, very similar behaviour of TP and TN rates is observed.

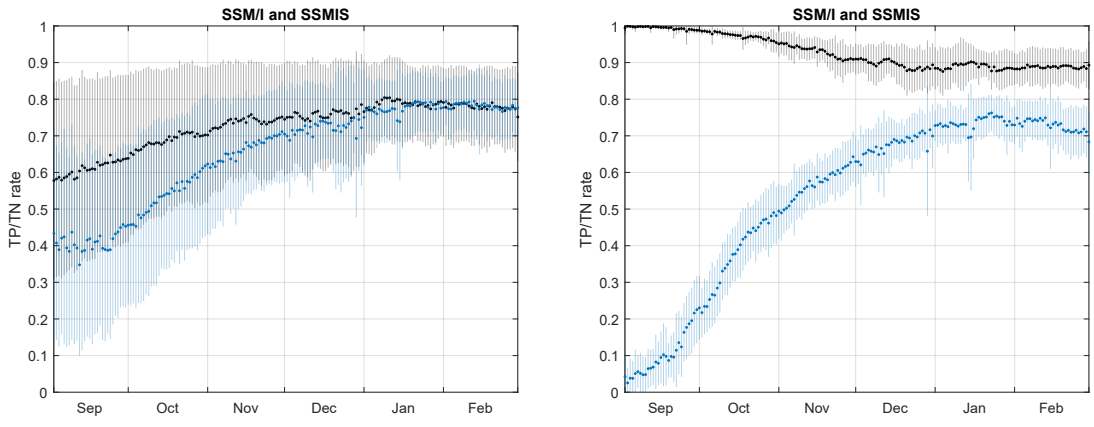

(a) Foster et al.

(b) Grody and Basist

Figure 5.3. Daily mean TP (blue) and TN (black) rate with error bars corresponding to one standard deviation over the course of a snow season for PM daily snow masks of SSM/I and SSMIS data with respect to synoptic weather station data.

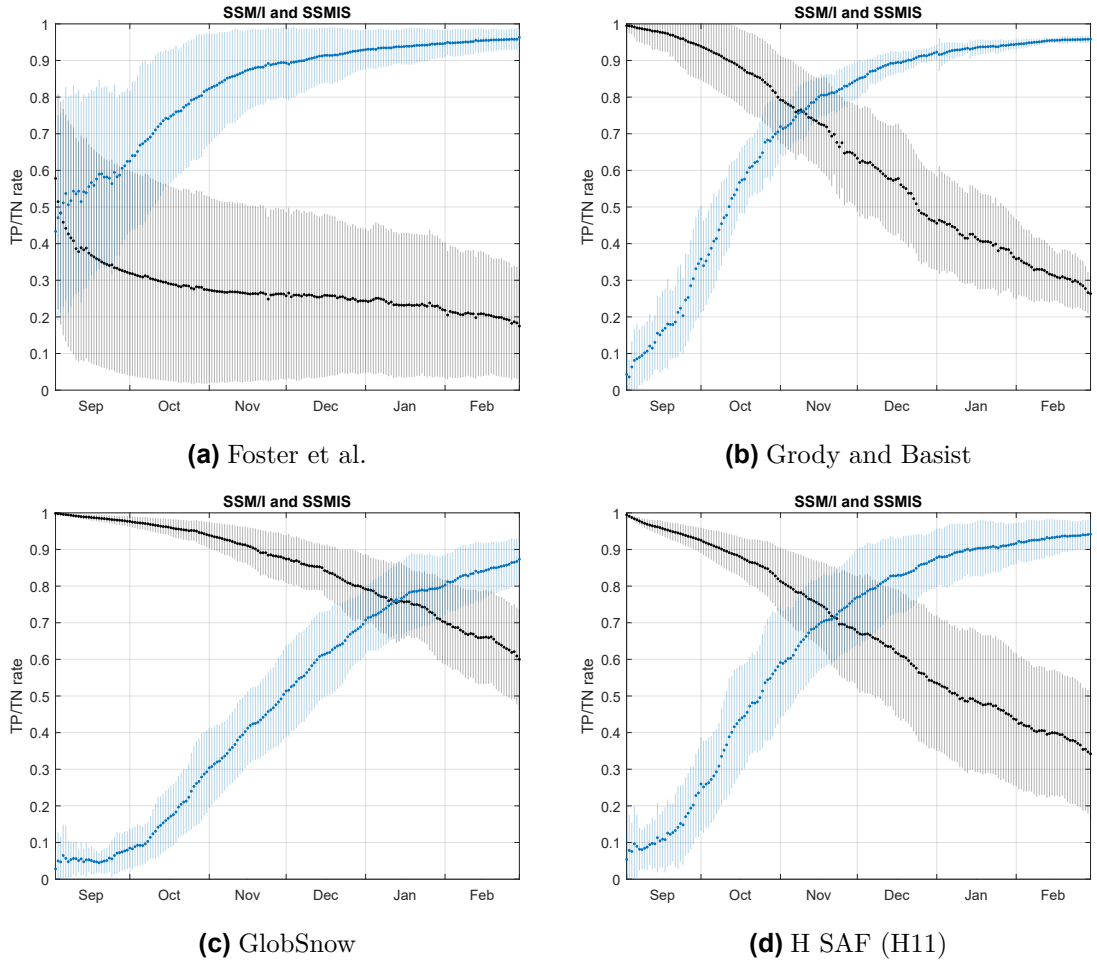

(a) Foster et al.

(b) Grody and Basist

(c) GlobSnow

(d) H SAF (H11)

Figure 5.4. Daily mean TP (blue) and TN (black) rate with error bars corresponding to one standard deviation over the course of a snow season for PM cumulative snow masks of SSM/I and SSMIS data with respect to synoptic weather station data.

As observed previously, cumulative snow masks generally outperform daily ones with respect to accuracy. Apart from Chang et al. and Foster et al., the algorithms present a similar behaviour, see for instance Figs. 5.3b and 5.4b. For daily masks, the TN rate stays high throughout the season with only a minor decline whereas the TP rate increases significantly albeit not reaching the same level as the TN rate. For cumulative masks, the decline in TN rate is steeper and the TP rate eventually surpasses the TN rate between November and January. This explains why cumulative masks dominate especially from November onwards: a high TP rate becomes more important with increasing snow extent.

The TP and TN rates furthermore clarify why Chang et al. and Foster et al. behave slightly different to the others in terms of accuracy. For daily masks, both the TP and TN rate grow over the course of a season and reach similar levels in January and February. For cumulative masks, higher TP rates are achieved, however, TN rates are reduced substantially. This behaviour is shown by Figs. 5.3a and 5.4a, and explains the low accuracy in September and October when applied to cumulative masks. It particularly affects SSM/I and SSMIS data which those algorithms were not originally designed for. Bareground synoptic observations dominate at the beginning of the season though those are often misclassified due to a low TN rate.

A high TN rate at the beginning of the snow season, in turn, leads inherently to an overall high accuracy. This explains why all other algorithms perform best for September and October as they present very high TP rates together with comparatively low standard deviations. Especially GlobSnow stands out with a TN rate close to 1 with very low standard deviations in September, see Fig. 5.4c, leading to the best accuracy for this month. But it is also the most conservative algorithm regarding the labelling of snow pixels, because its mean TN rate remains above 0.6 throughout the whole season and its mean TP rate does not surpass 0.9. This causes the sharp decrease in accuracy due to missing to detect the onset of snow, primarily for regions with higher density of synoptic measurements.

The benefit of the cumulative approaches of Grody and Basist and H SAF, which have been found to provide the best overall accuracy, lies in their high TN rate at the beginning of the season together with a steep increase in TP rate. The latter reaches around 0.7 and 0.6, respectively, by the end of October versus around 0.3 for GlobSnow, as shown in Figs. 5.4b to 5.4d. It continues to increase steadily until the end of the season, up to around 0.95 for both.

5.1.2 Sensitivity to Synoptic Snow Depth

To investigate the algorithms' sensitivity to true SD, the snow/snow-free classifications for all winters from 1979 to 2018 are binned depending on synoptic SD, as described in Section 4.3. Resulting histograms using cumulative masks of GlobSnow and H SAF are shown in Fig. 5.5 as example, all further histograms are given in Appendix A.3.

GlobSnow and H SAF share the same PM dry snow detection approach but use different thresholds of T_B and effective SD. The effect of those thresholds is well visible when comparing Figs. 5.5a and 5.5b: GlobSnow presents a very high confidence for bare-ground pixels with 91%, whereas H SAF reaches 78%. For snow pixels in contrast, H SAF identifies $> 50\%$ correctly for any SD whilst GlobSnow achieves this only for SD > 8 cm—in conformity with the SD threshold of its algorithm. A confidence $> 80\%$ is reached for SD > 29 cm for GlobSnow, and already for SD > 11 cm for H SAF. For comparison, Grody and Basist has an even higher sensitivity for snow pixels with $> 60\%$ for any SD and $> 80\%$ for SD > 5 cm. Bare-ground confidence is only slightly less than H SAF with 76%.

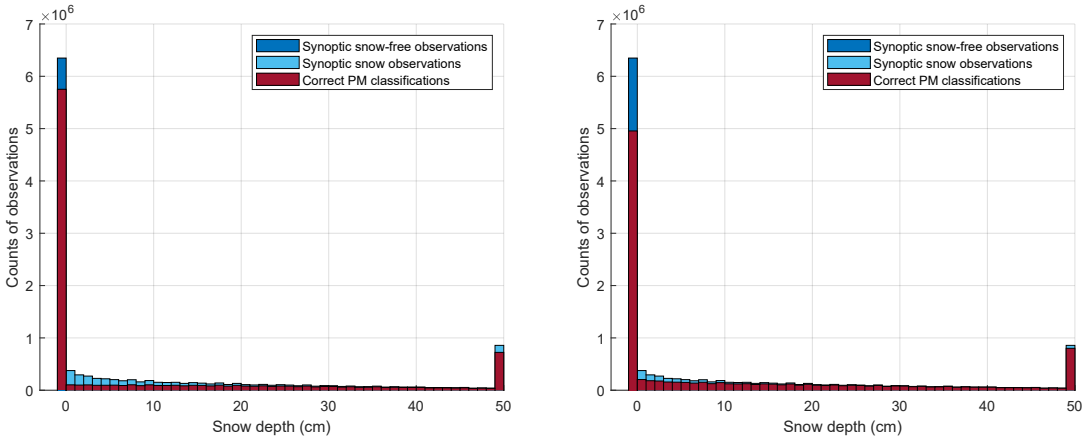

(a) GlobSnow **(b)** H SAF (H11)

Figure 5.5. Histograms of synoptic SD observations, and the share of correct snow/snow-free classifications for PM cumulative snow masks of SMMR, SSM/I and SSMIS data.

In general, the confidence to detect bare-ground pixels is worse for cumulative than for daily masks, but the confidence to detect snow pixels improves from daily to cumulative masks. This provides a further explanation for the overall increase in accuracy from November onwards, because deeper snow is better detected for all algorithms. The derived values are obviously only indicative due to pointwise nature of synoptic measurements, given that only a very limited number of pixels can be compared to in situ SD observations.

In addition to histograms of synoptic SD, histograms of effective SD with respect to weather station SD data are computed for GlobSnow and H SAF, see Appendix A.3. Any effective SD $> 50\,\text{cm}$ is again set as $50\,\text{cm}$. The distribution of effective SD differs considerably from the distribution of synoptic SD, not so much in terms of shape but absolute numbers (note the different scaling of the y-axis). If the algorithms were used to estimate SD and not simply snow presence, noticeable deviation from ground truth has to be expected. Besides, the initial purpose is to evaluate the current threshold of effective SD, see (2.15) and (2.16). However, no clear statement can be derived from the histograms and they are hence not further discussed. More investigation is required, also with respect to T_B thresholds since they are directly linked to effective SD.

5.2 Comparison of Snow Cover Extent

Snow masks from SSMIS data are compared to spatially-complete SCE maps from blended IMS data for 10 winters from 2007/2008 until 2016/2017. The daily mean area of SCE is shown in Figs. 5.6 and 5.7 over the course of a snow season for the individual algorithms using daily and cumulative snow masks, respectively. MAE and RMSE are computed for the daily mean SCE of PM approaches of both daily and cumulative masks with respect to IMS data, see Table 5.3.

JASMES data is also included and again performs best, with MAE of $3.7569 \times 10^6\,\text{km}^2$ and RMSE of $3.8065 \times 10^6\,\text{km}^2$. The curve progression of IMS is followed well as indicated by the small variance i.e. small difference between MAE and RMSE, whilst continuously estimating a higher SCE. This stands in contrast to PM daily masks, which resemble the IMS curve shape, too, but mostly predict (much) lower SCE—supporting the understanding that PM methods generally underestimate snow extent. As already noticed for total accuracies, the use of cumulative masks counteracts this behaviour and yields overall higher SCE and thus lower MAE and RMSE values.

Grody and Basist performs best for both daily and cumulative masks with MAE of about 4.0 and $2.5 \times 10^6\,\text{km}^2$, respectively, closely followed by Foster et al. for daily and H SAF for cumulative masks. Moreover, their variance is the lowest of all approaches. Particularly Grody and Basist match the IMS curve considerably well until December using cumulative masks. The cumulative effect results in a continuously increasing SCE, which eventually leads most algorithms to overestimate snow presence towards the end of the snow season, including Grody and Basist. Armstrong and Brodzik and GlobSnow, however, remain significantly below the IMS predictions throughout the whole season. It is only at the end of February that both reach similar levels in SCE, which is reflected by their poor MAE and RMSE.

When comparing the accuracy with SCE results, Chang et al. and Foster et al. once more deviate during September from the typical behaviour of IMS data as well as PM approaches. Both start off with a comparatively high initial SCE. For daily masks, their SCE prediction remains roughly constant, whilst for cumulative ones, a sharp increase is observed. Their monthly accuracy dropped noticeably between daily and cumulative snow masks, indicating that the cumulative effect is non-realistic.

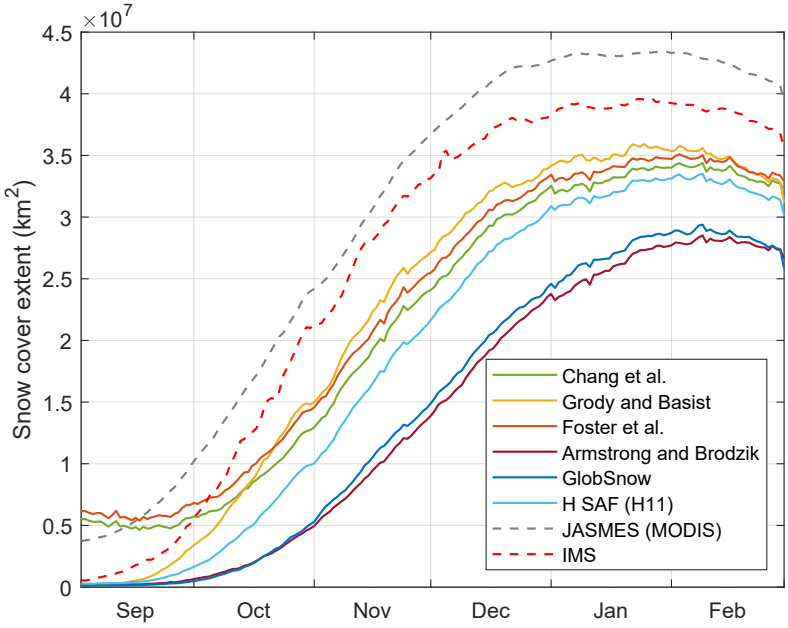

Figure 5.6. Daily mean SCE over the course of a snow season (winters from 2007/2008 to 2016/2017) for PM daily snow masks, optical JASMES masks and IMS data.

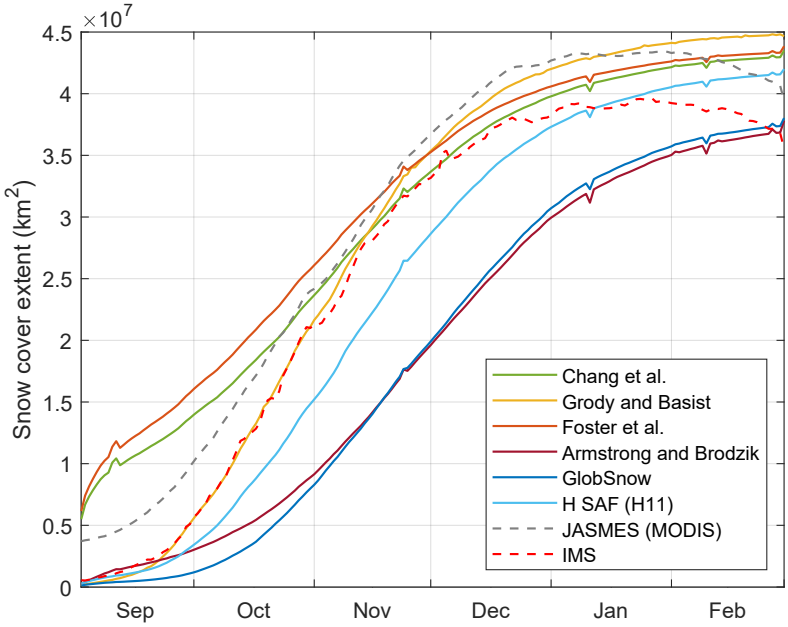

Figure 5.7. Daily mean SCE over the course of a snow season (winters from 2007/2008 to 2016/2017) for PM cumulative snow masks, optical JASMES masks and IMS data.

Table 5.3. MAE and RMSE of daily mean SCE from PM daily and cumulative snow masks with respect to IMS data.

	daily		cumulative	
	MAE (10^6 km^2)	RMSE (10^6 km^2)	MAE (10^6 km^2)	RMSE (10^6 km^2)
Chang et al.	5.7831	6.2456	3.6574	4.6670
Grody and Basist	**4.0486**	**4.3521**	**2.5082**	**3.3546**
Foster et al.	4.9929	5.3245	4.9990	5.8931
Armstrong and Brodzik	12.0829	13.3738	6.9935	8.5235
GlobSnow	11.4882	12.6641	7.1430	8.5926
H SAF (H11)	7.2567	7.9880	2.8742	3.5121

For all other PM algorithms, the SCE grows increasingly over time. This is true until the peak in SCE is reached approximately at the end of January or beginning of February. SCE for daily masks then begins to decrease, resembling natural changes, whereas cumulative SCE continues to grow but at lower rate. Just as for total accuracies, MAE and RMSE are better for cumulative than for daily masks of the majority of PM algorithms. The argument for cumulative masks seems obvious: PM estimates are much closer to reference IMS SCE. Even though this argument also applies to September and October, it was found that for these months daily outperform cumulative ones regarding accuracy. In fact, GlobSnow offers the best monthly accuracy for September using daily masks, but has the visibly lowest SCE. The derived area of SCE might present realistic values, however, the actual spatial location of the extent itself is not necessarily correct as explained in Section 4.3. The following subsection explores how accurate the location of the estimated SCE is.

5.2.1 Spatial and Temporal Difference

In order to investigate the estimated spatial extent of snow, difference maps are computed with respect to IMS data for all algorithms and considering the time span from 2007/2008 to 2016/2017. The resulting difference maps at the end of all seasons are shown in Figs. 5.8 and 5.9. For better clarity, all difference maps for individual months are given in Appendix A.4. Those maps show the general trend of each pixel, since one pixel might have experienced both positive and negative values that would cancel each other out. Absolute difference values are presented in Tables 5.4 and 5.5, which in turn take both over- and underestimation into account.

As already for SCE, Grody and Basist again shows the best performance in terms of total absolute difference, this time followed by H SAF for both snow mask types. The smaller the absolute difference the better, indicating less differences to IMS maps. Based on a visible comparison of Figs. 5.8b and 5.8f with Figs. 5.9b and 5.9f, both approaches tend to underestimate SCE for daily masks, whereas for cumulative masks, Grody and Basist generally appears to overestimate and H SAF both over- and underestimates to similar degree.

Difference maps of daily masks show a clear tendency to underestimate snow presence, as already observed for SCE, and not just for certain regions but rather on a broad scale. Underestimation is particularly dominant for GlobSnow and Armstrong and Brodzik. All other algorithms have at least a few regions that are characterised by overestimation, such as the Iberian Peninsula for Chang et al. and Foster et al., or the Taklamakan Desert in Northwest China again for Chang et al. and Foster et al. and less pronounced for H SAF.

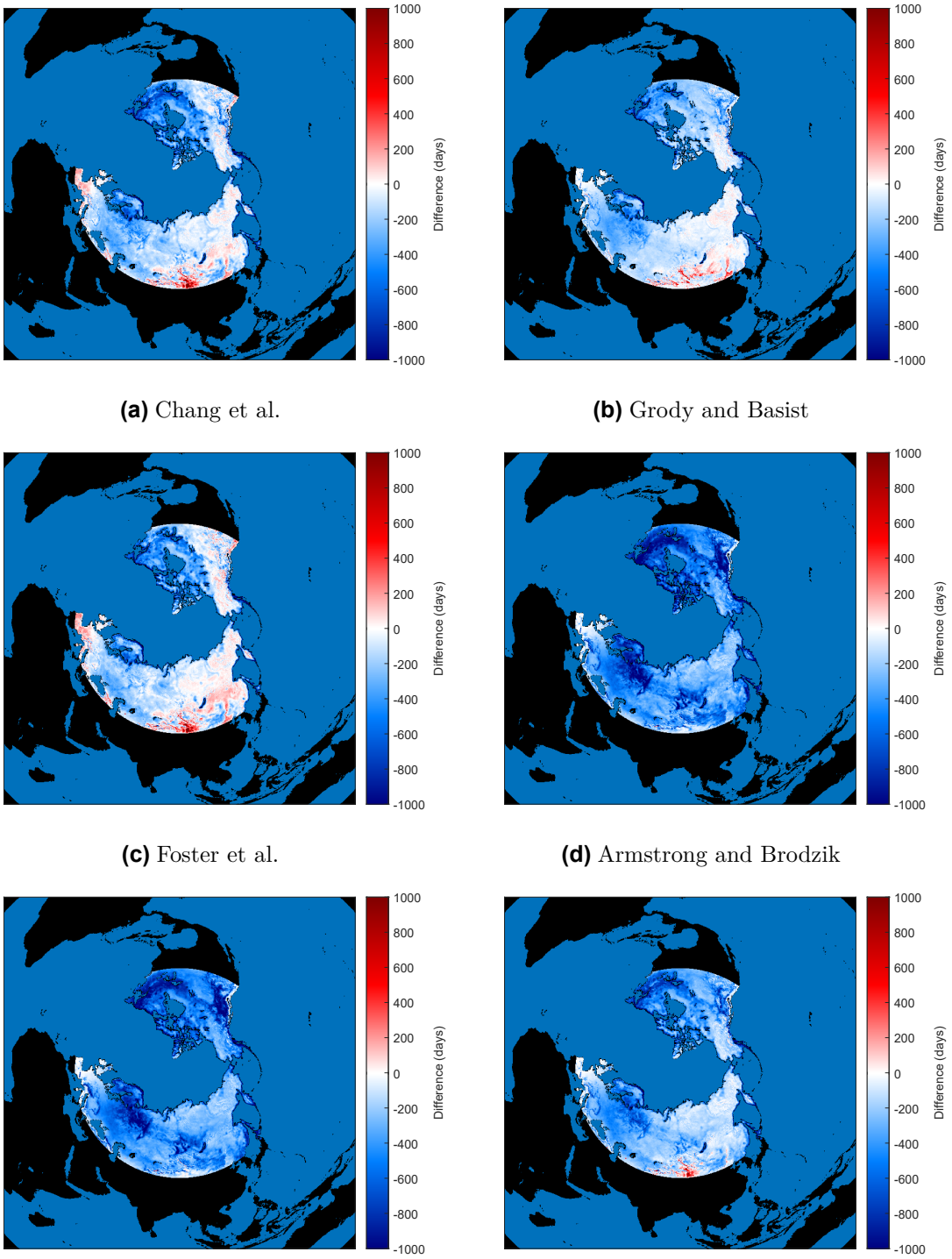

(a) Chang et al.

(b) Grody and Basist

(c) Foster et al.

(d) Armstrong and Brodzik

(e) GlobSnow

(f) H SAF (H11)

Figure 5.8. Difference maps for PM daily snow masks covering the winters from 2007/2008 to 2016/2017. The difference is expressed as the number of days that the PM algorithms underestimate (blue) or overestimate (red) snow presence with respect to IMS data. Within a single pixel, equal quantities of over- and underestimation annihilate each other.

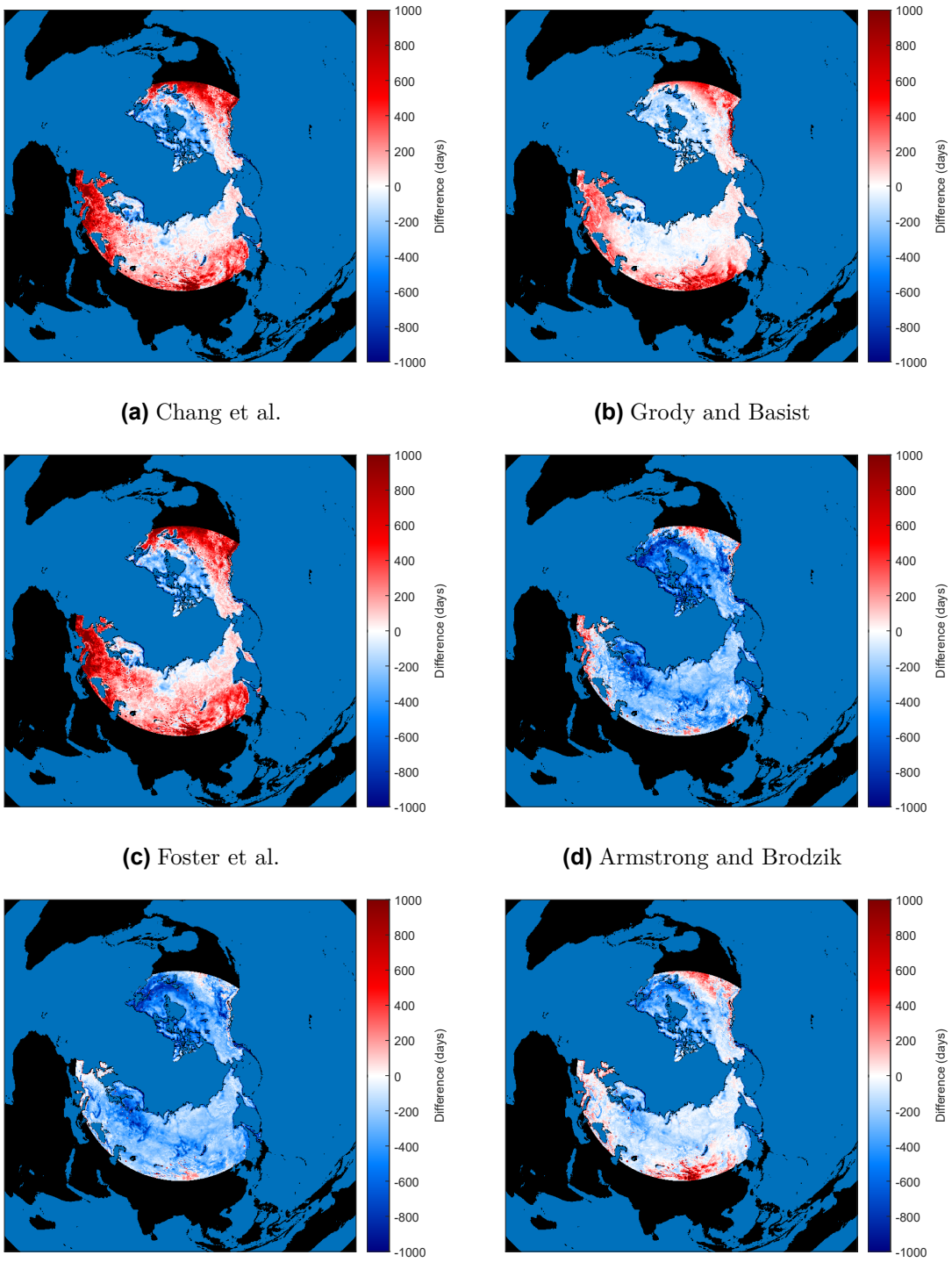

(a) Chang et al.

(b) Grody and Basist

(c) Foster et al.

(d) Armstrong and Brodzik

(e) GlobSnow

(f) H SAF (H11)

Figure 5.9. Difference maps for PM cumulative snow masks covering the winters from 2007/2008 to 2016/2017. The difference is expressed as the number of days that the PM algorithms underestimate (blue) or overestimate (red) snow presence with respect to IMS data. Within a single pixel, equal quantities of over- and underestimation annihilate each other.

Table 5.4. Absolute differences of individual months and the complete snow season (total) derived from the absolute pixelwise differences between PM daily snow masks and IMS data.

	Absolute difference (pixels)						
	Sep	**Oct**	**Nov**	**Dec**	**Jan**	**Feb**	**Total**
Chang et al.	2 905 667	5 180 226	6 014 319	4 998 049	3 446 455	2 712 027	25 256 743
Grody and Basist	**807 815**	**3 135 061**	**4 083 523**	**3 648 830**	**2 705 099**	**2 384 640**	**16 764 968**
Foster et al.	3 264 818	5 333 303	5 654 037	4 526 540	3 125 595	2 501 949	24 406 242
Armstrong and Brodzik	1 032 514	5 631 680	8 988 859	8 817 463	6 140 353	4 451 807	35 062 676
GlobSnow	987 873	5 557 761	8 558 356	8 349 882	5 703 538	4 292 032	33 449 442
H SAF (H11)	934 125	4 433 577	6 256 970	5 587 285	3 797 355	2 974 549	23 983 861

Table 5.5. Absolute differences of individual months and the complete snow season (total) derived from the absolute pixelwise differences between PM cumulative snow masks and IMS data.

	Absolute difference (pixels)						
	Sep	**Oct**	**Nov**	**Dec**	**Jan**	**Feb**	**Total**
Chang et al.	5 195 611	7 842 194	6 365 294	4 018 804	2 396 057	2 256 027	28 073 987
Grody and Basist	**843 731**	**3 002 082**	**3 366 569**	**2 530 812**	**1 870 880**	2 130 585	**13 744 659**
Foster et al.	5 875 488	8 319 058	6 177 597	3 757 046	2 289 277	2 233 909	28 652 375
Armstrong and Brodzik	1 555 162	6 079 877	8 364 290	7 056 462	4 087 096	2 768 364	29 911 251
GlobSnow	1 005 104	5 169 041	7 340 355	6 305 905	3 586 819	2 426 135	25 833 359
H SAF (H11)	1 043 440	4 189 178	5 135 540	3 866 461	2 331 890	**2 054 141**	18 620 650

The use of cumulative masks for difference maps results not only in the intended decrease of underestimation, but also in an increase of overestimation. The latter noticeably affects Chang et al. and Foster et al., which are the only ones whose total absolute difference does not improve for cumulative masks. Grody and Basist and H SAF are affected by overestimation as well though to a lesser extent and mainly for lower latitudes, see e.g. Fig. 5.10b, whilst for GlobSnow and Armstrong and Brodzik the underestimation of snow still dominates. Their total absolute difference improves for cumulative masks.

Furthermore, spatial variations are more noticeable (not necessarily larger) for cumulative masks, such as the underestimation of snow in mountainous regions. This is particularly visible for GlobSnow and H SAF in Europe as shown in Fig. 5.10a, where the Alps, Pyrenees, and Carpathian Mountains can be identified, for instance. Coastlines on the other hand experience a distinctive overestimation, again especially in Europe as (see Fig. 5.10a) but also along the West Coast of the United States. Significant overestimation is moreover observed for large lakes that are not masked out, including Vänern in southern Sweden (see Fig. 5.10a), Lake Nipigon as part of the Great Lake drainage basin in Ontario, Canada, or Sarygamysh Lake east of the Caspian Sea in Turkmenistan and Uzbekistan, to name a few examples. Those spatial variations highlight the importance of regional dry snow detection approaches, as suggested by Tedesco et al. [2].

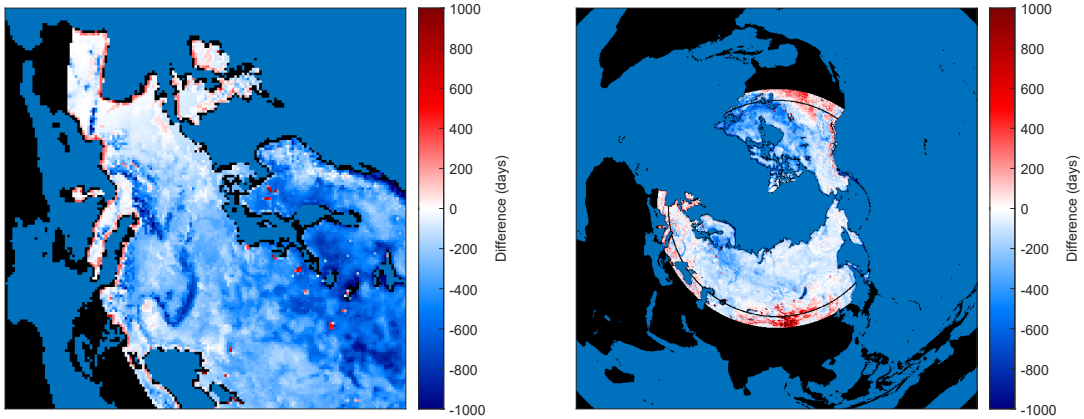

(a) GlobSnow **(b)** H SAF (H11)

Figure 5.10. Difference maps for PM cumulative snow masks, showing **(a)** detail of Europe for GlobSnow and **(b)** latitude of 45° North as black line for H SAF.

Similar trends are observed for monthly absolute differences as for monthly accuracies. The best absolute difference is found for September, apart from Chang et al. and Foster et al. who have their minimum in February. The absolute difference reaches its maximum or worst point in November, or October for Chang et al. and Foster et al. using cumulative snow masks. Again, October and November mark a changing point when the benefit of cumulative over daily masks becomes apparent. For Chang et al. and Foster et al. this point occurs later on in December, causing them to be overall better for daily snow masks.

It was pointed out in the previous SCE analysis that Chang et al. and Foster et al. deviate in the beginning of the snow season from the typical behaviour of IMS data and other PM approaches. The monthly difference maps demonstrate how both algorithms heavily overestimate SCE for most of the Northern Hemisphere in September and October, in particular for cumulative masks but also for daily ones. The overestimation reduces

significantly from November onwards but remains strong in lower latitudes for cumulative masks. Lower latitudes are prone to overestimation also for Grody and Basist and H SAF with cumulative masks, mainly during January and February. This cumulative effect is also visible in Fig. 5.7 as an overestimation in SCE towards the end of the snow season. Both Figs. 5.6 and 5.7 in addition show how GlobSnow and Armstrong and Brodzik continuously underestimate SCE. The monthly difference maps confirm this, showing that the onset of snow is visibly missed, let it be because of the insensitivity to shallow snow [1] or to fresh powder snow [9] or both. The regions for which they underestimate snow move further south with advancing SCE over the course of the winter.

In general, the difference maps and absolute difference values show that cumulative masks improve the performance of most PM approaches by enabling higher, more realistic SCE. However, cumulative masks are not optimal for any PM approach or for the whole snow season, since they may facilitate (significant) overestimation in snow presence.

5.3 Discussion

The preceding analysis of PM algorithms for dry snow detection addresses two major issues: their accuracy with respect to weather station SD data and their ability to estimate SCE in comparison to a blended product. Although the former provides a direct reference to ground-truth data, neither measure is superior but rather complements the other.

Pointwise weather station data are distorted by assuming each represents a whole grid cell. Since the microwave response of very thin snowpacks is negligible at 37 GHz, cells of low SD are furthermore expected in first place to be falsely labelled as snow-free, at least for all algorithms relying exclusively on the 18/19 and 37 GHz channels. The gain of information of low SD measurements is thus questionable, knowing that PM approaches tend to underestimate snow. Kelly et al. [31] therefore only take in situ measurements into account with SD greater than 30 mm, for instance. As this project investigates cumulative snow masks and implements additional frequencies, SD data are not filtered having already a very limited amount of weather station data. To further expand this available amount, it could be considered to create artificial 'ground-truth pixels' by setting cells as snow pixels that not only correspond but are also adjacent to (large) SD measurements. Regardless, this would not provide as extensive information as the blended SCE product. Despite not being ground truth, this product is considered to be reliable and serves as reference.

According to the quantitative measures, no single algorithm performs best throughout the whole time series or across the whole Northern Hemisphere. Table 5.6 aims to summarise the performance of the algorithms in a qualitative manner. Because cumulative snow masks are found to generally enhance PM dry snow detection, counteracting their tendency to underestimate snow presence, and because SSM/I and SSMIS data cover a significant longer time span, the categories 'accuracy' and 'difference' in Table 5.6 are presented under the consideration of those two aspects.

All in all, the approach of Grody and Basist [25] outperforms the other algorithms in terms of accuracy and SCE as shown in Table 5.6. It is the only approach considering and eliminating scattering effects other than due to snow, namely precipitation, cold deserts and frozen ground. This is highly advantageous when looking at the Northern Hemisphere as a whole since great variations in land cover have to be considered. The benefit of using multiple bands and refined criteria in order to discriminate between scattering mechanisms is its biggest disadvantage at the same time—the approach of Grody and Basist is not directly applicable to SMMR data. SMMR lacks centre frequencies of about 85/91 GHz, which are available only for SSM/I and SSMIS, respectively.

Table 5.6. Qualitative rating of PM dry snow detection approaches. Considered aspects are applicable instruments with regard to available channels, as well as accuracy and (absolute) differences for PM cumulative snow masks of SSM/I and SSMIS data. The rating scale indicates very poor (no dots) up to very good (three dots) performance; Difference type can be overestimation (+) and/or underestimation (−).

	Instrument		**Accuracy**			**Difference**	
	SMMR	SSM/I, SSMIS	total	Sep - Oct	Nov - Feb	total absolute	type
Chang et al.	yes	yes			●		+
Grody and Basist	no	yes	● ● ●	● ● ●	● ● ●	● ● ●	+/−
Foster et al.	yes	yes			●		+
Armstrong and Brodzik	(no)	yes	●	●	●		−
GlobSnow	yes	yes	●	● ● ●	●	●	−
H SAF (H11)	yes	yes	● ●	● ●	● ●	● ●	+/−

The algorithms of Chang et al. [13], Foster et al. [14] and Armstrong and Brodzik [37] are similar to the others in their performance for daily snow masks, but are not comparable anymore when using cumulative masks. Even though Foster et al. and Armstrong and Brodzik are both designed as improved versions of Chang et al., they present just minor advantages over the latter. Foster et al. take into account forest cover fraction and spatial variations of snow properties for Eurasia versus North America. Those changes seem to only slightly improve snow detection later on during the snow season. Armstrong and Brodzik on the other hand introduce a T_B adjustment to take into consideration the difference in central frequency for SSM/I against SMMR. Snow detection is now significantly improved at the beginning of the snow season, but remains of comparable levels otherwise. The algorithm of Armstrong and Brodzik could in theory be applied to SMMR data as is, but considering its purpose of customising Chang et al. for SSM/I data, this was not investigated. Interestingly, Chang et al. and Foster et al. present very similar spatial snow detection behaviour and have a strong tendency to overestimate SCE for cumulative masks, whereas Armstrong and Brodzik is generally susceptible to underestimate SCE.

GlobSnow [7], using the algorithm of Hall et al. [15], and H SAF [48] follow the same algorithm structure but with different thresholds for effective SD and brightness temperatures T_B^{37H} and T_B^{37V}. GlobSnow is more conservative regarding the labelling of snow pixels as pointed out by a comparatively low TP rate together with a relatively high TN rate. This leads to its very high accuracy during September and October when bare ground pixels overall dominate. Its difference pattern, predominantly underestimation, is spatially very similar to Armstrong and Brodzik. The different thresholds of H SAF in turn maintain a high confidence in detecting snow-free pixels at the beginning of the snow season, whilst improving snow detection when snow cover extent grows. This causes less under- but more

overestimation than for GlobSnow. H SAF presents similar overestimation characteristics as Grody and Basist—particularly for lower latitudes and towards the end of the snow season. After Grody and Basist, H SAF also performs overall well.

By including data of 85/91 GHz, it is shown that indeed the sensitivity to thin snow packs can be improved [1], [9]. H SAF, as example for an algorithm using 18/19-GHz and 37-GHz data only, identifies for cumulative masks more than 50% of all snow pixels correctly, but more than 80% of pixels corresponding to snow depths larger than 11 cm. Grody and Basist on the other hand include supplementary 85/91-GHz data. For cumulative masks, this approach achieves to classify more than 60% of all snow pixels correctly, and more than 80% for snow depths larger than only 5 cm. A tendency to overestimate the total snow extent as indicated by Rees [1] and Armstrong and Brodzik [32] is not observed to be more significant than for other algorithms that only implement 18/19 GHz and 37 GHz. As mentioned earlier, H SAF presents similar overestimation characteristics as Grody and Basist, and most often H SAF has higher values in absolute difference.

Common data processing steps for global snow estimations include masking of large water bodies and complex terrain [12]. Considering the poor snow detection ability observed for large lakes that have not been masked out, more thorough water masking could be considered, yet the resulting improvements would be relatively small. The masking of complex regions on the other hand would enhance especially the approaches of GlobSnow and H SAF significantly, which severely underestimate snow for mountain ranges. In fact, the GlobSnow SWE product masks out cells with large elevation changes [7], so a better performance of all algorithms in this context would be expected regardless. A further common procedure for snow detection involves the use of a snow climatology [12], e.g. [65]. By providing likelihoods for snow within each cell, regional differences regarding how sensitive an individual algorithm is to snow, would be directly addressed. This would possibly reduce the need of masking (mountain) cells. GlobSnow SWE retrieval applies JASMES [45] instead to detect the onset of snow melt, amongst others. Overall, JASMES achieves noticeably better results in terms of accuracy than any PM approach, especially during January and February, and can be considered a sensible choice. Especially the cumulative approaches of H SAF and Grody and Basist would benefit of a separate detection of snow melt, where affected pixels are set as 'snow-free'. Their issue with overestimating snow presence for lower latitudes in January and February could be expected to get resolved to most extent. In general, some form of snowmelt detection is required to apply cumulative masks also to months that are dominated by melt later on in the snow season.

When applying dry snow detection over a long time span, as is the case for the GlobSnow SWE product, one single algorithm should be preferably used. The use of different PM approaches either for different instrument periods or for different parts of one snow season would inevitably lead to discontinuous, non-realistic jumps in SCE—both on regional and hemispheric scale. The practicality of splitting algorithm approaches or switching between daily and cumulative masks within the time series is thus not desirable. The qualitative overview in Table 5.6 highlights Grody and Basist as best-performing from all investigated PM dry snow detection algorithms. Considering the 40-year time span that is investigated in this thesis and in the GlobSnow SWE product, however, it is a major constraint that it cannot be applied in its form to SMMR data. In this regard, the approach of H SAF is favourable, at least as immediate improvement, as it could be applied to GlobSnow SWE retrieval as is and would still be expected to improve SWE estimates. With further research required, the optimal aim would be to develop a SMMR-friendly version of Grody and Basist by omitting the 85/91-GHz channels (and possibly incorporating the 10-GHz channel) whilst keeping the differentiation between different scattering media.

6 Conclusion

In this thesis, algorithms using spaceborne passive microwave radiometer data for the detection of dry snow on hemispheric scale are assessed. Relevant dry snow detection approaches are evaluated, namely the approaches of Chang et al. [13], Grody and Basist [25], Foster et al. [14], Armstrong and Brodzik [37], Hall et al. [15] which is used in the GlobSnow v3.0 SWE product [7], and of the EUMETSAT H SAF (H11) product [48]. Those six algorithms exploit the fact that microwave emission of snow is frequency-dependent and are implemented using SMMR, SSM/I and SSMIS data in form of brightness temperatures. Their capabilities are subsequently compared over a time span of 40 years, from 1979 until 2018. The long-term comparison focuses on terrestrial seasonal snow cover in the Northern Hemisphere for latitudes above 40° North, and the algorithms' intraseasonal performance is of particular interest for the snow accumulation period during September to February. For the analysis, two types of binary (snow/snow-free) masks are computed: daily and cumulative snow masks. The former gives the SCE in conventional form, on a daily basis using the radiometer data that is available for a given day. The latter follows the example of [7] and is based on daily snow masks, but each cell that is classified as snow remains a snow pixel for the rest of the season disregarding possible snowmelt or data gaps.

The evaluation for the snow seasons from 1979/1980 to 2017/2018 is carried out by means of extensive pointwise snow depth observations from weather stations across the whole Northern Hemisphere. Daily, monthly and total means of accuracy are computed, indicating the agreement (fraction) of both snow and snow-free PM classifications of each algorithm with synoptic ground-truth data. Additionally, true positive and true negative rates, given as daily means over a snow season, present the shares of correct snow and snow-free PM observations, respectively, and are used to investigate the algorithms' sensitivity to snow depth. Besides ground-truth data, spatially-complete snow cover extent maps by the Interactive Multisensor Snow and Ice Mapping System [17] serve as reference for 10 snow seasons, from 2007/2008 to 2016/2017. This allows for an assessment of the snow-covered area detected by the PM algorithms relative to IMS estimates of SCE, using daily means of SCE for PM and blended data, and their mean absolute errors and root-mean-square errors with respect to each other. Moreover, the computation of difference maps by subtracting PM snow masks from IMS maps enables the visualisation of spatial and temporal differences in SCE. Although the computed accuracy is absolute with respect to ground truth and the comparison in SCE is only relative, both are important indicative measures that complement each other to convey a comprehensive picture of the algorithms' performance.

The investigated PM dry snow detection algorithms are primarily based on the brightness temperature difference of the horizontal 18/19-GHz and 37-GHz channels. Even though the algorithms of Foster et al. and Armstrong and Brodzik are both designed as enhanced versions of Chang et al., they present merely minor improvements. The approach of Foster et al. takes into account forest cover fraction and to some extent spatial variations of snow properties for Eurasia against North America, slightly improving snow detection later on during the snow season. Armstrong and Brodzik introduce an adjustment in brightness temperature taking into consideration differences in central frequency between SSM/I and SMMR, which improves snow detection more considerably but still limited to the beginning of the snow season. The algorithm of H SAF in turn, an adaptation of GlobSnow's

dry snow detection, shows more noticeable improvements concerning the underestimation of snow cover and performs overall well with a total accuracy of about 0.80 for cumulative masks. Horizontal polarisation-based algorithms, as the ones just mentioned, have previously been found to be particularly suitable for dry snow detection by yielding the best overall hemispheric to global-scale estimates [31], [35]. Vertical polarisation channels are commonly accepted to be more appropriate for snow depth estimations [31]. However, in this comparison the algorithm of Grody and Basist stands out with a total accuracy of 0.81 and 0.83 for daily and cumulative masks, respectively. This approach is based on the vertical 18/19-GHz and 37-GHz channels, amongst other, and moreover specifically considers and eliminates erroneous scattering effects caused by precipitation, cold deserts and frozen ground. This appears to be highly advantageous when considering the whole Northern Hemisphere with its great variety in land cover, and leads to the best snow detection performance.

While it is confirmed that PM dry snow detection approaches tend to underestimate snow extent [1], cumulative snow masks are found to be promising at counteracting this issue and outperform daily ones for most algorithms. The reduction in underestimation due to cumulative masks leads to smaller deviations from IMS maps, whose SCE progression is best followed by the cumulative approach of Grody and Basist (applicable to SSM/I and SSMIS), achieving a MAE in SCE as low as $2.5 \times 10^6\,\mathrm{km}^2$. H SAF (applicable to SMMR, SSM/I and SSMIS), also for cumulative masks, follows closely with a MAE of $2.9 \times 10^6\,\mathrm{km}^2$. Both approaches, H SAF and Grody and Basist, present overall high accuracies and comparatively low (absolute) differences. In comparison, the best results for daily masks are $4.0 \times 10^6\,\mathrm{km}^2$ again for Grody and Basist. The strength of the two cumulative methods lies in the steep increase in TP rate in comparison to other algorithms, i.e. their capability to detect snow observations correctly improves significantly over time—and this ability becomes increasingly important with advancing snow accumulation season. An improvement in snow detection over the course of a season is generally observed for all algorithms and both mask types, and is most likely a consequence of the PM methods' sensitivity to snow depth: shallow snowpacks in autumn are less accurately detected than deeper ones in mid-winter [13], [15].

Under the consideration of improving dry snow detection within the GlobSnow SWE product, the analysis shows that both the approaches of H SAF and Grody and Basist are strong candidates. Their cumulative versions tackle underestimation effectively, and regional overestimation is limited mainly to lower latitudes towards the end of the season in January and February. This can be explained by the fact that cumulative SCE continues to grow and does not resemble the natural stagnation and decrease in SCE from January onwards. In the case of GlobSnow, separate means are implemented to detect snow melt [7] and overestimation is thus not seen to be a major issue. Even though Grody and Basist convince with a higher performance due to their sophisticated discrimination between scattering materials, this is at the same time the biggest disadvantage. As it uses additional channels that are not available for SMMR, the algorithm cannot be applied directly to SMMR data which essentially cuts off 10 years of the long term climate record. The H SAF algorithm in its current form, on the other hand, can be simply implemented as is, considering it has the same structure as GlobSnow but applies different thresholds. In the short term, H SAF is a reasonable choice to be implemented in the GlobSnow SWE product. However, future work involves the development of a version of Grody and Basist that would be applicable to SMMR data as well, in order to ensure a long-term, accurate dry snow detection approach.

References

[1] W. Rees, *Remote Sensing of Snow and Ice*. CRC Press, 2005.

[2] M. Tedesco, *Remote Sensing of the Cryosphere*. John Wiley & Sons, Ltd, 2014.

[3] A. Dietz, C. Kuenzer, U. Gessner, and S. Dech, "Remote sensing of snow – a review of available methods," *International Journal of Remote Sensing*, vol. 33, pp. 4094–4134, 2012.

[4] J. Pulliainen, K. Luojus, C. Derksen, *et al.*, "Patterns and trends of Northern Hemisphere snow mass from 1980 to 2018," *Nature*, vol. 581, pp. 294–298, 2020.

[5] *Global Climate Observing System: Essential Climate Variable Factsheet - Snow*, https://gcos.wmo.int/en/essential-climate-variables/snow, Accessed: 2021-12-28.

[6] *ESA Climate Change Initiative - Snow*, https://climate.esa.int/en/projects/snow/, Accessed: 2021-12-28.

[7] K. Luojus, J. Pulliainen, M. Takala, *et al.*, "GlobSnow v3.0 Northern Hemisphere snow water equivalent dataset," *Scientific Data*, vol. 8, no. 163, 2021.

[8] W. Schreiber-Abshire, P. Dills, M. Weingroff, D. Ward, R. Ferraro, and F. Weng, *Land and Ocean Surface Applications (2nd Edition)*, Microwave Remote Sensing, COMET Program of the University Corporation for Atmospheric Research (UCAR), 2015.

[9] C. Mätzler, "Passive microwave signatures of landscapes in winter," *Meteorology and Atmospheric Physics*, vol. 54, pp. 241–260, 1994.

[10] F. Ulaby and D. Long, *Microwave Radar and Radiometric Remote Sensing*. The University of Michigan Press, 2014.

[11] I. Woodhouse, *Introduction to Microwave Remote Sensing*. Taylor & Francis Group, 2006.

[12] N. Saberi, R. Kelly, M. Flemming, and Q. Li, "Review of snow water equivalent retrieval methods using spaceborne passive microwave radiometry," *International Journal of Remote Sensing*, vol. 41, no. 3, pp. 996–1018, 2020.

[13] A. Chang, J. Foster, and D. Hall, "Nimbus-7 SMMR derived global snow cover parameters," *Annals of Glaciology*, vol. 9, pp. 39–44, 1987.

[14] J. Foster, A. Chang, and D. Hall, "Comparison of snow mass estimates from a prototype passive microwave snow algorithm, a revised algorithm and a snow depth climatology," *Remote Sensing of Environment*, vol. 62, no. 2, pp. 132–142, 1997.

[15] D. Hall, R. Kelly, G. Riggs, A. Chang, and J. Foster, "Assessment of the relative accuracy of hemispheric-scale snow-cover maps," *Annals of Glaciology*, vol. 34, pp. 24–30, 2002.

[16] P. Prestrud, J. Calder, P. Cochran, *et al.*, "Global Outlook for Ice and Snow," United Nations Environment Programme, Tech. Rep., 2007.

[17] S. Helfrich, M. Li, C. Kongoli, L. Nagdimunov, and E. Rodriguez, "Algorithm Theoretical Basis Document (ATBD) for Interactive Multisensor Snow and Ice Mapping System Version 3 (IMS V3)," NOAA NESDIS Center for Satellite Applications and Research, Tech. Rep. 2.5, 2018.

[18] L. Tsang, K. Ding, and B. Wen, "Dense media radiative transfer theory for dense discrete random media with particles of multiple sizes and permittivities," *Progress in Electromagnetic Research*, vol. 6, no. 5, pp. 181–225, 1992.

[19] L. Tsang, C.-T. Chen, A. Chang, J. Guo, and K.-H. Ding, "Dense media radiative transfer theory based on quasicrystalline approximation with applications to passive microwave remote sensing of snow," *Radio Science*, vol. 35, no. 3, pp. 731–749, 2000.

[20] B. Wen, L. Tsang, D. Winebrenner, and A. Ishimaru, "Dense medium radiative transfer theory: Comparison with experiment and application to microwave remote sensing and polarimetry," *IEEE Transactions on Geoscience and Remote Sensing*, vol. 28, no. 1, pp. 46–59, 1990.

[21] J. Pulliainen, J. Grandell, and M. Hallikainen, "HUT snow emission model and its applicability to snow water equivalent retrieval," *IEEE Transactions on Geoscience and Remote Sensing*, vol. 37, no. 3, pp. 1378–1390, 1999.

[22] A. Kumar, "Seasonal Snow Cover," in *Encyclopedia of Snow, Ice and Glaciers*, V. Singh, P. Singh, and U. Haritashya, Eds. Springer Netherlands, 2011, pp. 974–975.

[23] T. C. Grenfell, "Albedo," in *Encyclopedia of Snow, Ice and Glaciers*, V. Singh, P. Singh, and U. Haritashya, Eds. Springer Netherlands, 2011, pp. 23–35.

[24] P. Dills, T. Lee, A. Kuciauskas, and F. Weng, *Microwave Remote Sensing Resources*, Microwave Remote Sensing, COMET Program of the University Corporation for Atmospheric Research (UCAR), 2019.

[25] N. Grody and A. Basist, "Global identification of snowcover using SSM/I measurements," *IEEE Transactions on Geoscience and Remote Sensing*, vol. 34, no. 1, pp. 237–249, 1996.

[26] J. Foster, D. Hall, A. Chang, A. Rango, W. Wergin, and E. Erbe, "Effects of Snow Crystal Shape on the Scattering of Passive Microwave Radiation," *IEEE Transactions on Geoscience and Remote Sensing*, vol. 37, no. 2, pp. 1165–1168, 1999.

[27] E. Josberger and N. Mognard, "A passive microwave snow depth algorithm with a proxy for snow metamorphism," *Hydrological Processes*, vol. 16, no. 8, pp. 1557–1568, 2002.

[28] J. Foster, C. Sun, J. Walker, *et al.*, "Quantifying the uncertainty in passive microwave snow water equivalent observations," *Remote Sensing of Environment*, vol. 94, no. 2, pp. 187–203, 2005.

[29] M. Bhutiyani, "Inverted Cup Depth Hoar Crystals," in *Encyclopedia of Snow, Ice and Glaciers*, V. Singh, P. Singh, and U. Haritashya, Eds. Springer Netherlands, 2011, pp. 656–657.

[30] P. Nienow and F. Campbell, "Stratigraphy of Snowpacks," in *Encyclopedia of Snow, Ice and Glaciers*, V. Singh, P. Singh, and U. Haritashya, Eds. Springer Netherlands, 2011, pp. 1081–1084.

[31] R. Kelly, A. Chang, L. Tsang, and J. Foster, "A prototype AMSR-E global snow area and snow depth algorithm," *IEEE Transactions on Geoscience and Remote Sensing*, vol. 41, no. 2, pp. 230–242, 2003.

[32] A. Richard and M. Brodzik, "Hemispheric-scale comparison and evaluation of passive-microwave snow algorithms," *Annals of Glaciology*, vol. 34, pp. 38–44, 2002.

[33] A. Saraf, "Passive microwave data for snow-depth and snow-extent estimations in the Himalayan mountains," *International Journal of Remote Sensing*, vol. 20, no. 1, pp. 83–95, 1999.

[34] C. Derksen, A. Walker, and B. Goodison, "A comparison of 18 winter seasons of in situ and passive microwave-derived snow water equivalent estimates in Western Canada," *Remote Sensing of Environment*, vol. 88, no. 3, pp. 271–282, 2003.

[35] R. Armstrong and M. Brodzik, "Twenty-four year record of Northern Hemisphere snow cover derived from passive microwave remote sensing," in *Microwave Remote Sensing of the Atmosphere and Environment III*, International Society for Optics and Photonics, vol. 4894, 2003, pp. 373–380.

[36] R. Kelly, "The AMSR-E Snow Depth Algorithm: Description and Initial Results," *Journal of The Remote Sensing Society of Japan*, vol. 29, no. 1, pp. 307–317, 2009.

[37] R. Armstrong and M. Brodzik, "Recent Northern Hemisphere snow extent: A comparison of data derived from visible and microwave satellite sensors," *Geophysical Research Letters*, vol. 28, no. 19, pp. 3673–3676, 2001.

[38] B. Goodison, "Determination of Areal Snow Water Equivalent on the Canadian Prairies using Passive Microwave Satellite Data," in *12th Canadian Symposium on Remote Sensing Geoscience and Remote Sensing Symposium*, vol. 3, 1989, pp. 1243–1246.

[39] T. Che, X. Li, R. Jin, R. Armstrong, and T. Zhang, "Snow depth derived from passive microwave remote-sensing data in china," *Annals of Glaciology*, vol. 49, pp. 145–154, 2008.

[40] A. Tait, "Estimation of snow water equivalent using passive microwave radiation data," *Remote Sensing of Environment*, vol. 64, no. 3, pp. 286–291, 1998.

[41] M. Tedesco and J. Jeyaratnam, "A New Operational Snow Retrieval Algorithm Applied to Historical AMSR-E Brightness Temperatures," *Remote Sensing*, vol. 8, no. 12, 2016.

[42] M. Tedesco, J. Pulliainen, M. Takala, M. Hallikainen, and P. Pampaloni, "Artificial neural network-based techniques for the retrieval of SWE and snow depth from SSM/I data," *Remote Sensing of Environment*, vol. 90, no. 1, pp. 76–85, 2004.

[43] M. Tedesco, R. Kelly, J. Foster, and A. Chang, *AMSR-E/Aqua Daily L3 Global Snow Water Equivalent EASE-Grids*, Version 2, Northern and Southern Hemisphere (1978-1987), NASA National Snow and Ice Data Center Distributed Active Archive Center, 2004.

[44] D. Hall, G. Riggs, and V. Salomonson, "Algorithm Theoretical Basis Document (ATBD) for the MODIS Snow and Sea Ice-Mapping Algorithms," NASA, Tech. Rep., 2001.

[45] M. Hori, K. Sugiura, K. Kobayashi, *et al.*, "A 38-year (1978–2015) Northern Hemisphere daily snow cover extent product derived using consistent objective criteria from satellite-borne optical sensors," *Remote Sensing of Environment*, vol. 191, pp. 402–418, 2017.

[46] A. Frei, M. Tedesco, S. Lee, *et al.*, "A review of global satellite-derived snow products," *Advances in Space Research*, vol. 50, pp. 1007–1029, Oct. 2012.

[47] J. Foster, D. Hall, J. Eylander, *et al.*, "A blended global snow product using visible, passive microwave and scatterometer satellite data," *International Journal of Remote Sensing*, vol. 32, pp. 1371–1395, 2011.

[48] J. Pulliainen, P. Lahtinen, J. Kärnä, and S. Koponen, "Algorithm Theoretical Definition Document (ATDD) for Product SN-OBS-2 - Snow Status (Dry/Wet) by Microwave Radiometry," EUMETSAT H-SAF, Tech. Rep. H11, 2010.

[49] J. Pulliainen, P. Lahtinen, N. Siljamo, A. Sorman, Z. Akyurek, and S. Surer, "Algorithm Theoretical Definition Document (ATDD) for Product SN-OBS-1 - Snow Detection (Snow Mask) by Visible/Infrared Radiometry," EUMETSAT H-SAF, Tech. Rep. H10 (Version 1.1), 2011.

[50] M. Brodzik and K. Knowles, "EASE-Grid: A Versatile Set of Equal-Area Projections and Grids," in *Discrete Global Grids: A Web Book*. National Center for Geographic Information & Analysis, 2002, ch. 5, pp. 98–113.

[51] M. Brodzik, B. Billingsley, T. Haran, B. Raup, and M. Savoie, "EASE-Grid 2.0: Incremental but Significant Improvements for Earth-Gridded Data Sets," *ISPRS International Journal of Geo-Information*, vol. 1, no. 1, pp. 32–45, 2012.

[52] K. Knowles, E. Njoku, R. Armstrong, and M. Brodzik, *Nimbus-7 SMMR Pathfinder Daily EASE-Grid Brightness Temperatures*, Version 1, Northern Hemisphere (1978-

1987), NASA National Snow and Ice Data Center Distributed Active Archive Center, 2000.

[53] R. Armstrong, K. Knowles, M. Brodzik, and M. Hardman, *DMSP SSM/I-SSMIS Pathfinder Daily EASE-Grid Brightness Temperatures*, Version 2, Northern Hemisphere (1987-2018), NASA National Snow and Ice Data Center Distributed Active Archive Center, 1994.

[54] C. Fu, D. Han, S. Kim, and P. Gloersen, "User's Guide for the Nimbus 7 Scanning Multichannel Microwave Radiometer (SMMR)," NASA, Tech. Rep. 1210, 1988.

[55] J. Hollinger, J. Peirce, and G. Poe, "SSM/I Instrument Evaluation," *IEEE Transactions on Geoscience and Remote Sensing*, vol. 28, no. 5, pp. 781–790, 1990.

[56] D. Kunkee, G. Poe, D. Boucher, *et al.*, "Design and Evaluation of the First Special Sensor Microwave Imager/Sounder," *IEEE Transactions on Geoscience and Remote Sensing*, vol. 46, no. 4, pp. 863–883, 2008.

[57] O. Bulygina and V. Razuvaev, *Daily Temperature and Precipitation Data for 518 Russian Meteorological Stations*, Routine Snow Surveys (1979-2018), All-Russia Research Institute of Hydrometeorological Information - World Data Center, 2012.

[58] M. Menne, I. Durre, R. Vose, B. Gleason, and T. Houston, "An Overview of the Global Historical Climatology Network-Daily Database," *Journal of Atmospheric and Oceanic Technology*, vol. 29, no. 7, pp. 897–910, 2012.

[59] J. Dyer and T. Mote, "Spatial variability and patterns of snow depth over North America," *Geophysical Research Letters*, vol. 33, L16503, 2006.

[60] J. Pulliainen, "Mapping of snow water equivalent and snow depth in boreal and sub-arctic zones by assimilating space-borne microwave radiometer data and ground-based observations," *Remote Sensing of Environment*, vol. 101, no. 2, pp. 257–269, 2006.

[61] M. Takala, K. Luojus, J. Pulliainen, *et al.*, "Estimating Northern Hemisphere snow water equivalent for climate research through assimilation of space-borne radiometer data and ground-based measurements," *Remote Sensing of Environment*, vol. 115, no. 12, pp. 3517–3529, 2011.

[62] M. Takala, J. Pulliainen, S. Metsämäki, and J. Koskinen, "Detection of Snowmelt Using Spaceborne Microwave Radiometer Data in Eurasia From 1979 to 2007," *IEEE Transactions on Geoscience and Remote Sensing*, vol. 47, no. 9, pp. 2996–3007, 2009.

[63] P. Defourny, C. Lamarche, S. Bontemps, *et al.*, "Land Cover CCI - Product User Guide," ESA, Tech. Rep. 2.0, 2017.

[64] S. Bontemps, P. Defourny, E. Van Bogaert, O. Arino, V. Kalogirou, and J. Ramos Perez, "GlobCover 2009 - Products Description and Validation Report," ESA and UCLouvain, Tech. Rep. 2.2, 2011.

[65] K. Dewey and R. Heim, "Satellite Observations of Variations in Northern Hemisphere Seasonal Snow Cover," NOAA, Tech. Rep. NESS 87, 1981.

A Appendix

A.1 Daily Mean Accuracy

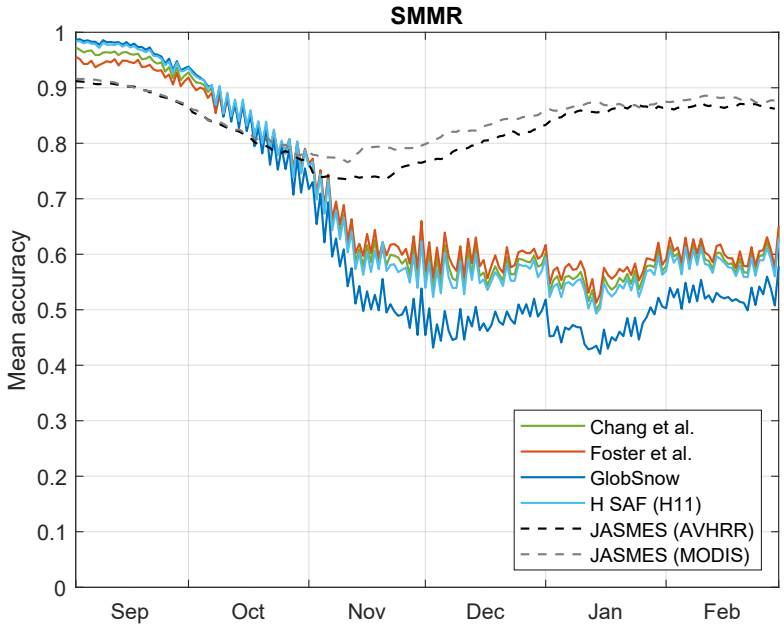

Figure A.1. Daily mean accuracy over the course of a snow season for PM daily snow masks of SMMR data and for optical JASMES masks of AVHRR and MODIS data with respect to synoptic weather station data.

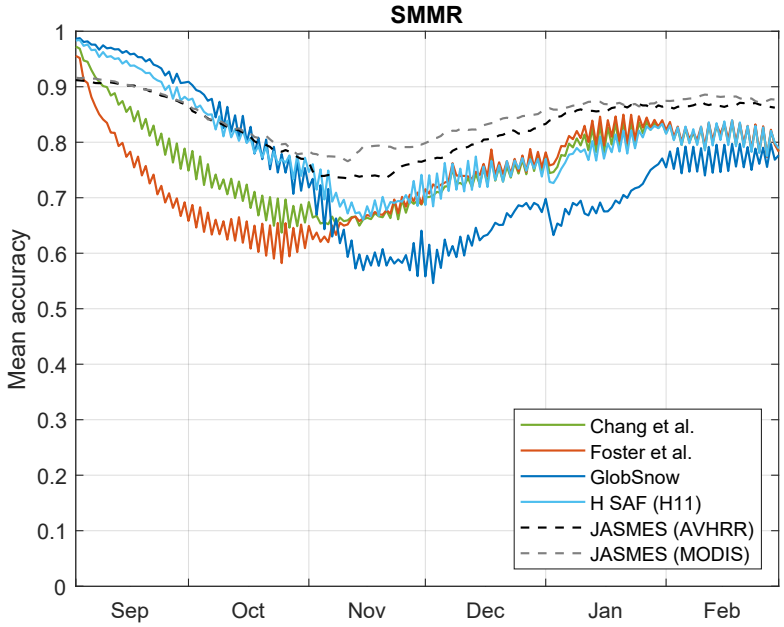

Figure A.2. Daily mean accuracy over the course of a snow season for PM cumulative snow masks of SMMR data and for optical JASMES masks of AVHRR and MODIS data with respect to synoptic weather station data.

A.2 TP and TN Rates

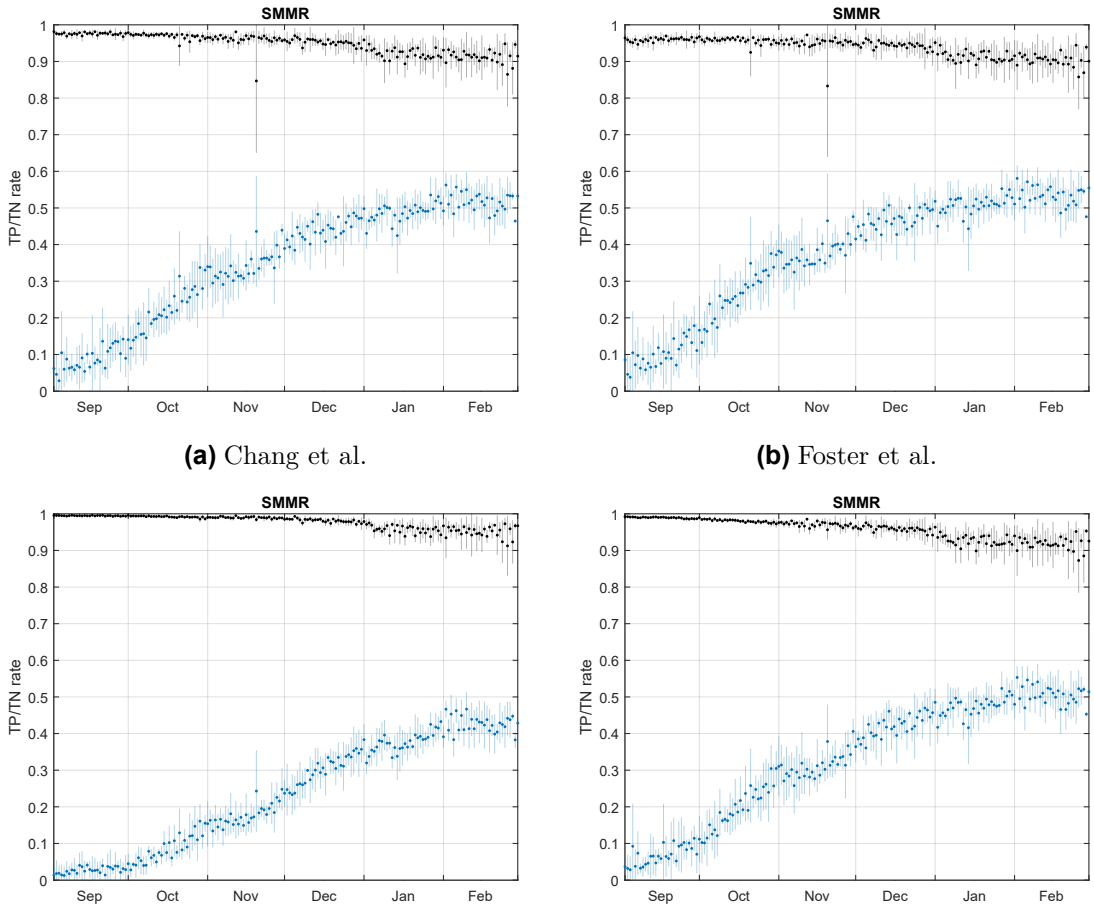

(a) Chang et al.

(b) Foster et al.

(c) GlobSnow

(d) H SAF (H11)

Figure A.3. Daily mean TP (blue) and TN (black) rate with error bars corresponding to one standard deviation over the course of a snow season for PM daily snow masks of SMMR data with respect to synoptic weather station data.

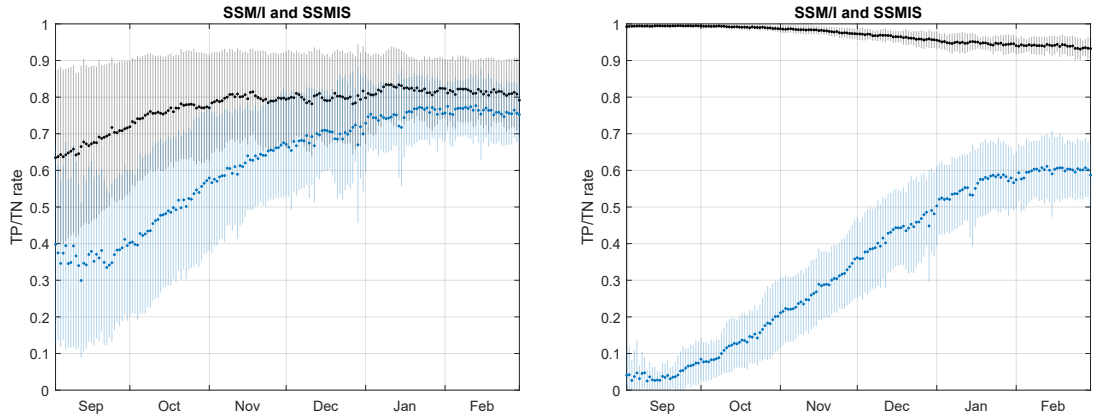

(a) Chang et al.

(b) Armstrong and Brodzik

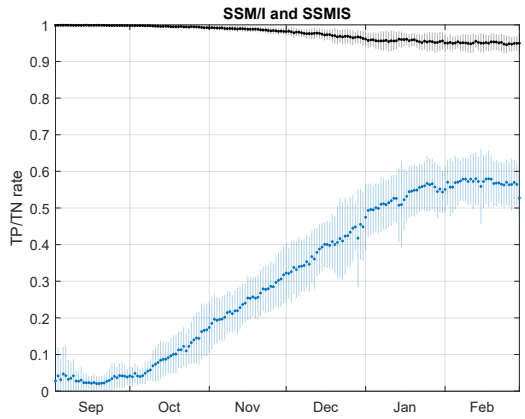

(c) GlobSnow

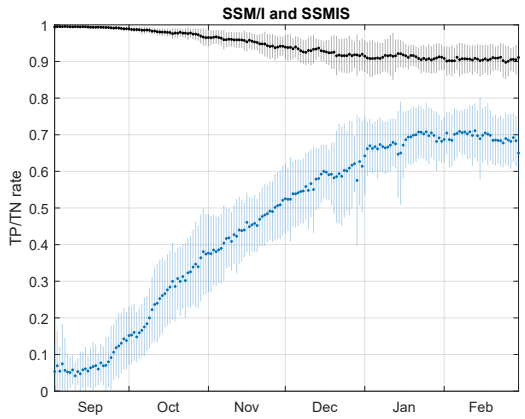

(d) H SAF (H11)

Figure A.4. Daily mean TP (blue) and TN (black) rate with error bars corresponding to one standard deviation over the course of a snow season for PM daily snow masks of SSM/I and SSMIS data with respect to synoptic weather station data (continued).

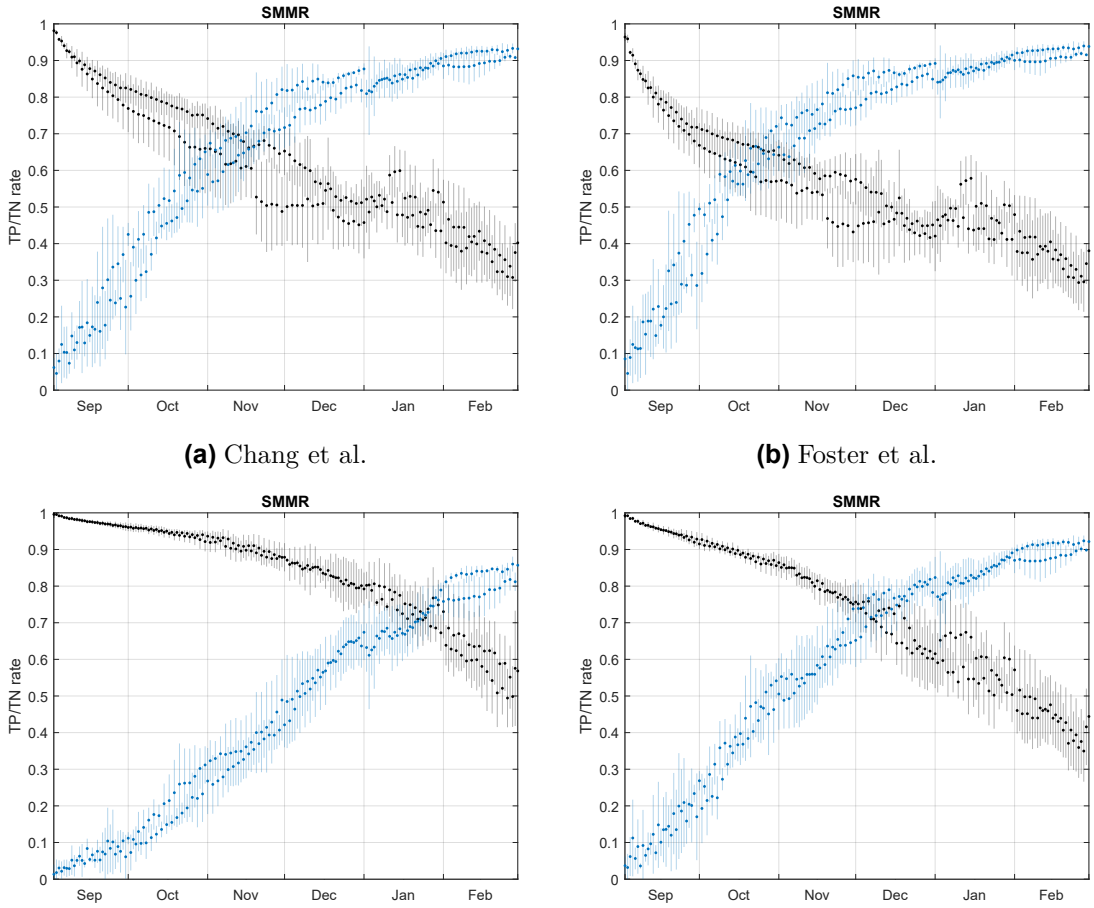

(a) Chang et al.

(b) Foster et al.

(c) GlobSnow

(d) H SAF (H11)

Figure A.5. Daily mean TP (blue) and TN (black) rate with error bars corresponding to one standard deviation over the course of a snow season for PM cumulative snow masks of SMMR data with respect to synoptic weather station data.

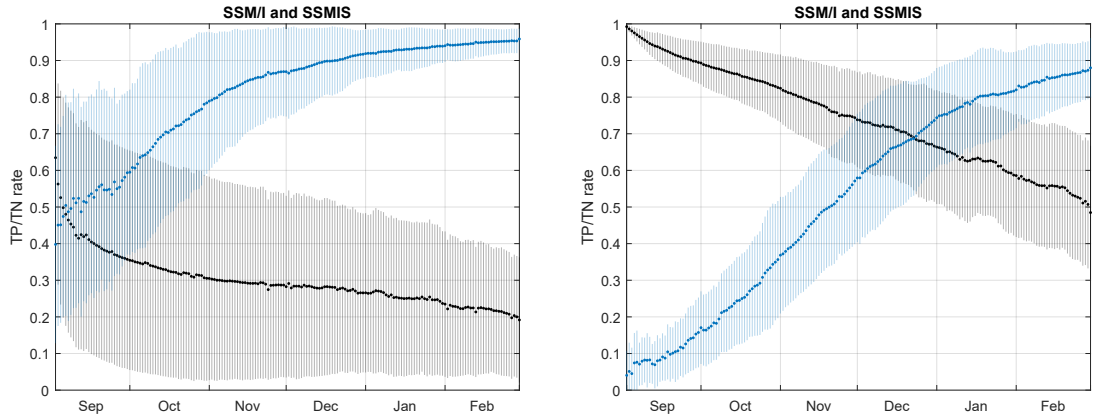

(a) Chang et al. **(b)** Armstrong and Brodzik

Figure A.6. Daily mean TP (blue) and TN (black) rate with error bars corresponding to one standard deviation over the course of a snow season for PM cumulative snow masks of SSM/I and SSMIS data with respect to synoptic weather station data (continued).

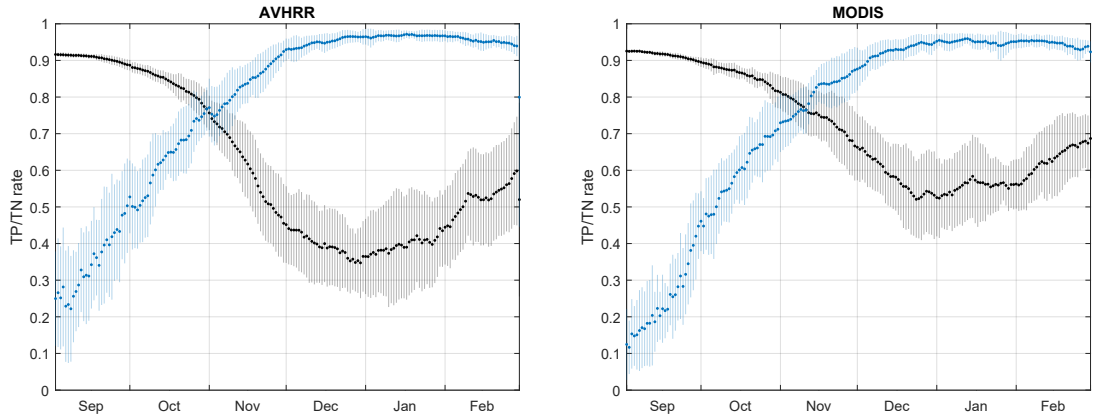

(a) **(b)**

Figure A.7. Daily mean TP (blue) and TN (black) rate with error bars corresponding to one standard deviation over the course of a snow season for daily optical JASMES masks of AVHRR and MODIS data with respect to synoptic weather station data.

A.3 Snow Depth Histograms

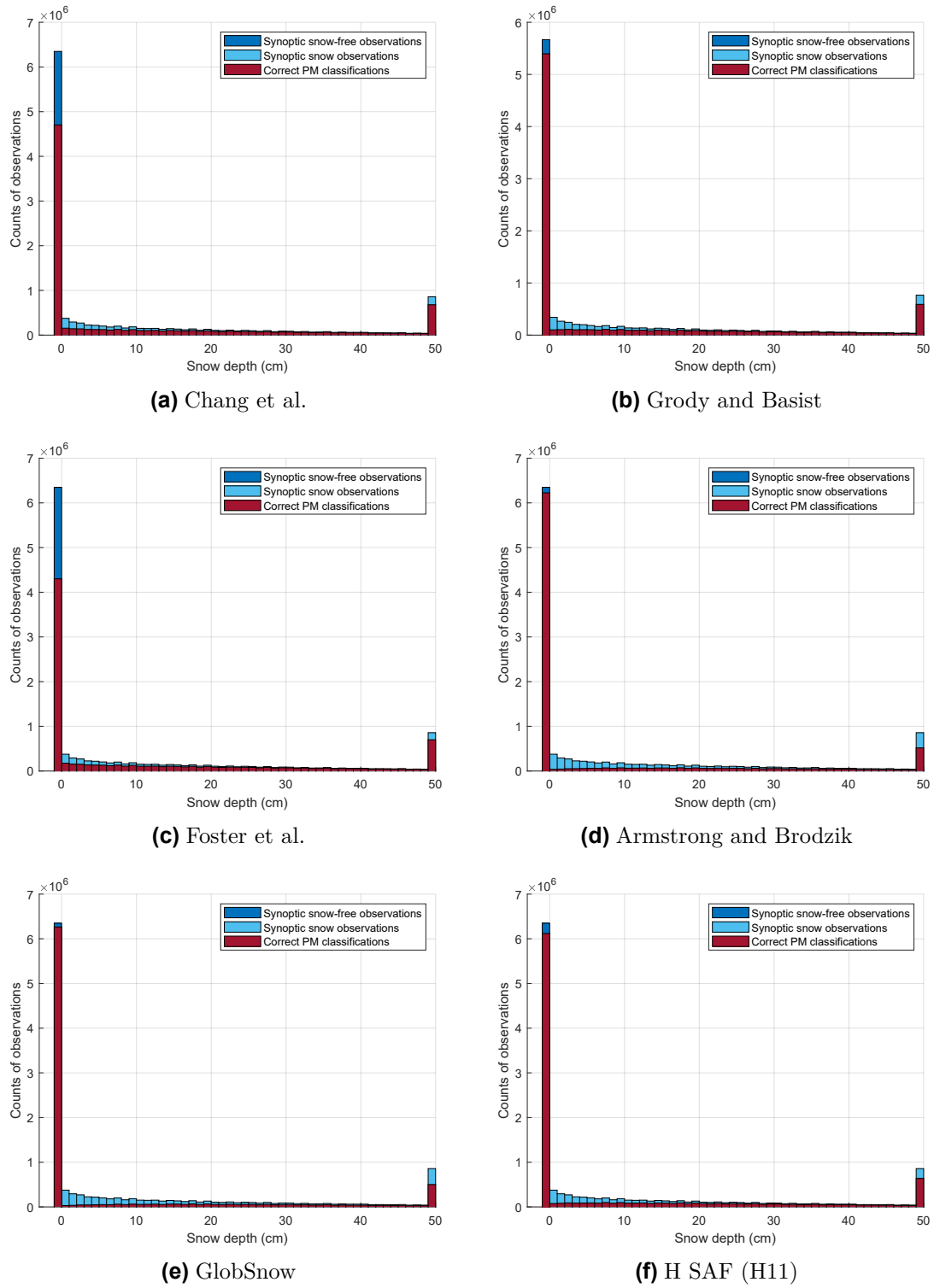

(a) Chang et al.

(b) Grody and Basist

(c) Foster et al.

(d) Armstrong and Brodzik

(e) GlobSnow

(f) H SAF (H11)

Figure A.8. Histograms of synoptic SD observations, and the share of correct snow/snow-free classifications for PM daily snow masks of SMMR, SSM/I and SSMIS data.

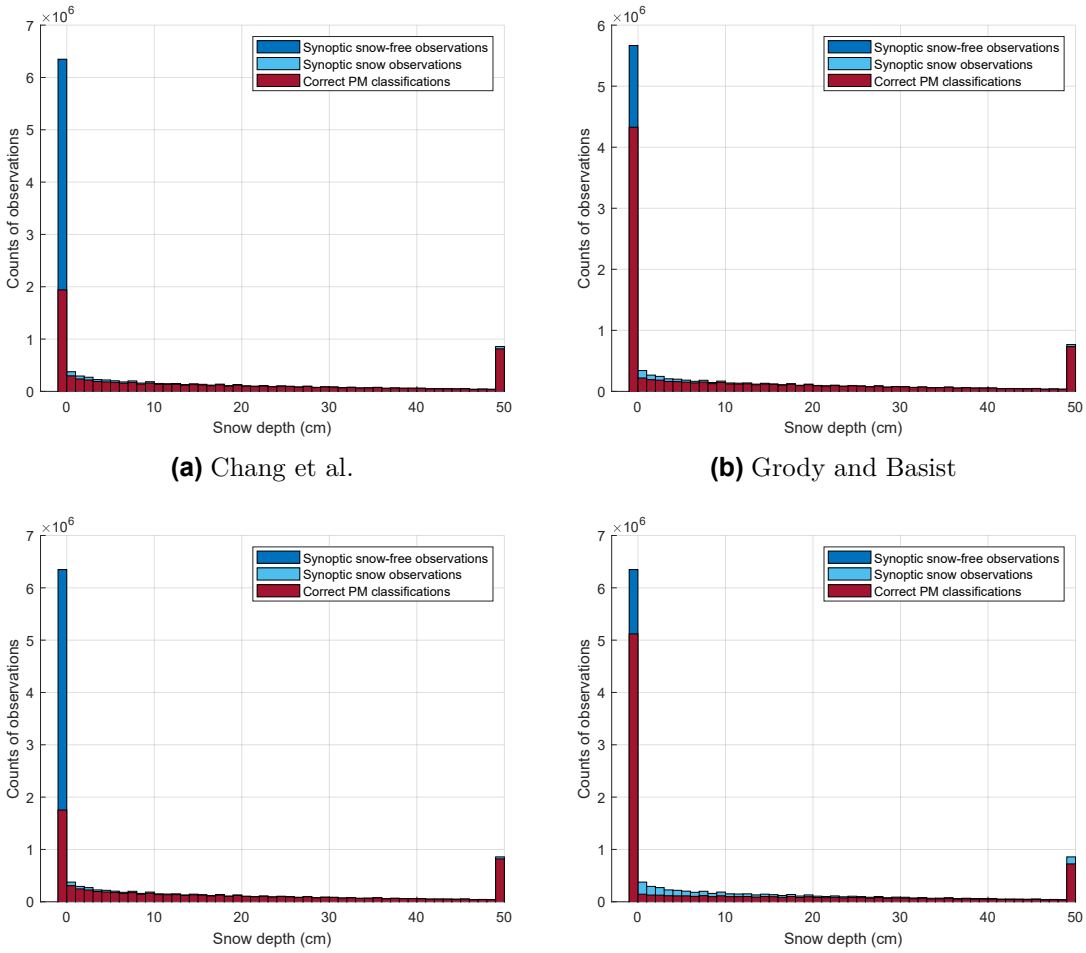

(a) Chang et al.

(b) Grody and Basist

(c) Foster et al.

(d) Armstrong and Brodzik

Figure A.9. Histograms of synoptic SD observations, and the share of correct snow/snow-free classifications for PM cumulative snow masks of SMMR, SSM/I and SSMIS data (continued).

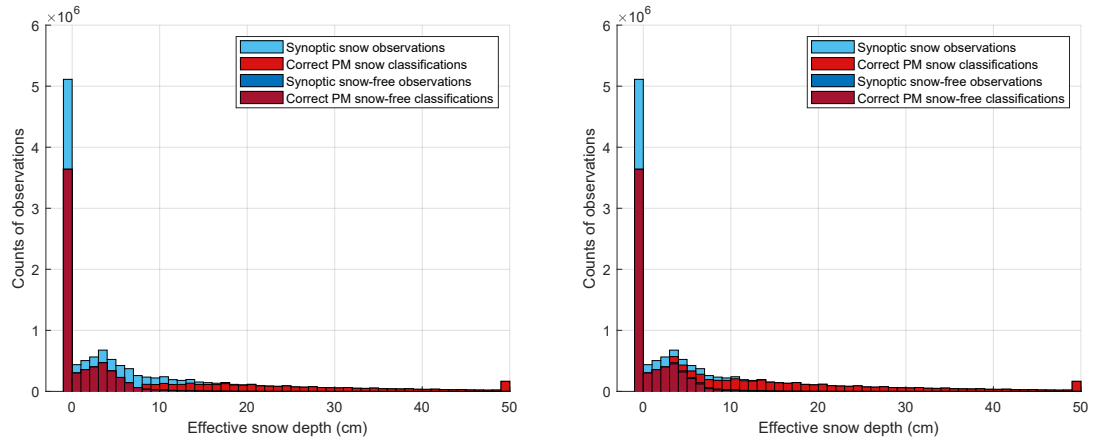

(a) GlobSnow **(b)** HSAF (H11)

Figure A.10. Histograms of synoptic observations versus corresponding effective SD estimated by PM dry snow detection algorithms for daily snow masks, and the share of correct snow/snow-free classifications for PM daily snow masks of SMMR, SSM/I and SSMIS data.

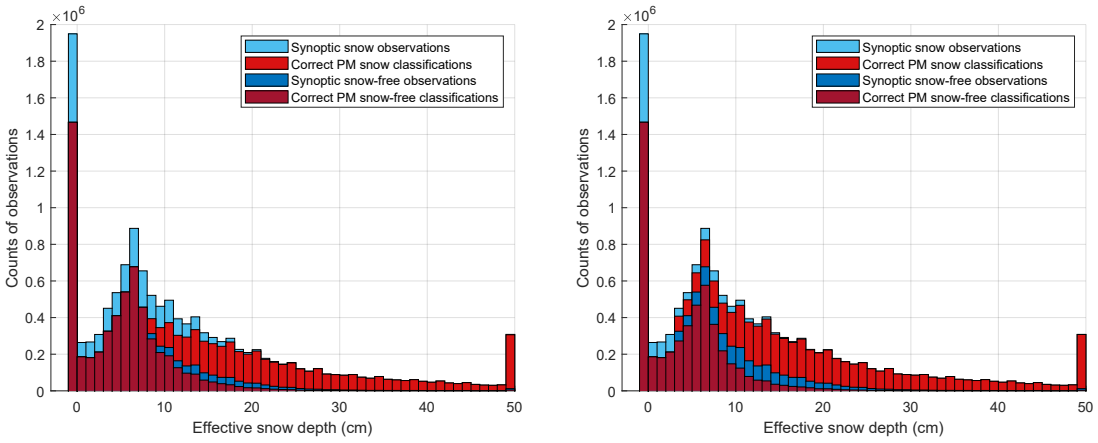

(a) GlobSnow **(b)** HSAF (H11)

Figure A.11. Histograms of synoptic observations versus corresponding effective SD estimated by PM dry snow detection algorithms for cumulative snow masks, and the share of correct snow/snow-free classifications for PM cumulative snow masks of SMMR, SSM/I and SSMIS data.

A.4 Monthly Difference Maps

Chang et al.

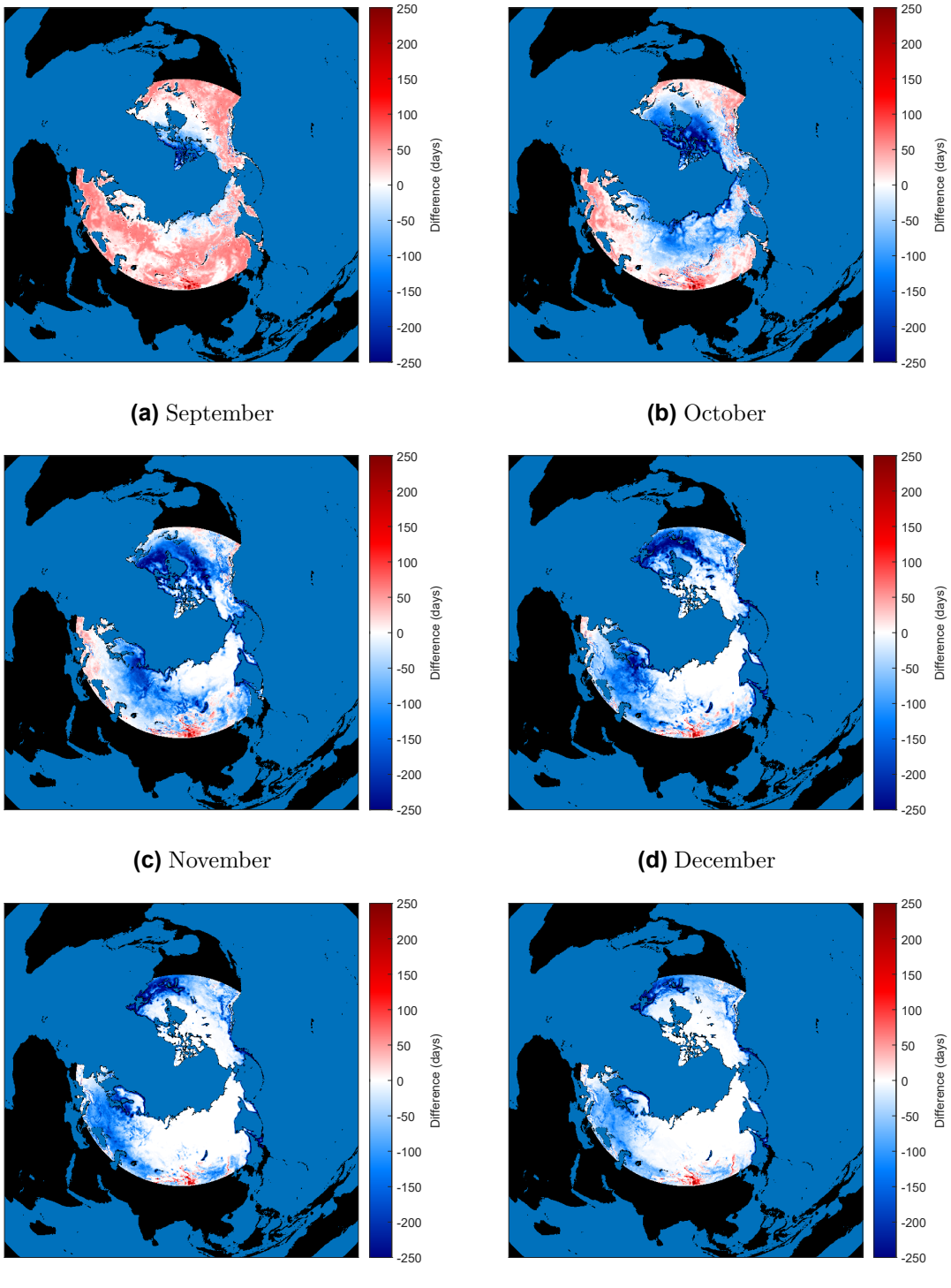

(a) September

(b) October

(c) November

(d) December

(e) January

(f) February

Figure A.12. Monthly difference maps for PM daily snow masks of Chang et al. covering the winters from 2007/2008 to 2016/2017.

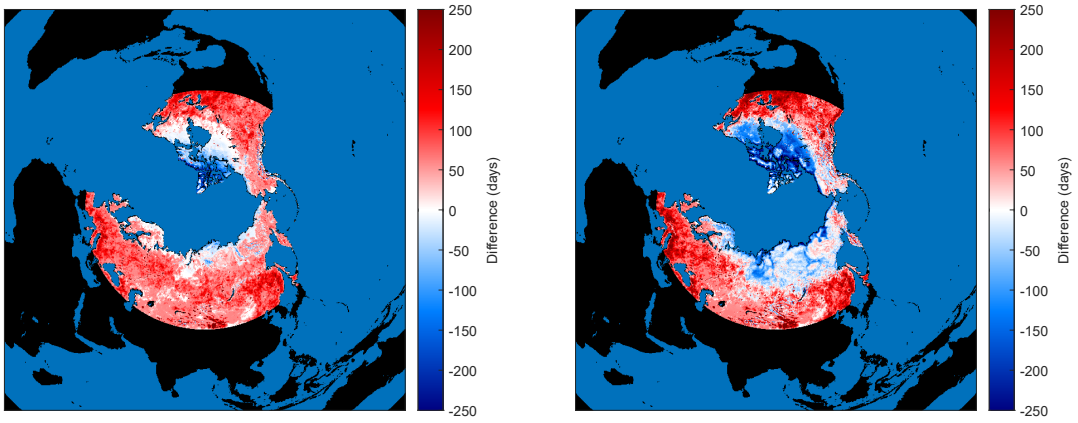

(a) September

(b) October

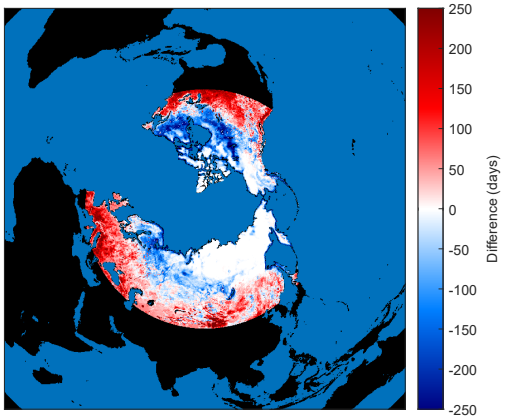

(c) November

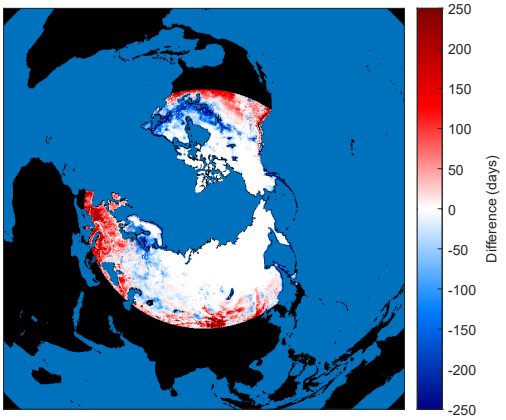

(d) December

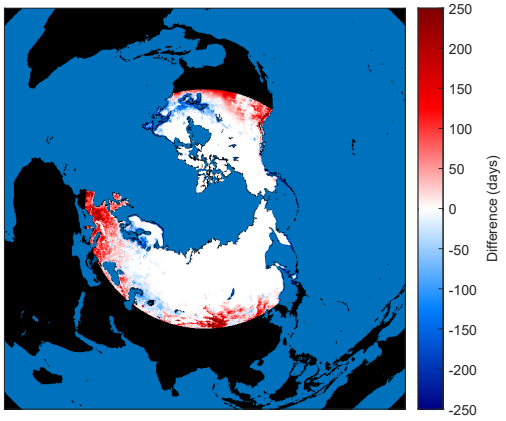

(e) January

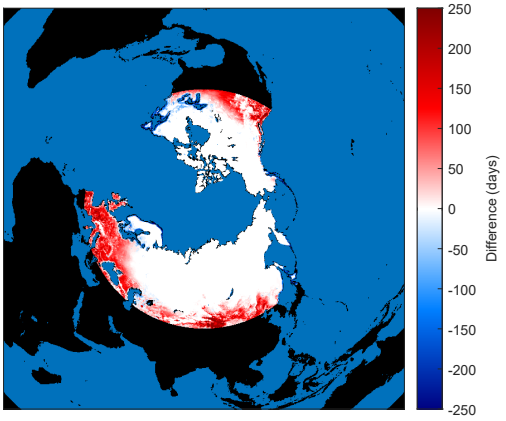

(f) February

Figure A.13. Monthly difference maps for PM cumulative snow masks of Chang et al. covering the winters from 2007/2008 to 2016/2017.

Grody and Basist

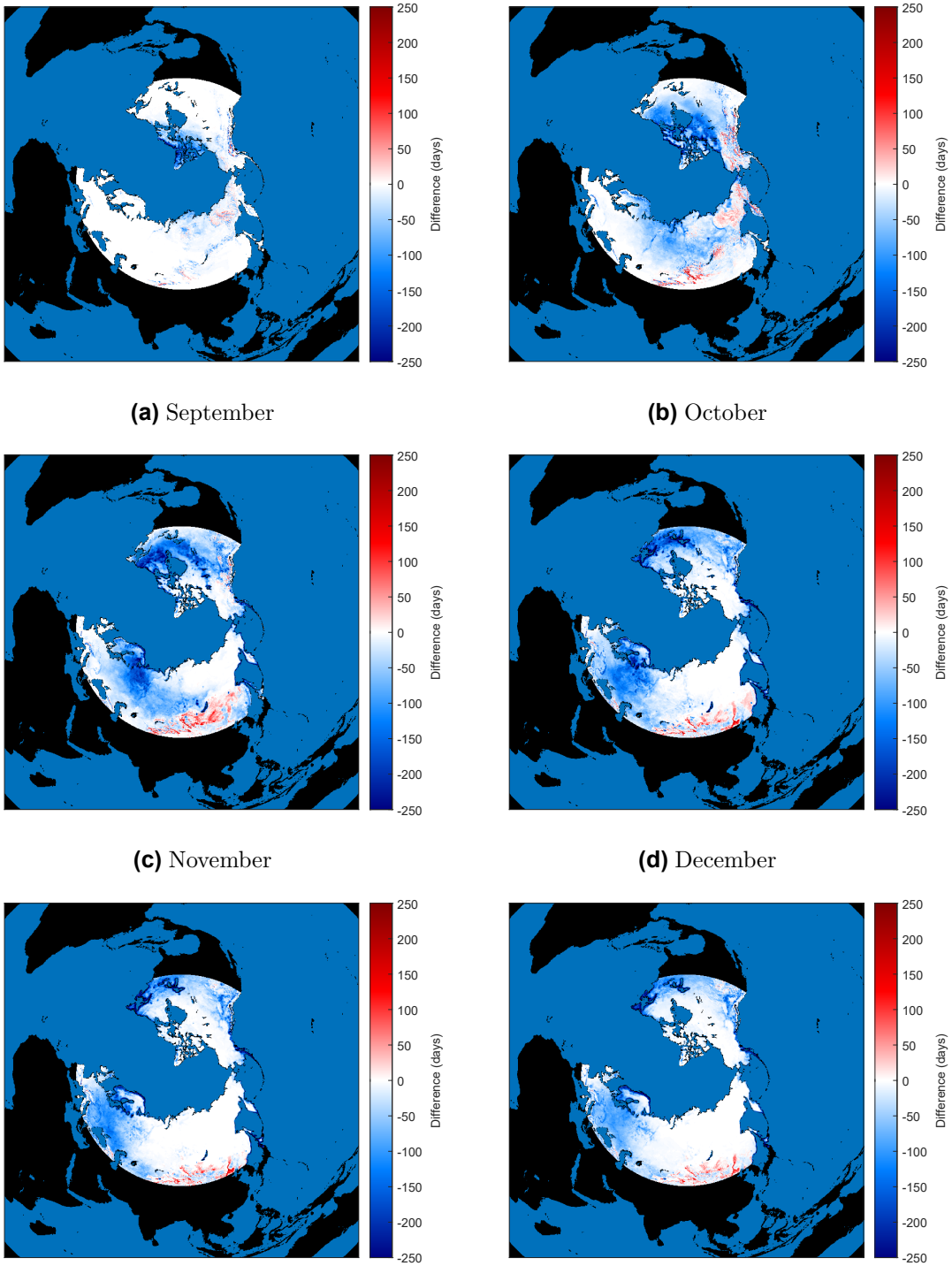

(a) September

(b) October

(c) November

(d) December

(e) January

(f) February

Figure A.14. Monthly difference maps for PM daily snow masks of Grody and Basist covering the winters from 2007/2008 to 2016/2017.

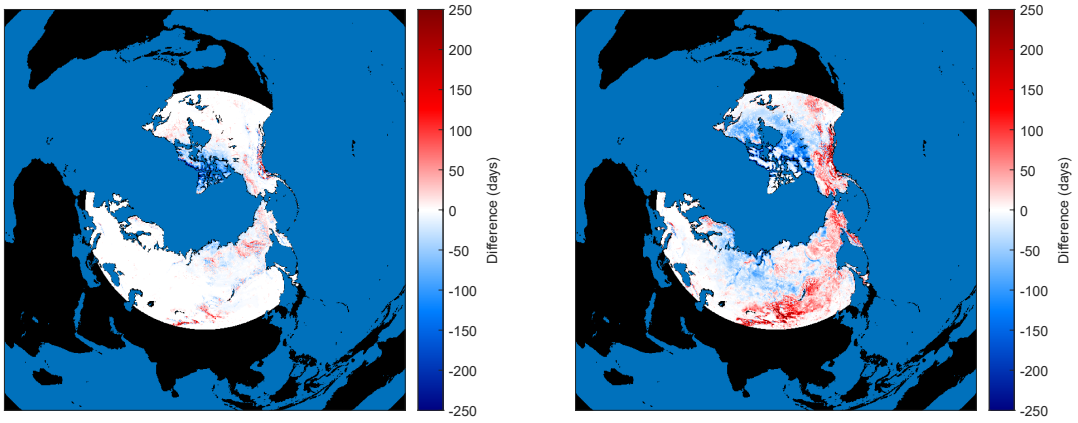

(a) September **(b)** October

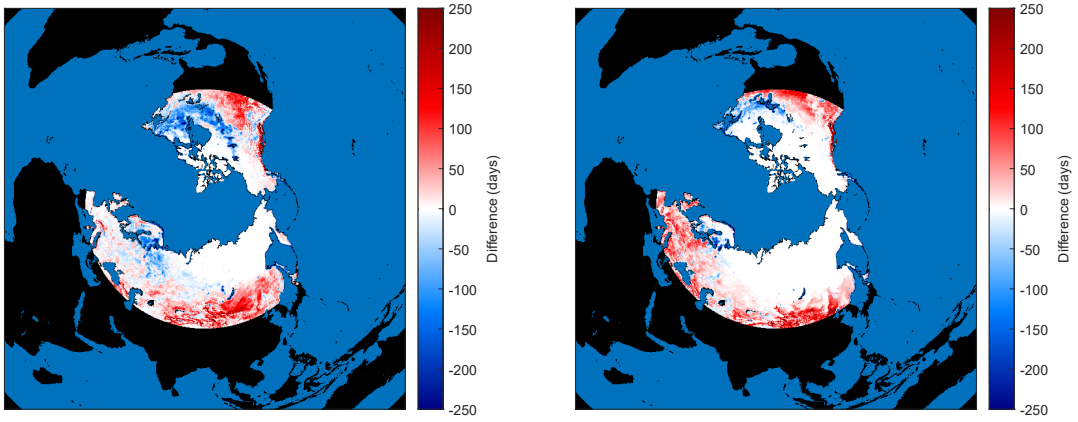

(c) November **(d)** December

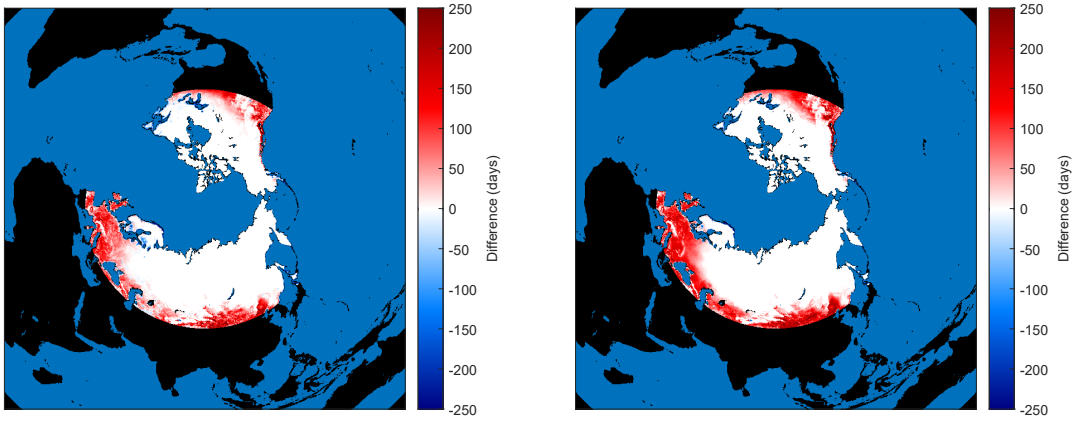

(e) January **(f)** February

Figure A.15. Monthly difference maps for PM cumulative snow masks of Grody and Basist covering the winters from 2007/2008 to 2016/2017.

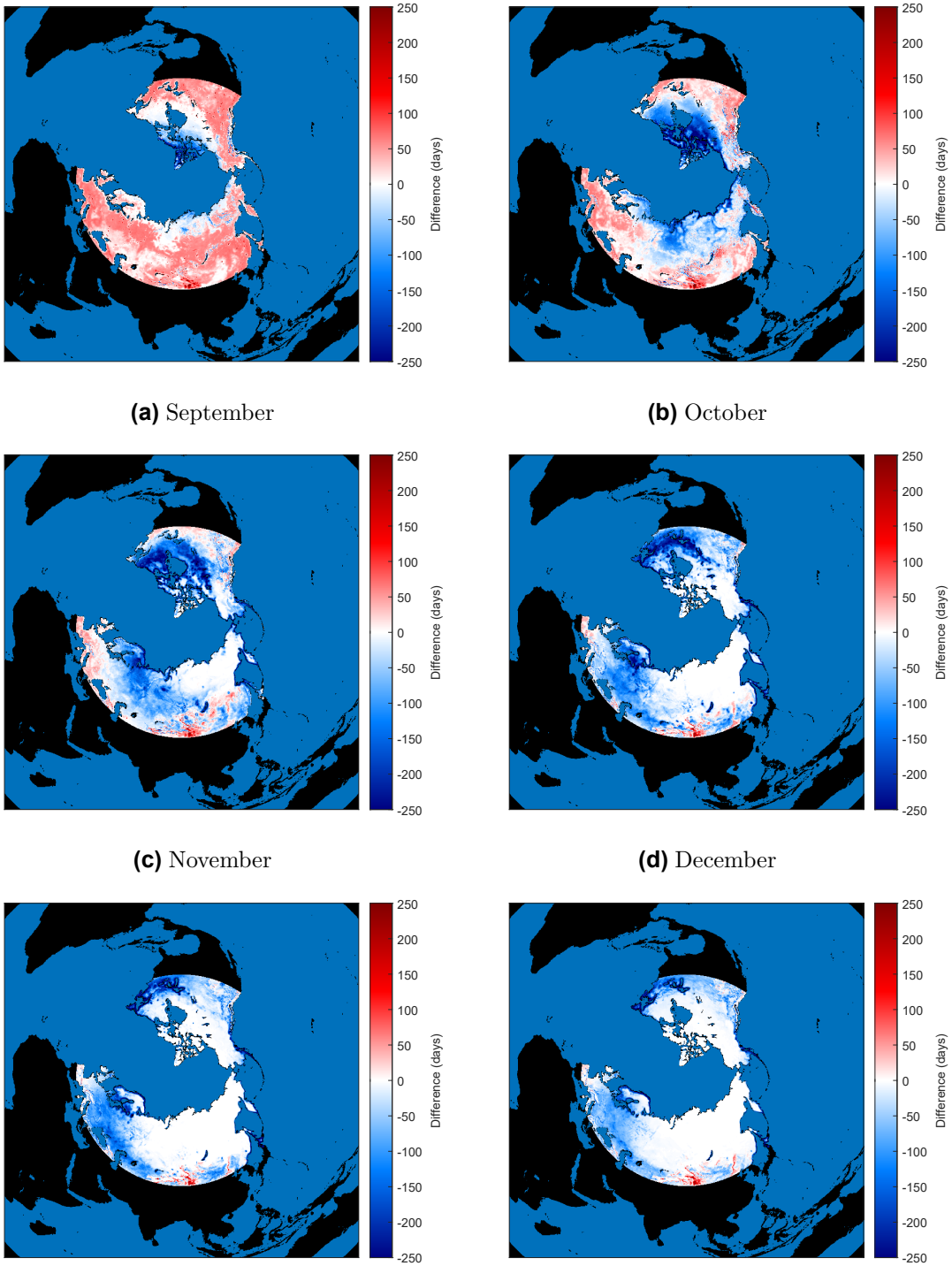

(a) September **(b)** October

(c) November **(d)** December

(e) January **(f)** February

Figure A.16. Monthly difference maps for PM daily snow masks of Foster et al. covering the winters from 2007/2008 to 2016/2017.

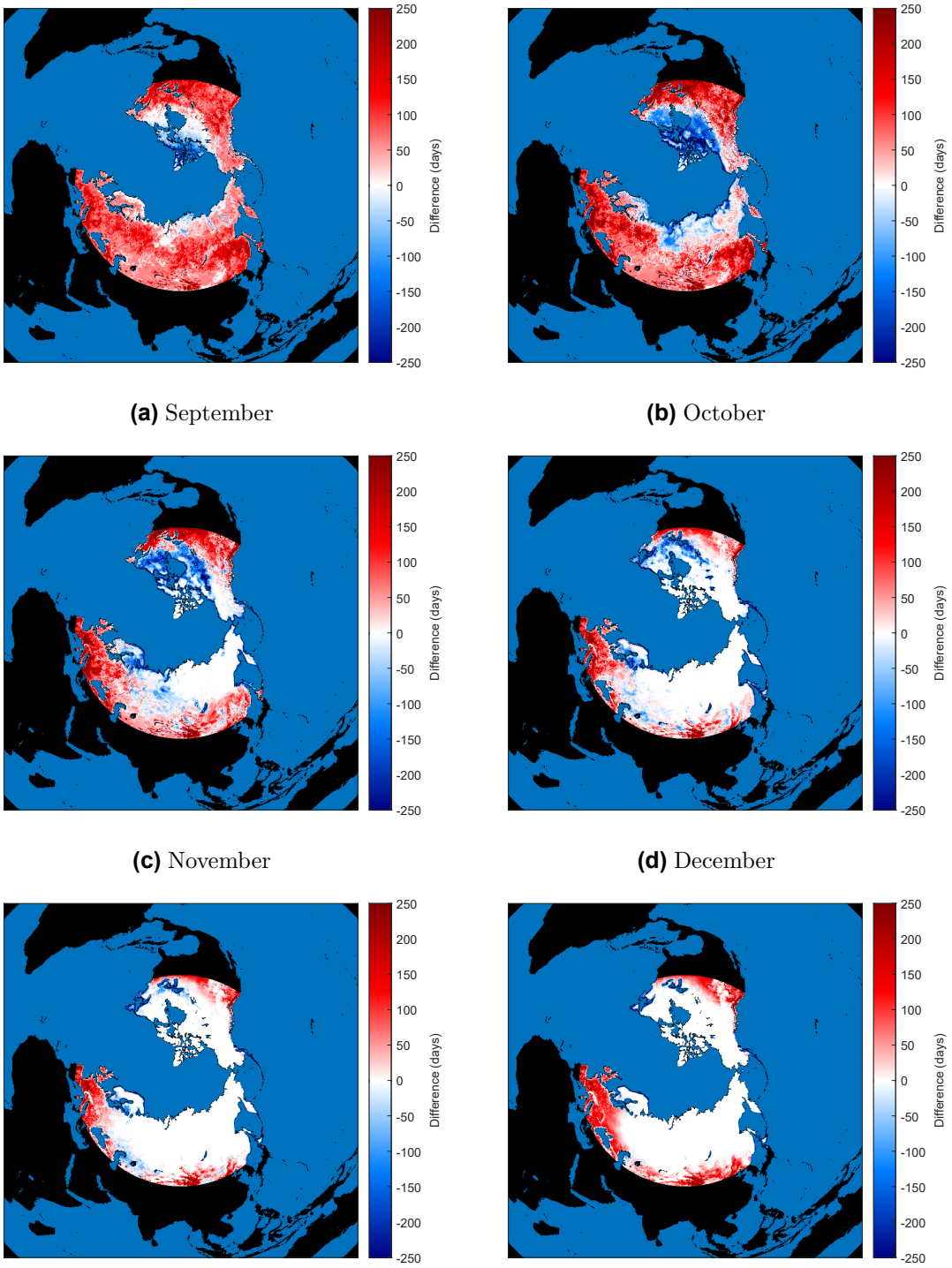

(a) September

(b) October

(c) November

(d) December

(e) January

(f) February

Figure A.17. Monthly difference maps for PM cumulative snow masks of Foster et al. covering the winters from 2007/2008 to 2016/2017.

Armstrong and Brodzik

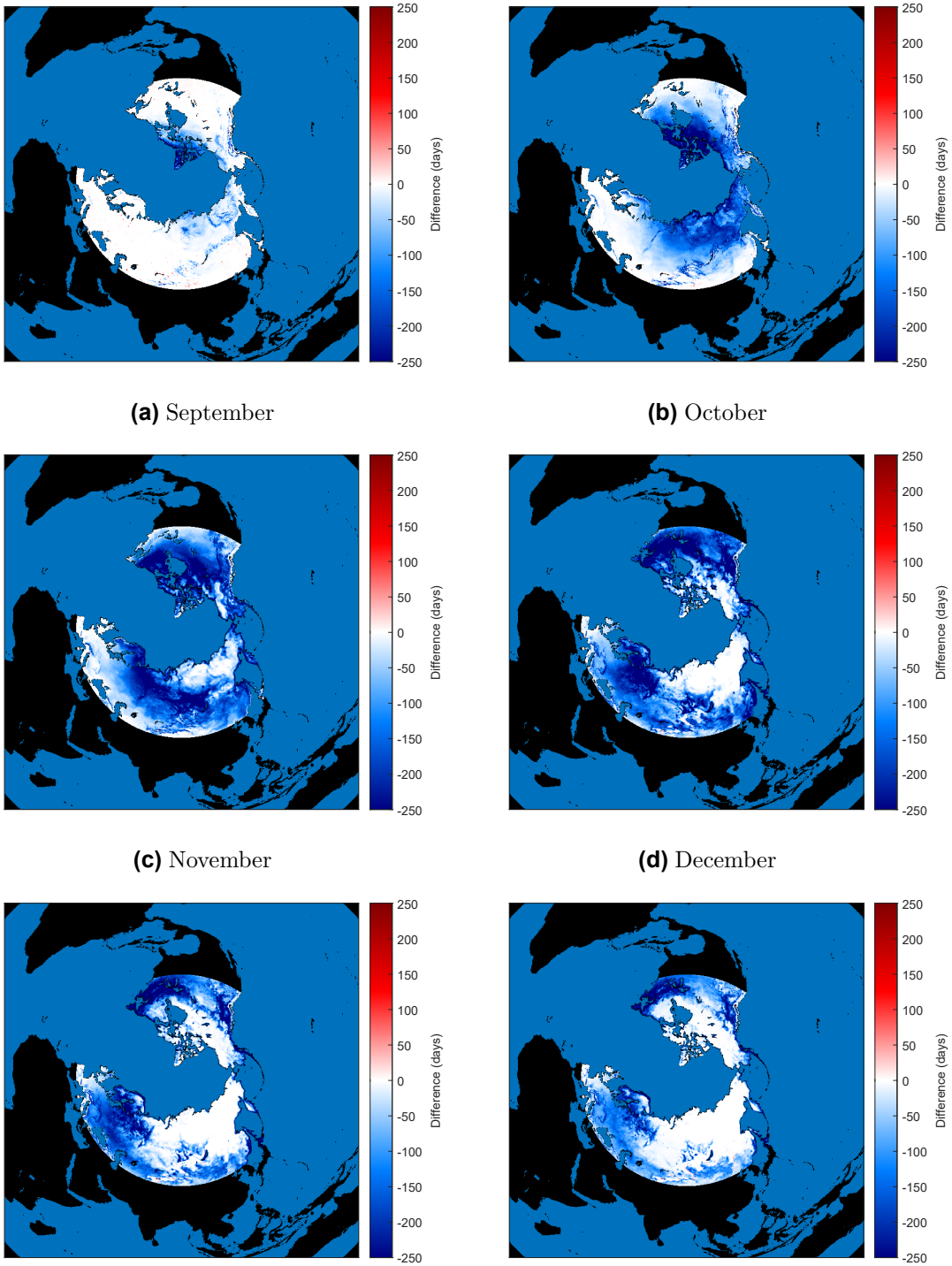

(a) September

(b) October

(c) November

(d) December

(e) January

(f) February

Figure A.18. Monthly difference maps for PM daily snow masks of Armstrong and Brodzik covering the winters from 2007/2008 to 2016/2017.

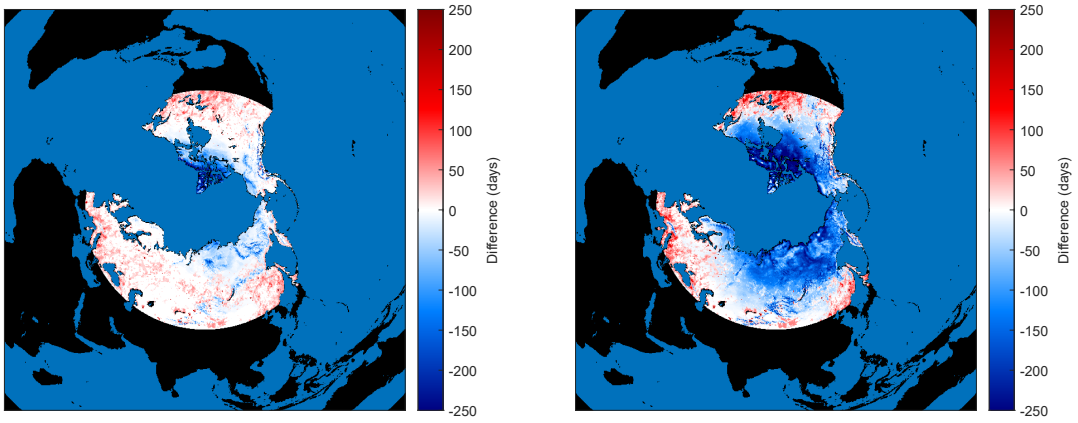

(a) September

(b) October

(c) November

(d) December

(e) January

(f) February

Figure A.19. Monthly difference maps for PM cumulative snow masks of Armstrong and Brodzik covering the winters from 2007/2008 to 2016/2017.

GlobSnow

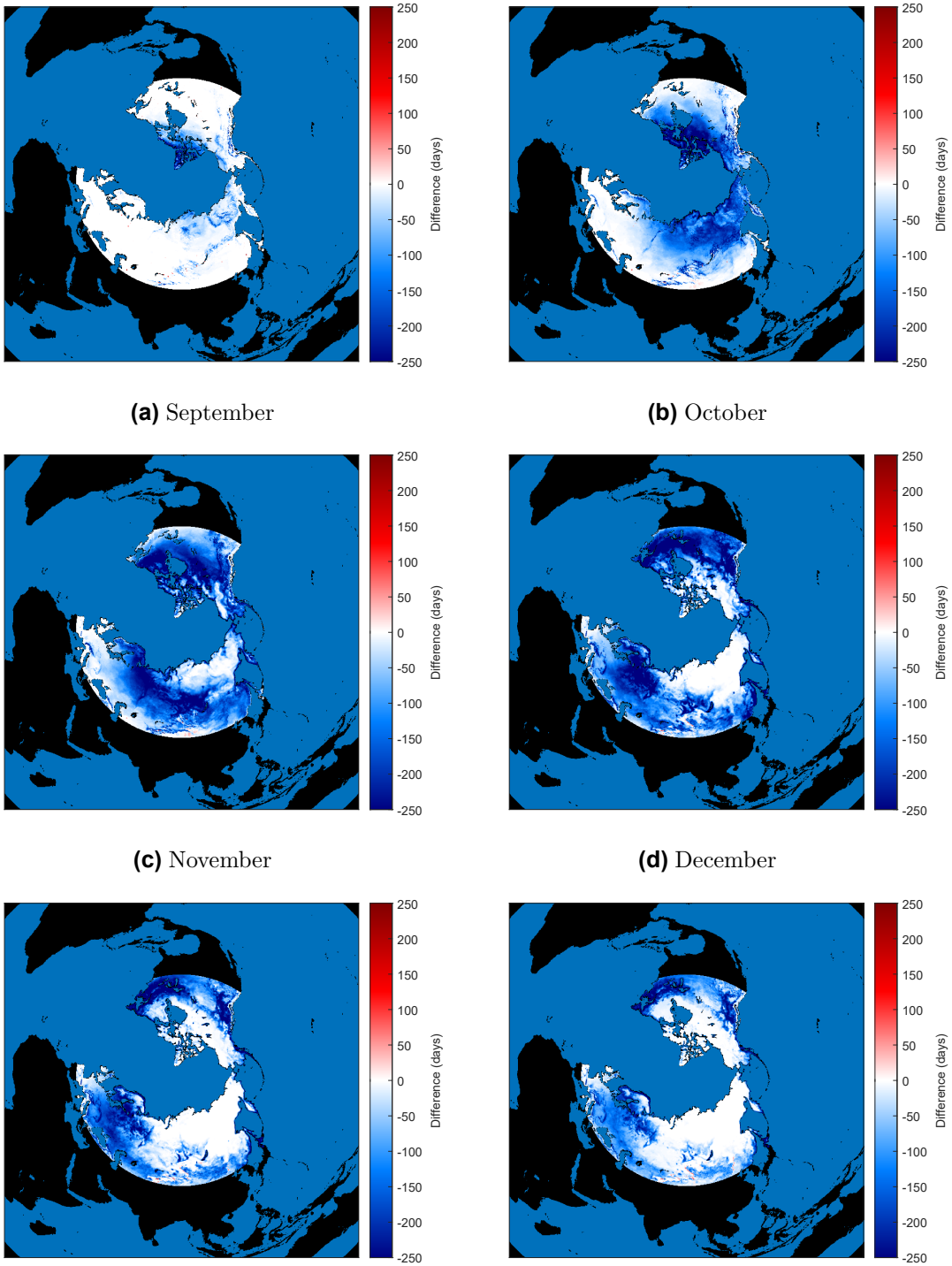

(a) September

(b) October

(c) November

(d) December

(e) January

(f) February

Figure A.20. Monthly difference maps for PM daily snow masks of GlobSnow covering the winters from 2007/2008 to 2016/2017.

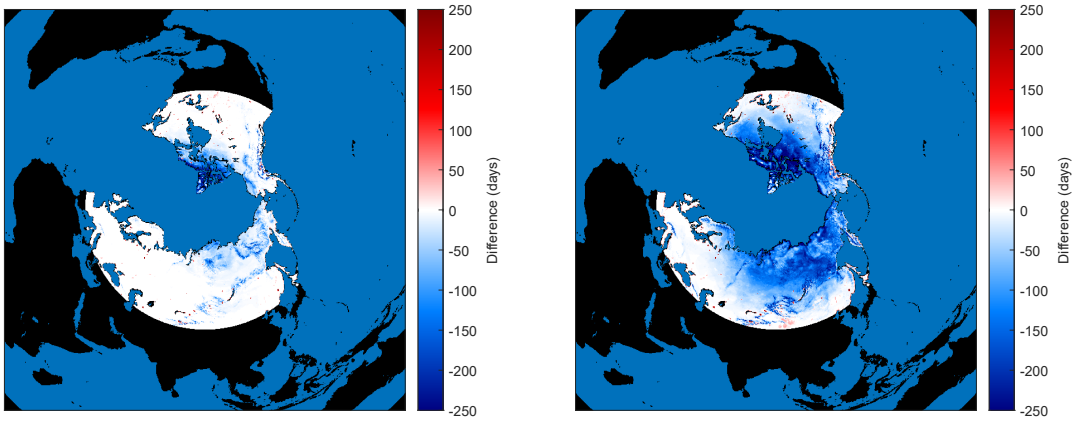

(a) September **(b)** October

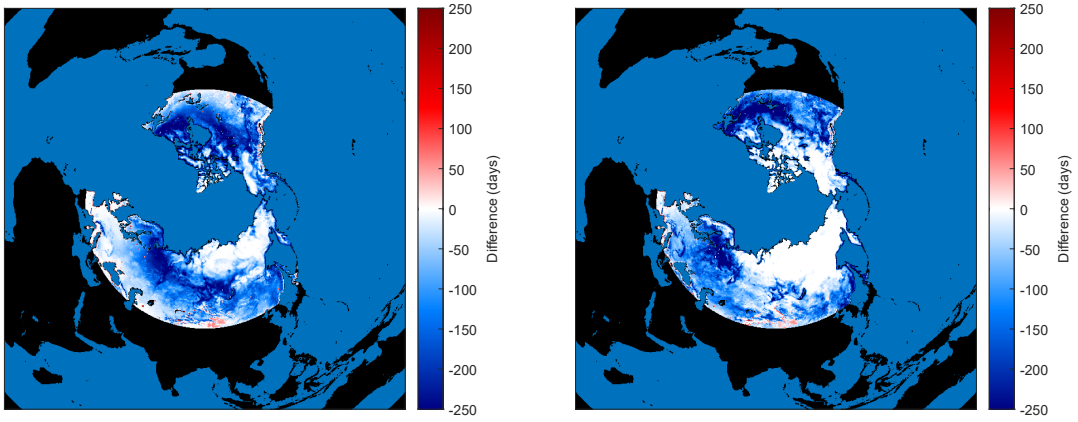

(c) November **(d)** December

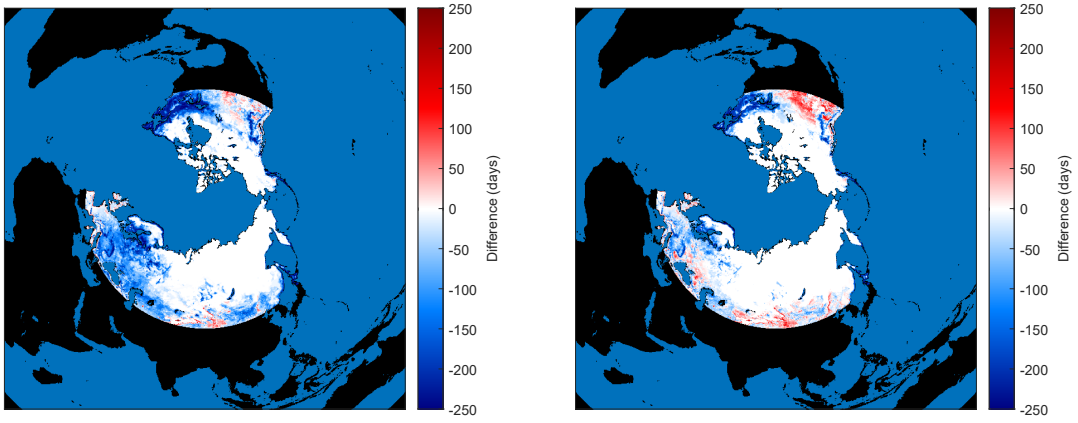

(e) January **(f)** February

Figure A.21. Monthly difference maps for PM cumulative snow masks of GlobSnow covering the winters from 2007/2008 to 2016/2017.

H SAF (H11)

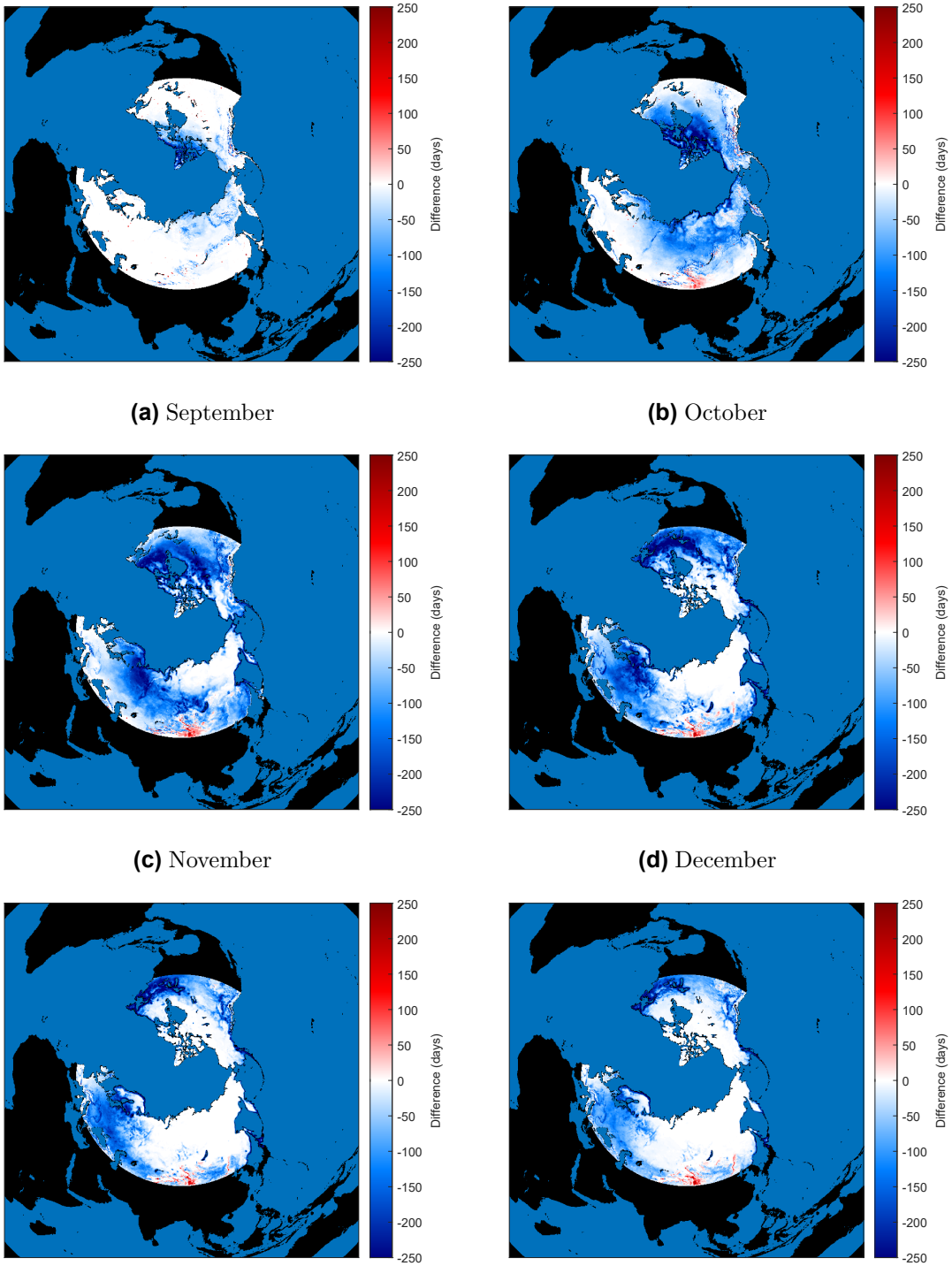

(a) September

(b) October

(c) November

(d) December

(e) January

(f) February

Figure A.22. Monthly difference maps for PM daily snow masks of H SAF (H11) covering the winters from 2007/2008 to 2016/2017.

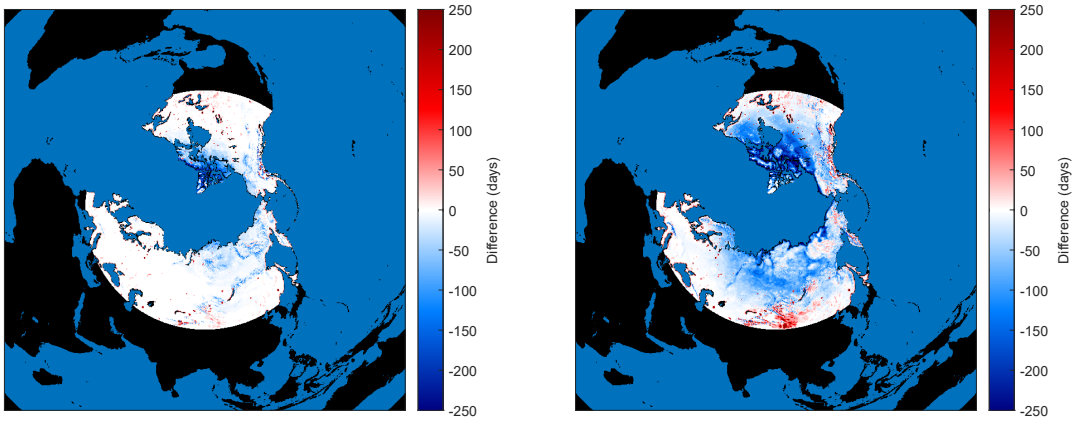

(a) September **(b)** October

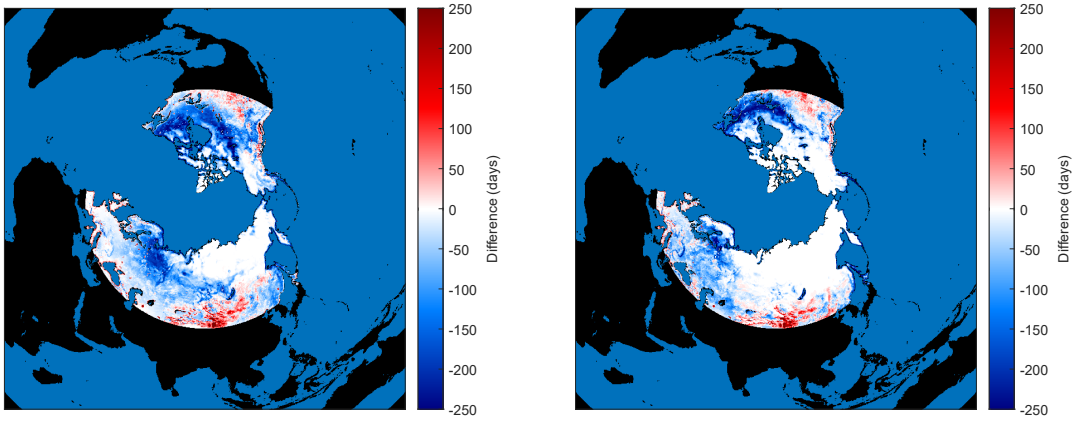

(c) November **(d)** December

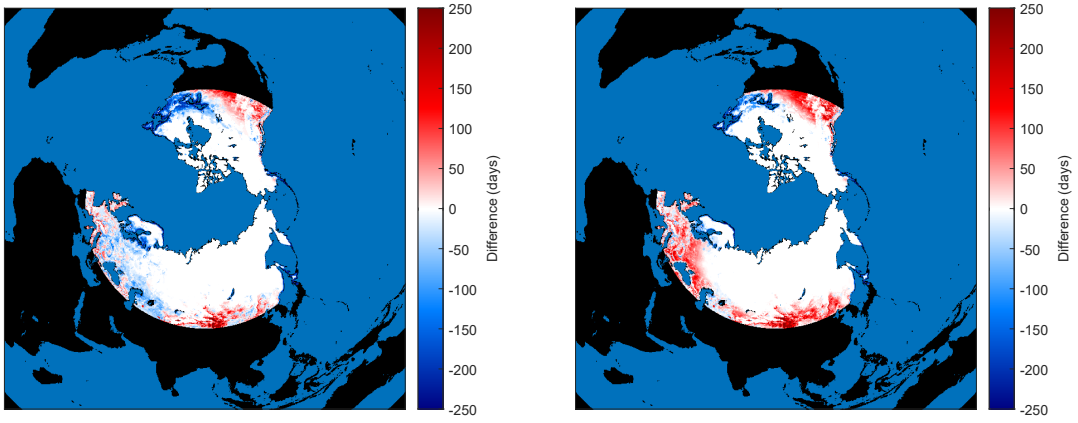

(e) January **(f)** February

Figure A.23. Monthly difference maps for PM cumulative snow masks of H SAF (H11) covering the winters from 2007/2008 to 2016/2017.